

Faculty of Physics and Astronomy

University of Heidelberg, Germany

Diploma Thesis

in Physics

submitted by

Carina Reble

born in Backnang, Germany

2007

Experimental and Theoretical Investigations of Dissipative Structures in Living Human Immune Cells

This Diploma thesis has been carried out by

Carina Reble

at the

German Cancer Research Center (DKFZ)

and the

Interdisciplinary Center for Scientific Computing (IWR)

at Heidelberg, Germany

under the supervision of

Prof. Dr. Jörg Langowski,

Priv.-Doz. Dr. Dirk Lebiedz and

Prof. Dr. Christoph Cremer

Experimental and theoretical investigations of dissipative structures in living human immune cells

Oscillations of NAD(P)H and calcium concentrations were recently reported to modulate the intensity of cytosolic NAD(P)H-waves and submembrane Ca^{2+} -waves in migrating human neutrophils. In order to reproduce these results, a high-speed microscopy setup based on an EMCCD camera and a widefield microscope was built and characterized by its noise figures and sensitivity. Fluorimetric measurements with freshly isolated neutrophils show oscillations of NAD(P)H and Ca^{2+} with periods of 10-20s, 20-30s and 50-70s. The results further suggest, that oscillations in cell shape can cause an oscillating fluorescence signal as well. The particular origin of the oscillating fluorescence could not be clearly identified. Acquisitions of spatiotemporal NAD(P)H or Ca^{2+} -waves failed, likely for sensitivity reasons. In order to investigate the propagation mechanism of the submembrane Ca^{2+} -wave, a mathematical model was constructed, which is able to reproduce the characteristic wave properties. The model is based on a spatial coupling of local variations in membrane potential produced by a localized transmembrane current, and voltage dependent gating of T-type Ca^{2+} -channels.

Experimentelle und theoretische Untersuchungen von dissipativen Strukturen in lebenden menschlichen Immunzellen

Oszillationen von NAD(P)H- und Kalziumkonzentrationen in neutrophilen Granulozyten sind in der Literatur beschrieben. Diese wurden bei entsprechender raumzeitlicher Auflösung als zytosolische NAD(P)H- bzw. submembranäre Kalziumwellen identifiziert. Um diese Ergebnisse zu reproduzieren, wurde ein Hochgeschwindigkeits-Fluoreszenzmikroskop aufgebaut, welches auf einem Weitfeldmikroskop und einer EMCCD-Kamera basiert. Dieser Aufbau wurde bezüglich seiner Rauscheigenschaften und der Sensitivität charakterisiert. Bei fluorimetrischen Messungen an lebenden Neutrophilen wurden NAD(P)H- und Kalziumoszillationen mit Perioden von 10-20s, 20-30s und 50-70s festgestellt. Die jeweilige Ursache der oszillierenden Fluoreszenzsignale konnte jedoch nicht eindeutig bestimmt werden. Die Ergebnisse weisen darauf hin, dass sowohl oszillierende Konzentrationen als auch Oszillationen des Zellkörpers ein oszillierendes Fluoreszenzsignal verursachen können. Die Detektion von raumzeitlichen Wellen allerdings scheiterte, was unter anderem auf ein ungenügendes Signal/Rausch-Verhältnis des Aufbaus zurückgeführt werden kann. Um den Propagationsmechanismus der submembranen Kalziumwelle zu untersuchen, wurde ein mathematisches Modell entwickelt, welches charakteristische Eigenschaften der Welle reproduziert. Dieses eindimensionale Modell basiert auf einer lokalen Kopplung von spannungsabhängigem Öffnungsverhalten der T-Typ Kalziumkanäle und einer lokalen, durch Kalziumeinstrom induzierten Membranpotenzialänderung.

Contents

| | | |
|----------|--|----------|
| 1 | Introduction | 1 |
| 2 | Basics | 5 |
| 2.1 | Microscopy basics | 5 |
| 2.1.1 | Image formation and resolution in widefield microscopy | 5 |
| 2.1.2 | Fluorescence microscopy | 7 |
| 2.2 | High-speed cameras | 8 |
| 2.2.1 | ICCD | 8 |
| 2.2.2 | EBCCD | 9 |
| 2.2.3 | EMCCD | 10 |
| 2.2.4 | Noise contributions of CCD based cameras | 13 |
| 2.3 | Setup established by Petty et al. | 16 |
| 2.3.1 | How short must exposure times be for wave detection? | 17 |
| 2.4 | Neutrophil Granulocytes | 19 |
| 2.5 | Cell polarization, migration and shape oscillations | 20 |
| 2.6 | NAD(P)H-metabolism and autofluorescence | 22 |
| 2.7 | NAD(P)H-oscillations and waves | 23 |
| 2.8 | Ca ²⁺ -signaling | 24 |
| 2.8.1 | The low voltage gated T-type Ca ²⁺ -channel | 25 |
| 2.9 | Ca ²⁺ -oscillations and waves | 26 |
| 2.9.1 | Temporal Ca ²⁺ -oscillations | 26 |
| 2.9.2 | Types and mechanisms of spatiotemporal Ca ²⁺ -waves | 26 |

| | | |
|----------|---|-----------|
| 2.10 | Transmembrane ion transport and potential | 27 |
| 2.11 | Models of the uniform membrane potential | 28 |
| 2.11.1 | The membrane as electrical circuit | 28 |
| 2.12 | Nonuniform membrane potential variation produced by localized ion current | 29 |
| 3 | Instrumental setup and characterization | 33 |
| 3.1 | Setup | 33 |
| 3.1.1 | Microscope and illumination system | 33 |
| 3.1.2 | Image splitter | 34 |
| 3.1.3 | Camera control and cooling | 35 |
| 3.1.4 | Computer components | 36 |
| 3.1.5 | Cell incubation during measurements | 36 |
| 3.1.6 | Data acquisition and analysis | 36 |
| 3.2 | Camera characterization | 37 |
| 3.2.1 | Spatial resolution | 37 |
| 3.2.2 | Temporal resolution | 38 |
| 3.2.3 | Real gain factor | 39 |
| 3.2.4 | Blemishes | 40 |
| 3.2.5 | Readout noise | 40 |
| 3.2.6 | Spurious charge | 43 |
| 3.2.7 | Dark current | 43 |
| 3.2.8 | Detection efficiency of the Setup | 45 |
| 3.3 | Conclusion | 49 |
| 4 | Live cell measurements | 51 |
| 4.1 | Materials and methods | 51 |
| 4.1.1 | Cell preparation and handling | 51 |
| 4.1.2 | NAD(P)H measurement | 53 |
| 4.1.3 | Calcium measurements | 54 |
| 4.1.4 | Shape measurements | 55 |

| | | |
|----------|--|------------|
| 4.1.5 | Data acquisition | 57 |
| 4.1.6 | Data analysis | 58 |
| 4.2 | Results | 59 |
| 4.2.1 | Effect of illumination power on cell behavior | 59 |
| 4.2.2 | Cell morphology and migration behavior | 62 |
| 4.2.3 | Shape oscillations | 63 |
| 4.2.4 | NAD(P)H-oscillations | 64 |
| 4.2.5 | Ca ²⁺ -oscillations | 66 |
| 4.2.6 | Problems with spatiotemporal acquisitions | 70 |
| 4.2.7 | Effect of cell stimulation | 71 |
| 4.2.8 | Experiments with HT1080 cells | 72 |
| 4.3 | Discussion | 72 |
| 4.3.1 | Shape oscillations and/or concentration oscillations? | 72 |
| 4.3.2 | Technical problems and limitations | 74 |
| 4.3.3 | Biological problems | 75 |
| 4.4 | Conclusion | 78 |
| 4.4.1 | An ideal setup for detection of biochemical oscillations | 78 |
| 4.4.2 | An ideal setup for detection of waves | 79 |
| 5 | Modeling of a submembrane Ca²⁺-wave | 83 |
| 6 | Summary | 109 |
| | Bibliography | 113 |
| | Acknowledgements | 117 |

Chapter 1

Introduction

Living cells are open systems far from equilibrium. The continuous exchange of matter and energy with the environment enables the formation of dissipative structures such as chemical concentration oscillations and self-organized patterns.

A variety of temporal oscillations in living human neutrophils have been observed so far, including oscillations of NAD(P)H, Ca^{2+} , plasma membrane potential and cell shape [1]. Recently, a high-speed microscopy setup established by Petty et al. (*Kellogg Eye Center, Michigan, USA*) allowed to capture movies of cytosolic NAD(P)H-waves and submembrane Ca^{2+} -waves. The intensity of the spatiotemporal NAD(P)H-waves is modulated by temporal oscillations with a period of 20s while the Ca^{2+} -wave coincides with repetitive baseline Ca^{2+} -spikes, also with a period of 20s, see Fig. 1.1.

It was shown that such phenomena are not just a physical curiosity, but are correlated to fundamental cellular functions such as migration and orientation. As neutrophils become morphologically polarized, as it is required for migration, a calcium wave is ignited at the leading edge and travels unidirectionally around the cell perimeter underneath the plasma membrane. When the cell senses a chemotactic signal such as a bacterial peptide, a new calcium wave is produced at the location of sensing, long before the cell actually changes its direction. Thus, the wave ignition site is linked to chemosensory perception [2, 3]. Similarly, the single longitudinal NAD(P)H wave in a polarized neutrophil responds to receptor stimulation by splitting into two waves, which travel in opposite directions [4]. Furthermore, the NAD(P)H-wave promotes the formation of superoxide anions, which is one of the primary functions of neutrophils [5].

It has been speculated that the presence and absence of a variety of superimposed chemical waves enables the cell to perform a sort of analog chemical computation [3]. Similarly as the well known depolarization waves in neurons, the much slower chemical waves could provide physiological information. The biological effect of a chemical wave might be to act

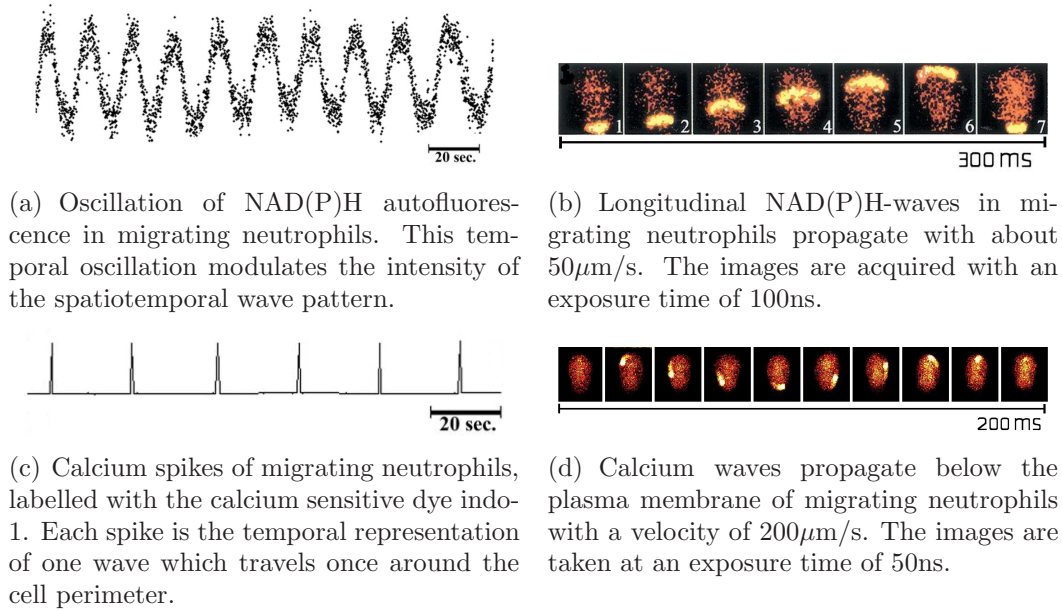


Figure 1.1

on nearby proteins. Proteins change their conformations on timescales of μs to ms , which is comparable to the time in which a wave passes a stationary point.

The reason why such waves have not been reported earlier is that conventional, slow speed imaging approaches are not capable of capturing fast travelling wave phenomena. Wave transit times in small cells ($\approx 10\mu\text{m}$) are shorter than typical exposure times of slow detectors, causing blurring of the signal. A higher temporal resolution in terms of high frame rates and/or short exposure times is required to investigate the timescales relevant for the event under study. Capturing a movie of the submembrane calcium wave, which propagates for a total transit time of 200ms, requires a frame rate > 30 frames per second. Since the wave propagates with a velocity of $200\mu\text{m/s}$, an exposure time of 1ms is required to avoid signal blurring due to wave motion, if the resolution limit is 200nm. However, Petty et al. reported that exposure times shorter than $200\mu\text{s}$ are required to recognize a spatiotemporal wave pattern, and that the contrast of the wave image improves even on a submicrosecond timescale, see Fig. 1.2. This observation can definitely not be explained by the diffusion of calcium-dye complexes. Clearly, further research is required to investigate these surprising findings.

Since shortening exposure times reduces the photon yield, a high sensitivity of the setup is crucial for high-speed acquisitions. The most important component of a high speed microscopy setup is therefore a detector that combines high sensitivity with high read out rates, such as an ICCD or an EMCCD camera. The low photon yield further limitates the spatial resolution of high-speed microscopy. Sufficient spatial resolution for this application

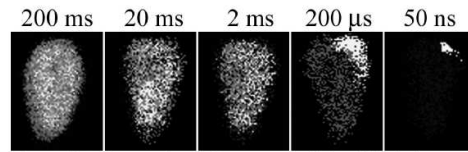


Figure 1.2: Calcium wave acquisitions at different exposure times. A Ca^{2+} -wave is recognizable at exposure times below $200\mu\text{s}$ [2], although the wave is stationary at exposure times of 1ms.

is provided by conventional widefield microscopy which further allows to observe large sample volumes simultaneously.

Unfortunately, apart from the setup established by Petty et al. in which an ICCD camera is fiber-optically coupled to the bottom port of a widefield microscope, no other technique was so far able to find results of similar image quality, phenomenological detail and curiosity. In addition to the technical challenge, this might result from the fact that these phenomena require a physiological in vitro cell behavior, which can be easily disturbed by improper cell handling.

The aim of the experimental part of this diploma thesis project was to reproduce the results of Petty et al. under comparable technical and biological conditions. For that purpose, a high speed microscopy setup, based on a widefield microscope and an EMCCD camera was built and characterized. Subsequently, experiments with freshly isolated living human neutrophils have been carried out by using different cell isolation methods and microscopy setups.

In addition to experimental approaches, mathematical modeling and simulation can provide insides to the mechanisms leading to the formation of dissipative structures. The aim of the theoretical part of this thesis was to construct a mathematical model, which is able to reproduce the characteristic propagation behavior of the Ca^{2+} -wave. This was done in collaboration with Mario Mommer (IWR/BIOMS, Heidelberg).

Chapter 2

Basics

2.1 Microscopy basics

This section will review the basic principles of widefield microscopy that are helpful to understand the characteristics of the imaging system, that was used to detect spatiotemporal fluorescence signals in living cells.

2.1.1 Image formation and resolution in widefield microscopy

Image formation in widefield microscopy can be described in terms of wave optics, where the light from one point source is described as a spherical wave that is centered in the object point. According to Huygens principle a wavefront is made up of a series of point sources of light, each emitting a spherical wave also called Huygen wavelets that constructively interfere at the image point. The three dimensional diffraction pattern of a point source is called Point Spread Function (PSF). The three dimensional diffraction pattern of an object can now be treated as intensity distribution of the interference pattern that arises from summation of all wavelets for each point in the image plane. The mathematical tool to describe wavelets are Bessel functions. Fourier transformation of the complex amplitude distribution in the aperture plane gives the amplitude distribution in the image plane. The square of this result is the intensity distribution.

For a well corrected objective lens, the PSF near the focal point is symmetrically periodic along the axis of the light path as well as radially symmetric. A cross-section of the PSF perpendicular to the focal plane is shown in Fig. 2.1(b). In the focal plane, the 2D section is called the Airy disk, see Fig. 2.1(a). Since the waves forming adjacent Airy disks superimpose incoherently for self-luminous bodies, one can determine the minimum resolvable separation distance of overlapping Airy disks in the image plane. If the first minimum

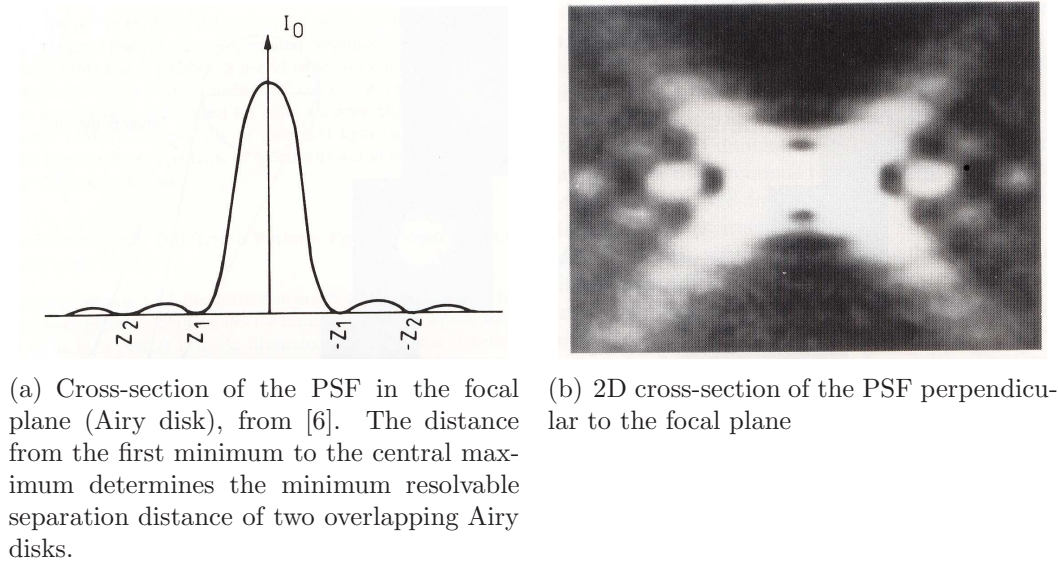


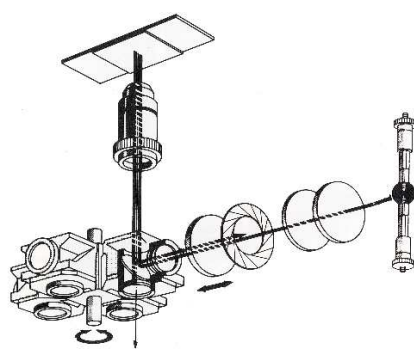
Figure 2.1

of one disk is aligned with the central maximum of a second disk (which is not displayed in Fig. 2.1(a)), the distance is also known as the minimum resolvable separation distance according to Rayleigh criterion. Following this definition, the lateral resolution limit is $d_{x,y} = 0.61\lambda/\text{NA}$ where $\text{NA} = n \sin(\theta/2)$ (with n being the refractive index of immersion media and θ being the angle cone of light captured by the objective). The axial resolution is $d_z = 2\lambda/\text{NA}^2$ in case of epi-illumination where the objective serves as condenser and thus has the same NA. Although this criterion for spatial resolution is based on a set of assumptions and is not valid for any modern light microscopy technique, it is still a good approximation for traditional widefield microscopy. Improvements in resolution can be obtained with z-scanning and computational deconvolution or structured illumination methods. Dramatic improvements can be achieved e.g. with stimulation emission depletion (STED) microscopy or photo activated localization microscopy (PALM) which allow spatial resolution in the 10nm range.

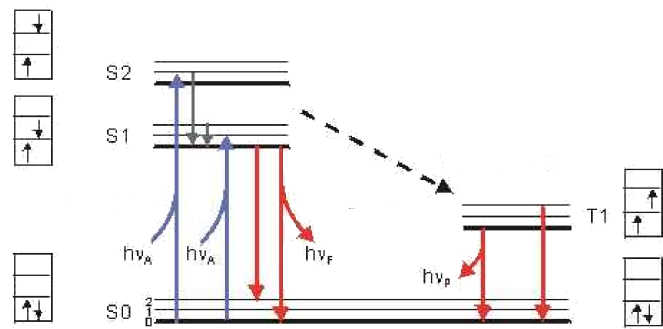
The theoretical spatial resolution of an imaging system consisting of a microscope and an array detector is further limited by the number and size its pixels. The image size of the minimum resolvable distance compared to the size of the pixels determines the so called sampling. According to the well known Nyquist theorem two pixels per distance to be resolved are sufficient for optimal sampling. However, the Nyquist Theorem has been derived for 2D signals and does not apply correctly to 3D data of an image. In microscopy, 3 pixels per minimum distance to be resolved are recommended for optimal sampling.

In *widefield microscopy* the entire field of view is illuminated and light from the entire

sample is detected simultaneously with an array detector. This implicates that out of focus signal is not excluded from detection, which will be important when artifacts have to be excluded, as in the case of cell movements vertical to the focal plane. In *bright-field* (transmission) mode which was used for cell localization and characterization in this project, image contrast arises from absorption of object parts that possess high extinction coefficients or by refraction at object boundaries that are slightly out of focus (Becke lines). The contrast can be enhanced by closing the condenser iris, resulting in loss of resolution. Fluorescence imaging was done in *epi-illumination* or reflection contrast mode, where the image is formed by reflected or backscattered light of the object that is illuminated through the objective. A dichromatic mirror placed between lamp and objective reflects the beam into the objective which also serves as condenser, see Fig. 2.2(a). Only the backscattered light is transmitted towards the detector, which in case of fluorescence microscopy has a higher wavelength due to the Stokes shift.



(a) Epi-illumination light path [6]: Light source (right) and sample (top) are perpendicular to each other. Excitation and emission light is separated by a dichromatic mirror.



(b) Principle of fluorescence explained by a Jablonski diagram: Transitions between an excited singlet state (S1) and a ground state are called fluorescence while transitions from the triplet state (T1) are called phosphorescence.

Figure 2.2

2.1.2 Fluorescence microscopy

Photon emission that results from a transition between an excited electronic state and a lower energy state is called luminescence. Fast transitions with lifetimes in the nanosecond range are called fluorescence while transitions with lifetimes ranging from milliseconds to seconds are called phosphorescence. Such transitions are commonly represented by vertical lines in Jablonski diagrams, see Fig. 2.2(b) due to the Frank Condon principle. The lifetime of an excited state is inversely proportional to the probability of a transition.

Transitions of electrons from excited singlet states (S_1 in Fig. 2.2(b)) to the ground state containing an electron with opposite spin are allowed, leading to a comparably high transition probability. If the excited state is a triplet state (T_1 in Fig. 2.2(b)) with the same spin orientation as the ground state, transitions are called forbidden terms of classical physics, but occur with a non zero probability according to quantum mechanics.

Fluorescence emission provides a strong signal compared to chemiluminescence that only emits one photon per molecule. This is prerequisite for high spatial and temporal resolution which is basically limited by the signal to noise ratio. The signal to noise ratio in fluorescence microscopy is mainly determined by the quantum efficiency, dynamic range of the fluorophore emission, aberrations of optical elements and sampling.

2.2 High-speed cameras

Measurements of weak spatially distributed light signals at high frame rates require special detection systems, that are mostly based on CCD cameras (Charge Coupled Devices). CCD cameras are commonly used for slow speed microscopy. They basically consist of an array of silicon diode photosensors that are called pixels. If incident photons have sufficient energy to create electron-hole pairs, the mobile charges are trapped within one pixel by electrodes. Proper clocking of the electrodes shifts the produced charge pattern down into the storage area, an area that is masked to prevent further illumination. For the readout process, the stored charge is sequentially transferred through parallel registers to a linear serial readout register where charge packets are converted to a digital signal by the ADC (Analog to Digital Converter). A weakness of conventional CCD cameras is their serial readout and that low noise performance can only be achieved at the expense of slow readout speeds. In order to overcome this limitation, different signal amplification techniques are applied in high-speed CCD cameras that are explained in the following.

The principle of an ICCD (Intensified CCD) camera will be explained since it was part of the setup that was successfully used by Petty at al. for spatiotemporal imaging, see section 2.3. The principle of an EBCCD (Electron Bombardment CCD) camera will be summarized since it was used to compare the sensitivity of our setup. As basis for the detector characterization in the first part of this thesis, the function principle of an EMCCD (Electron Multiplying CCD) camera is explained in greater detail.

2.2.1 ICCD

By combining an image intensifier with a CCD camera, high sensitivity and exposure times in the nanosecond range are achieved, due to fast electronic gating of the intensifier. The image intensifier is an evacuated tube which comprises the photocathode, a microchannel

plate and a phosphor screen. Incident photons generate electrons at the photocathode which are then accelerated towards an electron multiplier, called microchannel plate. It is composed of a series of honeycomb glass channels with resistive coating that enable the production of secondary electrons from the channel walls. The multiplication factor (up to 10^4) depends on the voltage that is applied across the microchannel plate. The output of the image intensifier is coupled to a CCD either by fiber coupling or lens coupling, depending on the required coupling efficiency and flexibility. The spectral response (QE) is primarily determined by the photocathode material. A Gen2 intensifier, which is used in the setup of Petty et al., incorporates a Bi or multi alkali photocathode has the best response in the UV range. However, the QE is typically less than 40%.

The extremely fast gating of an ICCD is realized by switching between high negative voltages swapping the electrons from the cathode, and small positive voltages, that prevent electrons from crossing the gap into the intensifier. For gating times below the ms range, it is important to use a phosphor type with a fluorescence lifetime shorter than that, e.g. P46 Phosphor.

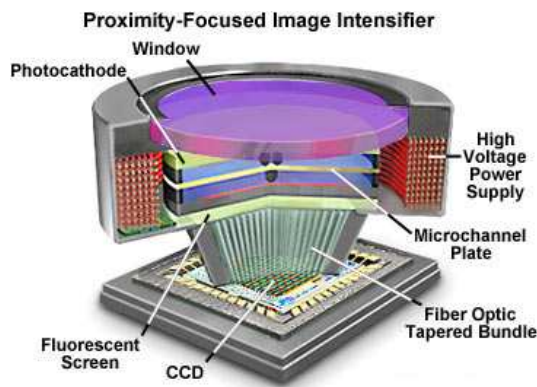


Figure 2.3: Principle of an ICCD camera [7]. Electrons generated at the photocathode are multiplied in the microchannel plate and produce photons at the phosphor screen which are detected by a CCD.

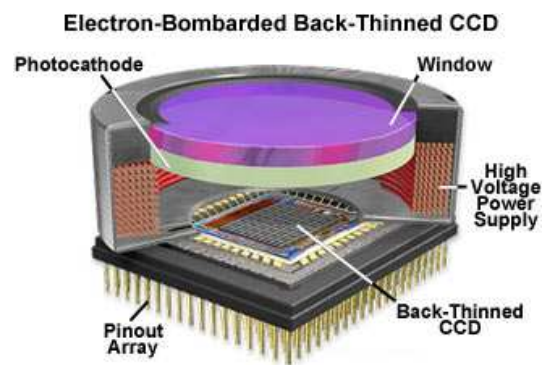


Figure 2.4: Principle of an EBCCD camera [7]. Electrons generated at the photocathode are accelerated across a gap and detected by a back-thinned CCD.

2.2.2 EBCCD

Similar as an ICCD, an Electron Bombardment CCD camera detects photons with a photocathode. The released electrons are then accelerated across a gap and generate multiple charges by impact ionization (a few hundred). Compared to ICCDs the gain is smaller and they can not be gated within nanoseconds.

2.2.3 EMCCD

The recent development of EMCCDs (Electron Multiplying CCD) allowed to replace the more expensive ICCDs in most applications. EMCCD cameras allow high sensitivity measurements at high frame rates by an additional register, where signal electrons are amplified above the readout noise level prior to the readout. The detailed function principle is described with specifications of the Andor IXON DV 860. The characterization of this camera will be more detailed since it was used for most experiments.

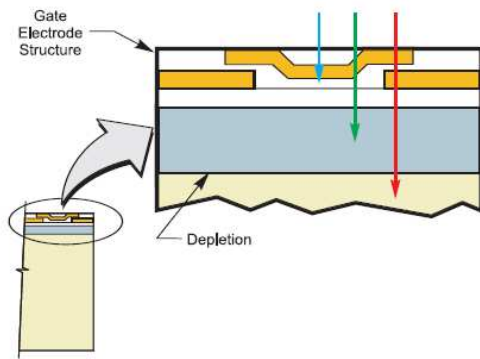


Figure 2.5: Cross-section through front-illuminated CCD chip. Incident light in the blue region is absorbed by the electrode structure before generating electrons in the depletion region.

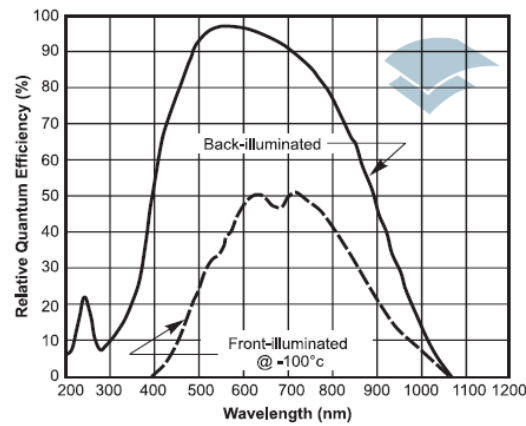


Figure 2.6: Spectral QE of front and backilluminated CCD chip.

2.2.3.1 Quantum efficiency (QE)

The high QE of a backthinned EMCCD compared to an ICCD justifies the assumption that a high-speed microscopy setup, comparable to the one established by Petty et al., can be built-up based on an EMCCD. The quantum efficiency describes the spectral response of a CCD, which is determined by the ability of the photons to be absorbed in the depletion region of the detector. The depletion region is a nonconducting layer sandwiched between the p- and n-doped regions. Electrons are trapped by the electric field produced by the electrodes bordering the pixel. If the chip is illuminated from the front as it is shown in Fig. 2.5, light can also be absorbed by the electrode structure. This effect is dominant in the blue spectral region. Below 350nm, almost all photons get absorbed by the electrode structure. This can be avoided by illuminating the chip from the back. Additionally, the silicon on the back of the chip is thinned until it is transparent, which corresponds to a thickness of about 10-15 μm . Coating of the window can further increase the QE in a

certain spectral range. The exact camera type used in the measurements in the Langowski lab was DV 860 DCS-BV, which is a backilluminated chip with a 550nm anti-reflection coating. It was therefore not optimized for applications in the UV. However, the QE at 405nm and 450nm, see Fig. 2.6, where fluorescence emissions are to be detected in this application, is still higher than the QE of a Gen2 intensifier which is typically $\approx 20\%$.

2.2.3.2 Charge transfer, electron multiplication and readout process

The charge packages within pixels are shifted by clocking the pixel bordering electrodes, as it is illustrated in Fig. 2.8. Vertical clocking transfers charge from the image region into the storage region of the chip, see Fig. 2.7. Vertical shift speeds limit the exposure times in EMCCDs and can be chosen by software as a shift time. Shifting 128 rows into the storage area takes at least $12.8\mu s$. Shift times become relevant if they are of the same order of magnitude as the exposure time. Light can still produce charge during the shift process and can therefore destroy an image. For the shortest exposure time of $20\mu s$, the last row would be exposed about twice as long as the first row. A list of shift times depending on shift speed is shown in Tab. 2.1.

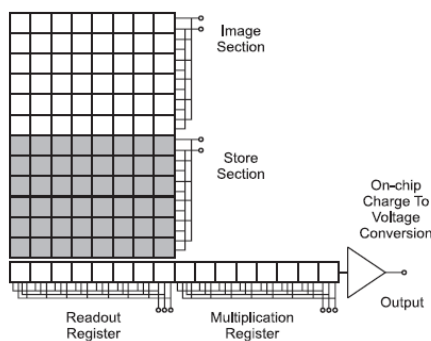


Figure 2.7: Structure of an EMCCD chip. The charge pattern which is produced in the image section is transferred into the storage area. An additional register amplifies the signal prior to the readout.

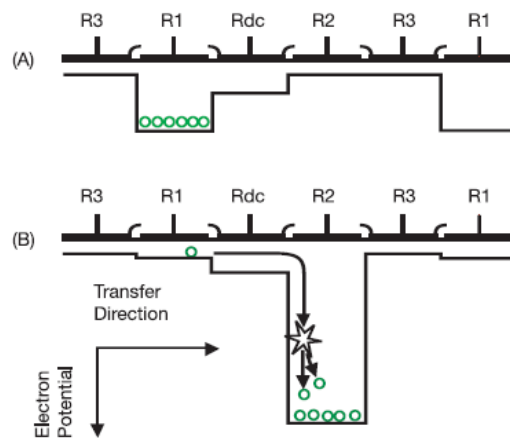


Figure 2.8: Illustration of a) charge shifting and b) electron multiplication process depending on the voltage that is used to clock the electrodes.

To ensure efficient charge transfer the shifttime has to be appropriate to the shift voltage which can be independently chosen by software. An unsuitable combination of shift speed and voltage leads to circular blemishes in the image, as presented later.

| shift speed | shift time per frame |
|-------------|-------------------------|
| $0.1\mu s$ | $12.8\mu s$ |
| $0.2\mu s$ | $25.6\mu s$ |
| $0.3\mu s$ | $38.4\mu s$ |
| $0.5\mu s$ | $128\mu s$ |
| ... | ... |

Table 2.1: Time required to shift the image into the storage area, depending on the shift time.

The horizontal shift speed, which determines the readout process and thus the frame rate, can be chosen as a readout rate by software. It corresponds to the rate by which the signal is digitalized by the ADC. At a readout rate of 10MHz, it takes 1.6384ms to readout a frame with 128^2 pixels, while the same process takes 16,4ms at a readout rate of 1MHz, see Tab. 2.2.

| readout rate | readout time per pixel | readout time per row | readout time per frame |
|--------------|---------------------------|-------------------------|---------------------------|
| 10kHz | $0.1\mu s$ | $12.8\mu s$ | 1.64ms |
| 5kHz | $0.2\mu s$ | $25.6\mu s$ | 3.28ms |
| 3kHz | $0.33\mu s$ | $38.4\mu s$ | 5.47ms |
| 1kHz | $1\mu s$ | $128\mu s$ | 16.4ms |

Table 2.2: Time required for the readout process depending on the readout rate

The analog to digital conversion (ADC) is specified by the number of electrons that correspond to one ADC count as well as the resolution in bits which determines the number of gray levels available. The camera type used in our setup has a 14 bit resolution meaning that $2^{14} = 16384$ is the maximum gray level value or that 16384 counts per pixel are the saturation level of the ADC. Using the default conversion rate (18 electrons are converted to 1 count, see Fig. 2.9), the saturation level corresponds to 294912 electrons. An electronic offset of about 950 counts or 17100 electrons has to be subtracted to get the real saturation level. If weak signals have to be resolved, the ADC conversion factor can be changed by applying a pre-gain. This has to be done in the acquisition settings depending on the required dynamic range of the application. Applying a pre-gain of 4.9 decreases the saturation level to $16384 * 18/4.9$ electrons, what reduces the dynamic range but allows a finer resolution of weak signals. Consequently, applying a pre-gain increases the contribution of readout noise. If a pre-gain of 4.9 is applied at a readout rate of 1MHz, the readout noise of 23 electrons (see Fig. 2.9) corresponds to 6 counts, while it corresponds to 1 count without a pre-gain. For the highest dynamic range, the pre-gain should be set such that

the highest gray value corresponds to the well storage capacity of one pixel.

In order to achieve the highest sensitivity or lowest noise contribution it is recommended by the manufacturer to set the pre-gain such that the readout noise is much less than 1 count of the ADC.

| A/D Rate | EM = electron multiplication Con = conventional | Options (✓) | CCD Sensitivity eles per A/D count | Single Pixel Noise electrons | Base Level (Counts) |
|----------|--|----------------|---------------------------------------|---------------------------------|------------------------|
| 10 MHz | 14 bit EM amplifier | ✓ | 18 | 70.57 | 952 |
| 5 MHz | 14 bit EM amplifier | ✓ | 18 | 46.21 | 952 |
| 3 MHz | 14 bit EM amplifier | ✓ | 18 | 29.41 | 935 |
| 1 MHz | 14 bit EM amplifier (D only) | ✓ | 18 | 23.4 | 967 |

Figure 2.9: The readout noise depends on the readout rate, which is called single pixel noise. The CCD sensitivity is determined by the AD conversion rate. Without applying a pre-gain, 18 electrons correspond to 1 count.

The electron multiplication (EM) takes place in a separate register where charges are shifted with voltages of 20 – 50V leading to charge production by impact ionization, see Fig. 2.8. The probability for the multiplication increases with voltage and decreasing temperature since impact ionization is more efficient for lower phonon scattering.

The EM gain increases the dynamic range as long as the full well capacity of the EM register can accommodate the amplified signal. When the gain reduces the readout noise below the single photon level, the dynamic range decreases. This limit is already reached for a real gain factor of 23 at a readout rate of 1MHz.

2.2.4 Noise contributions of CCD based cameras

The sensitivity limit of a detection system is set by its noise level. Digital cameras are therefore often compared by their noise figures. In order to get highest possible sensitivity for each application, one has to be aware of the different noise contributions in a detector, especially their dependency on temperature and readout speed. The total noise is the sum in quadrature of single noise sources. The inherent photon noise that arises from the stochastic nature of the photon flux is proportional to \sqrt{n} and often called shot noise. Additionally, noise electrons can be generated thermally, by charge transfer induced impact ionization, during the amplification process and by the readout process. Each noise contribution will be explained in the following.

2.2.4.1 Dark current

The so called dark current consists of electrons that are thermally generated on the chip. While moderate cooling in conventional CCD cameras reduces dark current below the shot noise, this is not sufficient for EMCCD cameras that can even detect single photons. One can classify two kinds of dark current. The common or traditional dark current is proportional to the exposure time and is regarded as negligible for short exposure times and sufficient cooling. Readout dark current means dark current produced during the readout process which can be mostly ignored because it contributes less than the readout noise. However in case of exposure times comparable to readout times and a detection efficiency that is not limited by readout noise, it contributes even more than exposure time associated dark current. If one is interested in dark current for short exposure times in EMCCDs, one can not simply extrapolate a long exposure measurement to exposure times below 1s, since the readout dark current dominates at these times. Both types of dark current can be reduced by cooling, while another source of noise, the clock induced charge generation increases with decreasing temperature. Thus, cooling has to be optimized depending on the application.

2.2.4.2 Clock Induced Charge (CIC)

In order to shift the charge pattern down into storage area, the electrodes bordering the pixels are clocked with a certain frequency and voltage. This is essentially the same process as for the electron multiplication, apart from much higher voltages being applied in the latter case. Therefore additional electrons are produced by the charge shift process, more efficiently at lower temperatures.

In order to minimize this effect, the clocking voltage and speed have to be chosen carefully. On the one hand faster clocking decreases CIC production by reducing the acceleration time, but charge transfer efficiency will decrease as well. Higher voltages that are then needed to improve charge transfer efficiency increases the CIC. Low charge transfer efficiency can degrade spatial resolution for bright signals due to lower well depths and thus both effects have to be balanced. According to Andor tech notes, CIC only sets the detection limit below -95°C , where it is supposed to exceed photon noise. Although the EMCCD used this project was never cooled below -90°C the CIC was found to contribute significantly even at higher temperatures.

2.2.4.3 Readout noise

Readout noise results from the analog to digital conversion that introduces noise by quantifying the charge package with a discrete count value. The higher the readout speed the higher is the required bandwidth of the ADC and thus the readout noise. The readout

noise is proportional to $N_{fullwell}/2^n$ with $N_{fullwell}$ being the full well capacity and n being the number of bits of the ADC. If the amplification is low, the readout noise dominates as it does for slow scan CCD cameras.

2.2.4.4 Electron amplification noise

The noise that originates from the stochastic nature of the amplification process is represented by the noise factor F , and is independent of the amplification of the noise produced before the amplification,

$$F^2 = \frac{(\delta_{output})^2}{G^2(\delta_{input})^2}. \quad (2.1)$$

2.2.4.5 SNR

The resulting signal to noise ratio can be calculated dividing the signal $S = G * QE * P$ by the total noise N , with G , QE , P being the gain factor, quantum efficiency and the number of incident photons, respectively:

$$\frac{S}{N} = \frac{G * QE * P}{\sqrt{f^2 * G^2(QE * P + (\delta_{dark})^2 + (\delta_{cic})) + (\delta_{readout})^2}} \quad (2.2)$$

It is noteworthy that photon noise ($\sim \sqrt{P}$), dark noise (δ_{dark}) and clock induced charge noise (δ_{cic}) are amplified by gain factor and amplification noise factor (f), division by the gain factor G leads to:

$$\frac{S}{N} = \frac{QE * P}{\sqrt{f^2(QE * P + (\delta_{dark})^2 + (\delta_{cic})^2) + \frac{(\delta_{readout})^2}{G^2}}} \quad (2.3)$$

This shows that sufficient gain can theoretically make readout noise negligible. If dark current is eliminated by cooling, only the clock induced charge noise and the photon shot noise remain [8].

2.2.4.6 Camera modes

The camera can operate in different modes that can be chosen in the acquisition settings. Depending on these modes, the exposure time is either coupled to the readout, as in the frame transfer mode, or can be controlled independently, as in the non frame transfer mode. In order to choose the right camera mode one should consider the horizontal and vertical shift times per row as illustrated in Tab. 2.1 and 2.2.

The *frame transfer mode* is optimal for fast kinetic cycles and exposure times larger than 2ms. In this mode, the exposure times already begins as soon as the the previous image has been shifted down into the storage area. Therefore exposure and readout are coupled which leads to a fixed cycle time and a minimum exposure time that is equal to the minimum readout time, see Tab. 2.2. The maximum frame rate at full spatial resolution of about 550 frames/s can therefore be achieved in this mode. As mentioned above, using the *non frame transfer mode* means basically that exposure time and readout time can be chosen independently. This is crucial for exposure times shorter than 1.65ms. After the exposure the charge pattern is shifted down into the storage area and is then read out in the preferred speed while new charge is produced on the image area, until the next exposure time starts. However, right before each exposure the chip is cleaned of charges produced in between two exposures. This mode saves a lot of memory if continuous data acquisition is not indicated. The minimum time for one cycle is determined by the time needed for the read out of 128 rows, see Tab. 2.2.

While the camera modes explained above are combined with the option *kinetics* for the acquisition of timeseries, the option *fast kinetics* allows the shortest exposure times but requires an additional optical part like an image splitter. Since a mechanical shutter is too slow, this allows partial chip illumination in order to prevent exposure of unused pixels that are used as additional storage area. Continuous data acquisition is only possible for one series of subimages, in which the chip has been divided. Exposure times depend on the shift speed and size of the illuminated area. For a separation into two subimages this corresponds to a minimum average exposure of $6.5/2\mu\text{s}$. However, exposure times as short as $1\mu\text{s}$ can be chosen by software.

In general, using exposure times comparable to the shift time should be avoided since the effective exposure time depends on row number.

2.3 Setup established by Petty et al.

Differences in experimental setups potentially effect the results. This diploma thesis project included the reproduction of results published by Petty et al. by using a comparable, but not identical setup. Thus, the setup established by Petty et al. will be described as detailed as it was found in the literature.

The temporal NAD(P)H-oscillations and Ca^{2+} -spikes have been measured by microfluorometry. For that purpose, the bottom port of an inverted microscope (*Zeiss*) with quartz condenser and objectives was coupled to a cooled PMT (Photomultiplier Tube, D104 *Photon Technology*, Lawrenceville, NJ). The signal of the PMT was displayed with an oscilloscope.

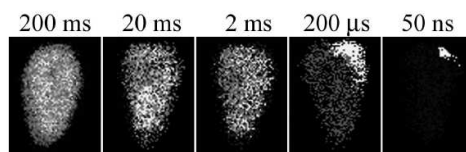


Figure 2.10: Wave acquisitions at different exposure times. A Ca^{2+} -wave is recognizable at exposure times below $200\mu\text{s}$ [2].

The amplitude of the NAD(P)H-oscillations was $\approx 5\%$ of the baseline. For some acquisitions the amplitude of the oscillation was increased by stimulation with PMA (phorbol 12-myristate 13-acetate, $10\mu\text{M}$ for 15 min), $\text{INF-}\gamma$ (25ng/ml) or the combination of FMLP ($0.5\mu\text{M}$) and melatonin (150mg/ml).

For acquisitions of NAD(P)H waves, an AttoArc HBO 100W mercury lamp was used for illumination. The bottom port of an inverted microscope (*Zeiss*) was fiber-optically coupled (endoscope like) to an Actron-150 spectrophotometer (*Acton Instruments*). The use of an image preserving fiber optic bundle (fiber-optic face plate) increases the light collection efficiency up to 10 times [9]. The exit side was connected to an image intensifier tube (Gen2), attached to a Peltier-cooled ICCD camera ((I-MAX-512), *Princeton Instruments*). For acquisitions of the NAD(P)H-waves the contrast was improved by taking images at the maximum of the temporal oscillations. Stimulation leading to an increased amplitude of the oscillations was used to increase the contrast of wave acquisitions. Exposure times of 10ms were sufficient to recognize the NAD(P)H-wave, see [10], but most published images have been taken with 100ns exposure times. In case of Ca^{2+} -waves, acquisitions were taken during the expected occurrence of a Ca^{2+} -spike. No spatiotemporal event was recognizable for exposure times larger than $200\mu\text{s}$ [2]. Exposure times in the nanosecond range are only possible with an ICCD camera, as explained in section 2.2.1. Thus, the effect of the exposure time on image blurring will be highlighted in the next section.

2.3.1 How short must exposure times be for wave detection?

Randomization of the signal due to wave motion can be prevented, if the exposure times are shorter than the time it takes for the wave to propagate a distance comparable with the minimum resolvable separation distance (e.g. according to the Rayleigh criterion, see section 2.1.1). Using

$$d_{\text{Rayleigh}} = \frac{0,61\lambda}{NA} \approx 180\text{nm}, \quad (2.4)$$

as the minimum resolvable separation for $\lambda = 405$ nm (emission wavelength of the calcium dye indo-1) and $NA = 1,4$ (in Petty setup) one obtains:

$$\Rightarrow t_{exp} = \frac{d_m}{v_{wave}} = \frac{180 \text{ nm}}{180 \text{ nm/ms}} \approx 1 \text{ ms} \quad (2.5)$$

for the Ca^{2+} -wave and ≈ 2.5 ms for the 4 times slower NAD(P)H-wave respectively. For shorter exposure times the waves must be stationary. However, Petty et al. found experimentally that the contrast of NAD(P)H waves increases for even shorter exposure times. Imaging of Ca^{2+} -waves requires exposure times shorter than $200 \mu\text{s}$ and the contrast is still improving down to a illumination time of 50ns, see Fig. 2.3.

Thus, in the setup of Petty et al., blurring of the signal is faster than the mechanism of wave propagation.

In the following, the influence of diffusion on image blurring of Ca^{2+} -wave acquisitions is discussed. To our knowledge, measurements of the diffusion constant of Ca^{2+} -indo-1 complexes in the cytosol have not been done so far. The diffusion coefficient of free Ca^{2+} underneath the membrane $D = 4 * 10^{-11} \frac{\text{m}^2}{\text{s}}$ [11] can be regarded as a lower limit for the diffusion of Ca^{2+} -indo-1 complexes, due to the high calcium binding capacity of the cytosol. By assuming a 2D geometry due to the flatness of an adherent cell, using

$$d_{rms}^2 = 4Dt \quad (2.6)$$

leads to

$$t_{exp} = \frac{d_{rms}^2}{4D} \approx 200 \mu\text{s} \quad (2.7)$$

However, as displayed in Fig. 2.3, the signal still spreads on smaller timescales. As an upper limit for diffusional blurring, the self diffusion coefficient of H_2O can be used leading to $t_{exp} \approx 8 \mu\text{s}$.

This implicates that even if diffusion of Ca^{2+} -indo-1 complexes was as fast as self diffusion of H_2O , one should obtain a blurring free picture for exposure times of $8 \mu\text{s}$. The fact that a minimum resolvable separation distance, as defined in Eq. 2.4, assumes optimal sampling further justifies the use this estimation as an upper limit for image blurring.

Thus it is likely that diffusion is not the only process leading to leading to the blurred images on timescales below $1 \mu\text{s}$. However, no plausible biophysical mechanism has been proposed so far.

Another question might be why the center of the blurred wave is not saturated. This can be explained by the emission spectrum of indo-1, see Fig. 4.2(b), which shows a binary response to calcium concentrations. Therefore, above a certain calcium concentration, the emission intensity no longer represents the calcium concentration.



Figure 2.11: Differential interference contrast image of blood cells showing macrophages (left), erythrocytes (right) and an adherent migrating neutrophil (middle).

Furthermore, it is worth to mention, that it is not trivial to achieve a comparable gray level or false color representation of images, that significantly differ in their data histograms due to a large range of exposure times.

2.4 Neutrophil Granulocytes

Most experiments that are presented later were done with neutrophils, a white blood cell type which was isolated from whole blood. The main contents of human blood are plasma, trombocytes, red blood cells (erythrocytes) and white blood cells (leukocytes). Next to lymphocytes, monocytes and macrophages, the most abundant type of leukocytes with about 70 percent are neutrophil granulocytes. Together with eosinophil and basophil granulocytes they form the class of polymorphonuclear cells (PMNs). Neutrophils play an important role in the human innate immune system. The average half-life of a neutrophil circulating in the blood is only a few hours. In case of activation e.g. by cytokines, they migrate towards the infection by a process called chemotaxis. Chemotaxis means movement directed by a gradient of diffusing signaling molecules e.g. cytokines like FMLP (f-met-leu-phe) or interferon- γ that are expressed by other immune cells like mast cells and macrophages. Since neutrophils are capable of ingesting a microorganism they are called phagocytes. Invading pathogens can be killed by hydrolytic enzymes that are stored in cytoplasmic granules, or the formation of reactive oxygen species, called *respiratory burst*. The in vivo behavior of neutrophils does not strongly depend on adjacent cells, making them as semi-autonomously as tumor cells. They are therefore well suited for in vitro studies.

2.5 Cell polarization, migration and shape oscillations

Cell migration is a very basic cell function required for many processes e.g. tumor cell invasion and metastasis or chemotaxis of immune cells towards the site of infection. Since the phenomena which are subject of this thesis were observed in polarized migrating neutrophils (see next sections), it is crucial to ask how the observation of these phenomena depend on the varying morphological states or migration modes that neutrophils can perform. Especially the role of shape oscillations needs to be investigated. The following section explains the relation of polarization, migration and shape oscillations in neutrophils, following the review of Ehrenguber et al. [12].

A morphological change called polarization is crucial for the motility of neutrophils, which are spherical in the resting state. However, this process is known to be independent of adherence since polarized cells are observed in suspensions as well. Morphological polarization involves the formation of asymmetric cell extensions, which are classified into lamellipod and pseudopod extensions. Lamellipodia are thin, clear, veil-like extensions that are formed early after stimulation while the cell remains in a spherical morphology (see Fig. 2.12 B). The polarized morphology is developed by the formation of pseudopods (see Fig. 2.12 C) which are of moderate width compared to cell dimensions, see references in [12]. The process of migration involves repetitive extension of lamellipodia at the leading edge, the formation of adhesion sites, contraction of the cell body, and the release of trailing adhesion sides. Additionally, if cells migrate through tissues, they must be able to perform proteolytic activity in order to work themselves through the extracellular matrix.

Oscillatory shape changes of neutrophils have been reviewed in [12], where it is concluded that shape oscillations are a fundamental feature of neutrophil migration. Cell shape changes can be characterized by changes in cell volume and changes in cell symmetry. The volume of a neutrophil at physiological osmolarity is $\approx 300\mu\text{m}^3$, but their surface is known to increase by a factor of 2.6 after lysis [13], which is a commonly used isolation method described in section 4.1.1.1. However, pure volume effects were not reported in the studies of shape changes by previous investigators that are described in the following. References can be found in [12].

In the absence of chemotactic gradients, neutrophils show pseudopod extensions and discrete direction changes that occur with a constant frequency. This behavior is not changed by chemotactic stimulation. Furthermore, in 75% of unstimulated spontaneously migrating cells, shape oscillations with periods of 8-10s and 20-30s have been found.

When neutrophils migrate within a chemotactic gradient, their velocity was observed to oscillate between 10 and $30\mu\text{m}/\text{min}$. The oscillation period was 50-55s and corresponds to mean transit time between discrete changes in direction. During their periodic bursts of speed they are described to obtain a more flattened shape with an extended leading lamellipod that forms contact with the surface, which then, after a slight phase lag, rapidly moves the cell body over the immobile contacts.

Similarly, neutrophils in suspension stimulated with chemoattractants exhibit sinusoidal light scattering oscillations with a period of ≈ 8 s caused by periodic lamellipod extension and retraction cycles, see Fig. 2.12 D). The collective shape oscillations observed in suspension are damped with a decay time of 40-60s, possibly due to desynchronization of single cells. The decay time of damped oscillation in suspension corresponds to the time between direction changes of crawling cells. Although it is not known whether the oscillations seen in suspension are due to the same process that occur on a surface, the fact that both, lamellipod formation and polarization occur without adherence or another stimulus suggests these phenomena to be an intrinsic property of a neutrophil. Adherence could be a natural event to enable shape oscillations. Both observed periods (8s and 50s) could be related to polymerization cycles of actin, see references in [14].

The described periodic process of migration was found to be accompanied by repetitive calcium signals or oscillations in neurons, fibroblasts, tumor cells, and neutrophils, see references in [15]. Since calcium serves as multifunctional messenger in cells, these oscillations could potentially coordinate the cyclic temporal features of cell migration such as actin assembly and integrin regulation.

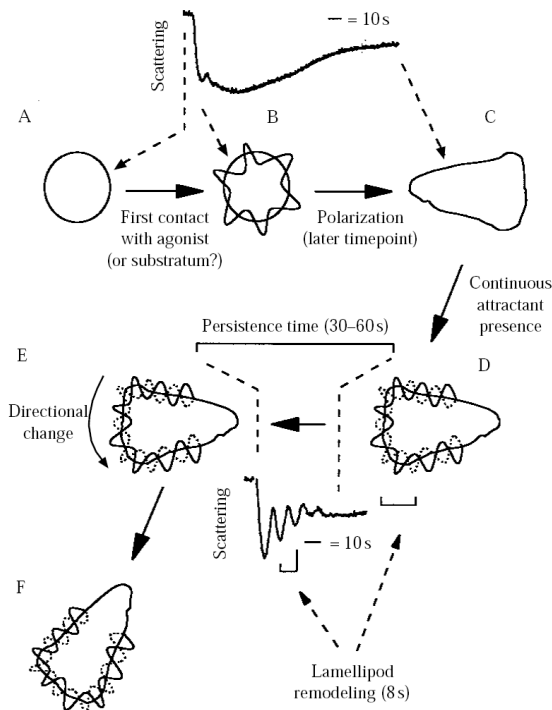


Figure 2.12: Hypothetical role of shape oscillations in neutrophil migration compared with real time tracings of cell suspensions measured with 90° -light scattering. Resting cells are spherical (A) and develop lamellipodia upon stimulation (B), pseudopod formation polarizes the cell (C). In suspension, stimulation leads to 8s oscillations (D) possibly due to surface contact. The cell migrates (E) with a persistence time of 50-60s before it changes direction (E) followed by another straight-line movement, see [12].

2.6 NAD(P)H-metabolism and autofluorescence

An important part of this thesis is concerned with microscopic measurements of cellular autofluorescence in neutrophils, which is assumed to result mainly from NADH and NADPH, if measured with a specific filter set.

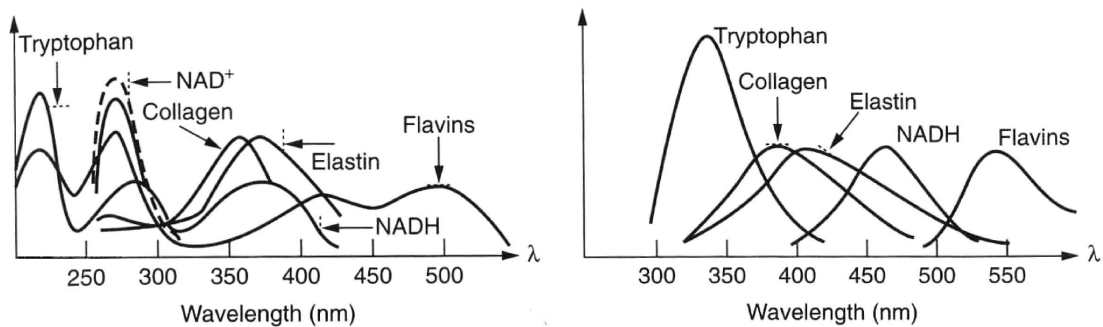
NADH is the reduced form of NAD^+ (nicotinamide adenine dinucleotide) which is produced during glycolysis and the citric acid cycle.

NADH is oxidized by an electron transport chain during aerobic respiration, leading to a substantial ATP production (36 molecules of ATP per cycle compared to 2 molecules per glycolysis cycle). Glycolysis converts glucose to pyruvate which then enters the citric acid cycle in aerobic conditions or glucose is converted to lactate under anaerobic conditions. Under anaerobic or hypoxic conditions glycolysis is the only source of ATP and it is known to be the main energy producing pathway in neutrophils. Similarly, malignant tumor cells have glycolytic rates that are up to 200 times higher than glycolytic rates in healthy cells, a fact that is used in positron emission tomography to locate active tumors areas with a radioactive form of desoxyglucose. Furthermore, glycolysis is known to be a potentially oscillating reaction driven by feedback activation and inhibition of glycolytic enzymes, especially of its key enzyme phosphofructokinase, which is activated by ADP and inhibited by ATP. This can explain oscillating levels of NADH [16].

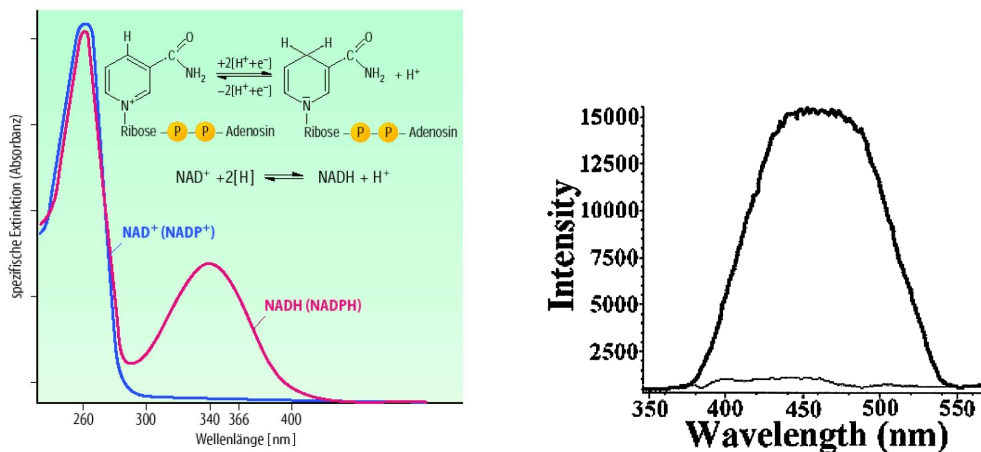
NADH causes a major fraction of intrinsic tissue fluorescence with an absorption maximum at 340nm and an emission maximum at 460nm [17]. Its oxidized form NAD^+ is nonfluorescent. The fluorescence results from the reduced nicotinamide ring, see Fig. 2.13(b). Since NADH and NADPH can not be distinguished by the emission wavelength, it will be referred to as NAD(P)H in the following. The molecular brightness or quantum yield of NAD(P)H fluorescence depends on the chemical environment. Quenching (decrease of emission) can occur dynamically by collision with the adenine moiety and protein binding can increase the quantum yield fourfold due to less quenching by adenine [18].

Other intrinsic cellular fluorophores include aromatic amino acids (tryptophane, tyrosine and phenylalanine) and enzyme cofactors (NADH, flavins or derivatives of pyridoxyl). Collagen, elastin lipo-pigments and porphyrins are also sources of fluorescence in intact tissues [18]. Spectral characterization of intrinsic tissue fluorescence can be used to identify cancerous or disease states [17]. Typical excitation and emission spectra are presented in (see Fig. 2.13(a)).

Fluorimetric measurements of NAD(P)H autofluorescence are an accepted method to monitor the metabolic state of living tissues. In order to link the measured autofluorescence of neutrophils to cell metabolism, it was shown that the presence of the metabolic inhibitors 2-deoxy-D-glucose (100mM) and sodium azide (3%) reduced the intensity by 95%, see Fig. 2.13(c)[10].



(a) Absorption (left) and emission spectra (right) of autofluorescence in living tissues [17].



(b) Absorption spectra of NAD^+ and NAD(P)H [19]. NADH and NADPH have equal spectral properties.

(c) Autofluorescence emission of neutrophils results mainly from NAD(P)H . The application of metabolic inhibitors dramatically reduces the autofluorescence emission [10].

Figure 2.13

2.7 NAD(P)H-oscillations and waves

Oscillations of NAD(P)H autofluorescence were observed in three different periods. A period of 3 – 4 minutes was reported in spherical but adherent neutrophils, oscillations with a period of 20s have been observed in polarized adherent neutrophils, and a period of 10s was found if polarized adherent cells which were further activated by cytokines [20, 21], see fig. 2.14. Migration or shape changes of the cells accompanying the NAD(P)H oscillations have not been studied simultaneously in these experiments where measurements have been done without spatial resolution by using a PMT. However, it was reported later that these oscillations were observed in migrating cells [1]. The temporal oscillations were shown to be accompanied by propagating waves.

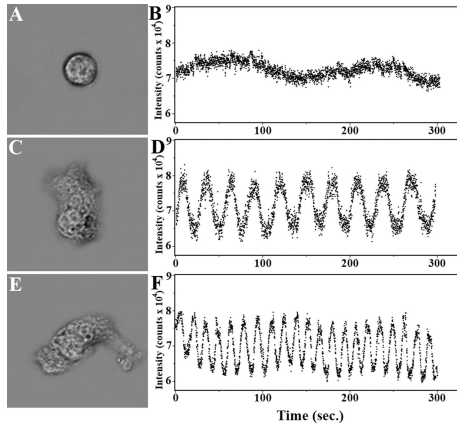
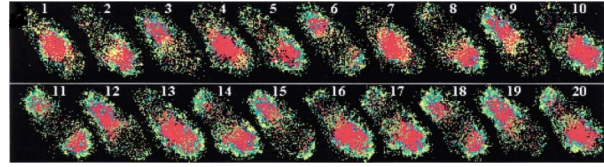
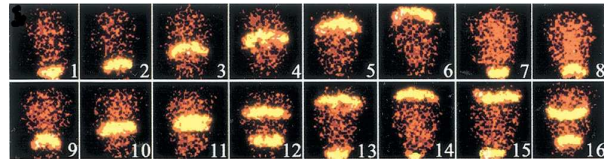


Figure 2.14: NAD(P)H oscillations of different periods were observed in spherical, polarized and activated neutrophils [20, 21].



(a) Nad(p)h-wave, exposure time= 10ms, interframe time=90ms, time between two frames in this sequence is 450ms, see [10].



(b) Nad(p)h-wave, exposure time= 100ns, interframe time=100ms, [4].

Figure 2.15

NAD(P)H-waves have been reported in different morphologies too. Concentric waves were observed in spherical adherent cells while longitudinal waves ($v \approx 50 \mu\text{m}/\text{s}$) with a period of 20s were observed in 100% of polarized unactivated cells. Splitting waves, propagating in opposite directions have been observed in cells stimulated with various chemoattractants or activating substances, see [4] for details. Again, migration was not mentioned to accompany the phenomenon [10, 4, 5].

Similar NAD(P)H oscillations have been observed in macrophages [22] and HT-1080 fibrosarcoma cells [23]. As in neutrophils, oscillations with a period of 3 minutes were found for resting cells, and 20s oscillations for polarized migratory cells while no oscillation was observed in densely grown, confluent cells.

2.8 Ca^{2+} -signaling

Rises in intracellular calcium concentrations are well known to trigger a wide range of physiological processes including gene expression, secretion of hormones, chemotaxis and apoptosis either directly or as second messenger in signaling cascades. Simultaneous control of these processes requires a higher spatiotemporal organization level as an overall increase and decrease of concentration. Temporal oscillations and spatiotemporal waves of intracellular calcium have been found in various cell types. Information leading to specific cell functions is suspected to be encoded in amplitude, frequency or pulse shape modulation of temporal signals or different spatiotemporal propagation pathways and mechanisms [24, 25].

Important participants in Ca²⁺-signaling are Ca²⁺-pumps in the plasma membrane (Ca²⁺-ATPases) which consume a large amount of energy in order to maintain a steep gradient across the membrane with a concentration difference of $\approx 10^{-4}$ M. Similar pumps are located in the membranes of endoplasmatic reticulum (ER) and mitochondria which pump Ca²⁺ back into these intracellular stores. Ca²⁺-release from stores is mostly described as mediated by IP₃ or Ryanodine. Furthermore, additional calcium stores were found in the plasma membrane of neutrophils that can release calcium upon stimulation by a yet unknown mechanism, which was found to be mostly accompanied by depolarization [26]. Another protein that transports calcium out the cell with high rates is the Na²⁺/Ca²⁺-exchanger located in the plasma membrane which can change its transport direction at high depolarizations. Transmembrane calcium influx is mainly mediated by voltage gated Ca²⁺-channels, which play a key role for calcium activated processes that are accompanied by depolarization. Calcium influx triggered by low depolarizations through T-type channels will play a key role in the Ca²⁺-wave model, which is introduced in the third part of this thesis.

2.8.1 The low voltage gated T-type Ca²⁺-channel

Among six different types of voltage gated Ca²⁺-channels in human cells that are classified according to their activation and inactivation dynamics, threshold potential and sensitivity to Ca²⁺-antagonists, there is only one channel type that activates at low depolarizations of transmembrane potential. The originally called low-voltage-activated (LVA) channels display a transient activation, which motivates the name T-type calcium channels, followed by fast inactivation and a slow recovery from inactivation into a closed state [27]. Three subtypes are known to coexist, which are encoded by separate genes [28]. The low threshold potential of T-type Ca²⁺ channels favors their role in processes that are excitable by relatively small variations in membrane potential such as caused by a localized ion current. They have been identified as pacemakers in neurons where they can generate low threshold spikes that then lead to burst firing and oscillatory behavior. The pacemaking function is especially prominent in the thalamus where pathological changes of these oscillations have been implicated in a wide range of neurological disorders [28]. Apart from nervous tissues T-type channels are expressed in heart, kidney, smooth muscle, sperm, and many endocrine organs [28].

2.9 Ca^{2+} -oscillations and waves

2.9.1 Temporal Ca^{2+} -oscillations

Different shapes of Ca^{2+} -oscillations have been observed possibly due to different mechanisms [25]. In migrating neutrophils, Jaconi et al. [29] observed sinusoidal Ca^{2+} -oscillations of varying periods with a mean of 28 ± 5 s and an amplitude of 70% relative to the baseline. In contrast, Petty et al. report repetitive baseline Ca^{2+} -spikes with a duration of 200ms.

Apart from the possibility of more or less independent phenomena being superimposed, differences in signal shape can result from the detection method. Depending on the on- and off-rate of the calcium sensor, the appearance of a spiky signal could be smoothed. Additionally, the detector integration time is usually more than 200ms, which decreases the spike amplitude due to averaging. A concentration peak will be missed very likely if ratio imaging is applied which is realized by automatized filter changes. The almost perfectly noiseless appearance of the spikes published by Petty et al. suggests the use of a threshold, when displaying the data with an oscilloscope.

2.9.2 Types and mechanisms of spatiotemporal Ca^{2+} -waves

As reviewed by Jaffe [30], calcium waves can be classified by propagation speed and underlying propagation mechanism. Slow calcium waves with a velocity of $0.1\text{-}1\mu\text{m/s}$ (at 20°C) are likely mechanically propagated via stretch sensitive calcium channels. This wave type is supposed to underly slow contractile waves which occur during animal growth. A suggested propagation mechanism for the class of medium speed waves ($1\text{-}10\mu\text{m/s}$) as observed in vascular myocytes is calcium induced calcium entry (CICE). Calcium entry can activate other calcium sensitive ion channels that produce depolarizing currents e.g. chloride channels and thus feed back on voltage gated calcium channels. Fast calcium waves, the best known calcium waves, travel at $10\text{-}30\mu\text{m/s}$ and are the ones first observed and visualized in *medaka* eggs. They are cytosolic waves propagated by reaction diffusion mechanisms in which Ca^{2+} -ions are the only diffusing propagators and calcium induced calcium release (CICR) the only reaction. CICR is commonly described to be modulated by IP_3 or Ryanodine. The class of ultrafast calcium waves is described as subsurface or cortical Ca^{2+} -increases which accompany action potentials in neurons, muscles and other excitable systems with a velocity of $10^4 - 10^8\mu\text{m/s}$.

A new type of highly localized submembrane Ca^{2+} -wave that does not fit into the above-mentioned classifications was recently discovered in human neutrophils by Petty et al. [2]. In a later experiment, the same type of Ca^{2+} wave was observed in HT 1080 fibrosarcoma cells [15]. These waves were found to be the spatiotemporal representation of repetitive

Ca^{2+} -spikes with a period of 20s [31]. During each spike, a single Ca^{2+} -wave travels unidirectionally with a velocity of $\approx 180\mu\text{m/s}$ around the cell perimeter.

Enhanced Ca^{2+} -spike amplitude could be correlated with the formation of a pair of Ca^{2+} -waves that travel in opposite directions with the same velocity as the single wave. The trigger of this additional Ca^{2+} -waves can be stimulation by the ligand FMLP or the application of a phase matched pulsed electric field [2, 31].

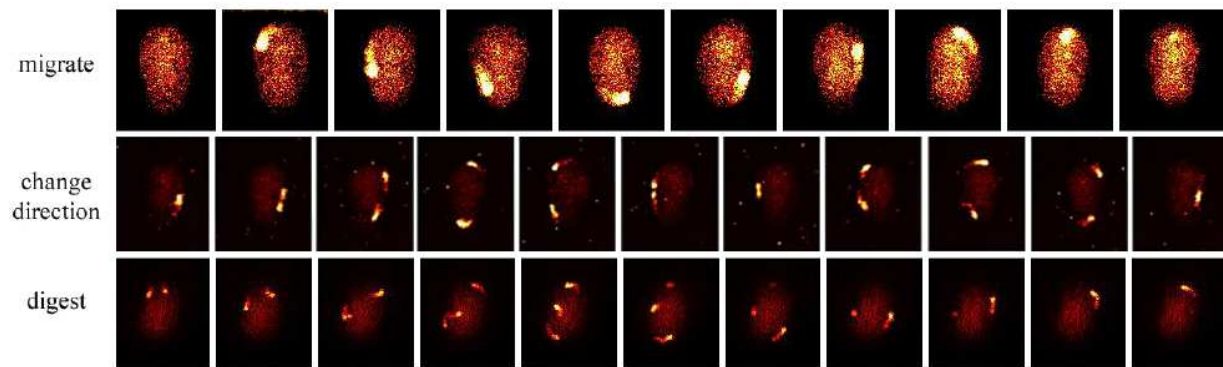


Figure 2.16: Submembrane Ca^{2+} -wave accompany migration, orientation and phagocytosis in neutrophils, [32].

Apart from migration and orientation, these Ca^{2+} -waves have been described to accompany adhesion, secretion, phagosome formation and tumor cell killing. In the third part of this thesis, a model for a plausible propagation mechanism of this wave type is developed, which is based on a local coupling of low voltage gated Ca^{2+} -channels and a Ca^{2+} -influx induced potential change.

2.10 Transmembrane ion transport and potential

The plasma membrane of a cell is a lipid bilayer which is impermeable except for small non-polar molecules. It separates intra- and extracellular space which allows the control of cytosolic ion concentrations that control biochemical reactions. To allow transmembrane ion fluxes the membrane is interspersed with proteins that are specialized for ion transport. Depending on their source of energy they are classified as pumps, cotransporters and uniporters. Ion pumps actively transport ions against concentration gradients by using ATP (therefore called ATPases). Important examples are the Ca^{2+} -ATPases responsible for restoration of low calcium levels after signaling induced calcium rise and the Na^+/K^+ -ATPase that simultaneously transports two ions to maintain their gradients. Cotransporters use electrochemical gradients of other ions, mostly Na^+ or K^+ , to transport ions against their gradients. Depending on the direction of transit they are called symporter

or antiporter. Uniporters are passive selective transporters that allow ions species to cross the membrane in direction of their electrochemical gradients. These ion channels do not allow continuous flux but can be activated (opened) by different mechanisms including mechanical stress, temperature, light, binding of signaling molecules and voltage. Specificity with respect to ion species can be explained by characteristic stiff charge patterns (carbonyl residues) lining the channel pore that have to replace the hydrate shell of the ion in solution in order to overcome the energy barrier.

The plasma membrane potential of a living cell is defined as the potential difference across the plasma membrane. Its physiological importance results from voltage dependent gating of ion channels and an electrical driving force which plays an important part in transmembrane signaling. It is commonly described as spatially uniform property, determined by concentration gradients and electrical gradients. These gradients are driving forces for selective transmembrane ion transport. More precise formulations of the uniform membrane potential are introduced in the next section. A localized transmembrane current, produces a local potential profile. A formulation of this spatial variation in membrane potential was used for the Ca^{2+} -wave model which will be introduced in chapter 5.

2.11 Models of the uniform membrane potential

2.11.1 The membrane as electrical circuit

Capacitor formulation The membrane can be described as capacitor where intra- and extracellular space are an ideal conductor and the membrane acts as a charge separating dielectric. The potential can thus be defined by

$$V = \frac{Q}{C_m}, \quad (2.8)$$

where Q includes contributions of all charged particles in a cell and C_m is the membrane capacitance. Since an ideal conductor balances charges (and induced charges) such that the potential inside the conductor is constant, the cytoplasm and the extracellular space must be electroneutral and all net charge is located on the boundary. Only a small number of ions generates the membrane potential. Problems of this approximation result from the assumption of constant extracellular ion concentrations that implicate an infinite extracellular space [33].

The differential formulation The differential formulation of membrane potential includes current induced potential changes. The potential is described by

$$\frac{dV}{dt} = \frac{\sum_k i_k}{C_m}, \quad (2.9)$$

where i_k denotes the current of ion species k . If there was no net current flux, which is commonly assumed for steady state conditions, the potential would remain constant according to Eq.2.8. By introducing implicitly defined ion concentrations and implicitly defined currents, the equivalence of the capacitor and the differential formulation was shown [33].

2.12 Nonuniform membrane potential variation produced by localized ion current

In order to model a local voltage dependent channel opening, we need a formulation of the potential profile produced by a local transmembrane current. A formulation of such a nonuniform membrane potential variation was introduced by Eisenberg and Engel in 1970 [34], where they predict a steep rise in membrane potential due to the high current density around a point like current source. The membrane potential (V_m) for a point like steady state current (i_0) in a spherical cell is described, dependent on the angular distance from the point of current entry:

$$\frac{i_0 R_m}{4 \pi a^2} + \frac{i_0 R_i}{2 \pi a} \sum_{i=1}^n \frac{n+1/2}{n+a/\Lambda} P_n(\cos(\theta)) \quad (2.10)$$

with: θ =angular distance from point of current entry

a = the cell radius [cm]

R_m = resistance of 1cm^2 of membrane [Ωcm^2]

R_i = resistance of 1cm of cytoplasm [Ωcm]

$\Lambda = R_m/R_i$ [cm]

a/λ = generalized space constant

$P_n(\cos(\theta))$ Legendre Polynomials

The first constant term in Eq. 2.10 corresponds to the spatially uniform potential while the infinite sum describes its nonuniform spatial variation. It is noteworthy that the uniform and the nonuniform potential are considered as additive quantities. Furthermore, the nonuniform potential is independent of the membrane resistance and capacity, which both determine the uniform potential. Additionally, uniform and nonuniform potential

establish on different timescales, see [34]. While the time constant of the uniform potential is commonly known as $\tau = R_m C_m$, the local potential establishes by the factor a/Λ faster. Since a/Λ is typically 10^{-5} the local potential is assumed to follow channel kinetics instantaneously.

In this formulation, the sum over all transmembrane currents is zero. An additional temporally constant propagating current, as responsible for the local potential variation, will cause a concentration shift according to $\frac{d[C_a]}{dt} = \frac{1}{zF} i_{Ca}$. Consequently, the concentration shift causes a depolarization of the uniform potential according to the capacitor formulation.

The solution introduced above is the simplified form of a more general solution by Hellerstein [35] who derived the so called *equations for the electrotonic potential*:

$$R(\sigma_{i/e}(\frac{\partial V_i}{\partial n} + \frac{\partial V_a}{\partial n}) - J_a) = \tau \frac{\partial}{\partial t}(V_e - V_i) + (V_e - V_i) \quad (2.11)$$

$$\Delta V_{i/e} = 0 \quad (2.12)$$

where $\sigma_{i/e}$ is the intra/extracellular conductivity, n the normal to the membrane, J_a the applied current through a channel and $V_{i/e}$ the intra/extracellular potential. While a detailed derivation can be found in [35], the origin of the single terms in 2.11 is illustrated in Fig.2.17.

If Eq. 2.11 is solved for a spherical cell, the solution used by Eisenberg and Engel can be obtained by evaluating at $r = a$ and assuming $\sigma_i = \sigma_e$.

The equations which have been implemented in our model are an approximation of Eq. 2.10 introduced in [34].

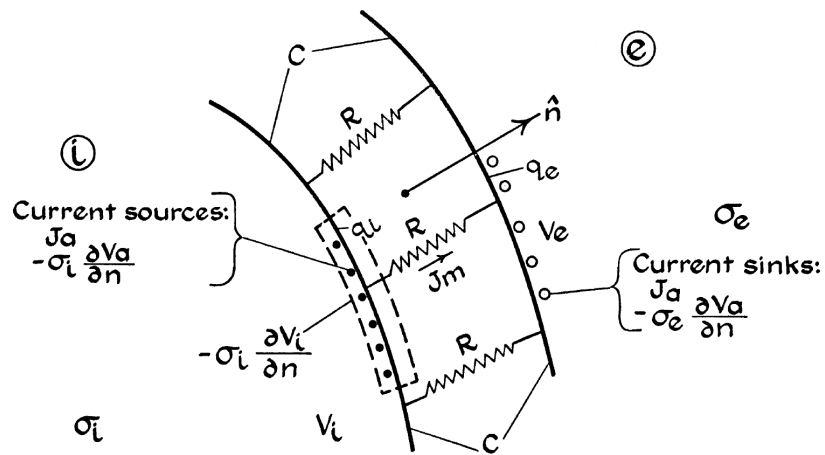


Figure 2.17: Membrane model for the fundamental electrotonic equations. The external medium, characterized by a conductivity σ_e is separated from the internal medium of conductivity σ_i by a membrane with distributed resistance times unit area (R), and capacitance per unit area (C). The surface charge density (q_i) builds up as a result of currents from the internal medium ($-\sigma_i \partial V_i / \partial n$) and currents due to applied current sources (J_a). This charge density is depleted by the transmembrane current density J_m , which builds up the charge density on the external surface (q_e), see [35].

Chapter 3

Instrumental setup and characterization

3.1 Setup

In order to collect fluorescence image series of spatiotemporal events in living cells a suitable microscopy setup had to be built up. This was realized by combining commercial modular components including an inverted wide field microscope, an EMCCD camera as detector, an incubation chamber to maintain physiological conditions and other optical or electrical accessories that are needed to control system performance.

A performance honeycomb breadboard (0.6x1.2x0.06m, *Melles Griot*) with a black low scatter surface was used and mounted on a custom made metal frame with rubber buffers made by the DKFZ workshop. In order to protect the sensitive electronics of the camera, the table was grounded by connecting it to the grounding potential of the lab with conventional grounding cables. Grounding between camera and controller card was provided by a 36-way connector and grounding of the camera was improved by conducting connections to the metal core of the optical table.

3.1.1 Microscope and illumination system

The setup was based on a commercial inverted IX70 microscope (*Olympus*). A 100W mercury lamp consisting of a U-RFL-T burner (*Olympus*) and either a USH-1030L bulb (*Ushio*) or a hbo (*Osram*) bulb served as light source for conventional fluorescence excitation. The lamp house was attached to a TIRF (Total Internal Reflection Fluorescence) illumination adapter that was purchased as prototype from Olympus, see Fig. 3.15. The lamp burner was plugged into a separate power strip in order to minimize electrical feedback with other

components that can be damaged by current surge of the HV power supply. A few simple mechanical modifications had to be made to make the adapter fit the microscope.

As typical for epi-illumination, the excitation wavelength is then selected by an optical filter and is reflected into the objective by a dichromatic mirror. Emitted fluorescence light enters the objective and is transmitted by the dichromatic mirror while backreflected excitation light is reflected back towards the excitation filter. The emission filter behind the mirror further selects the emission wavelength of interest. Fluorophore specific combinations of excitation filter, dichromatic mirror and emission filter were placed into filter cubes that were mounted in a filter wheel that allows a quick change of filter sets. The filter cubes had a built-in light trap consisting of a volume with black felt to absorb light that passes the dichroic on the illumination side. In order to prevent heat damage of the filter sets, an infrared filter was placed before the Hg lamp and the microscope. Another reason for this is the high infrared sensitivity of the chip, see Fig. 2.6. A 60x UplanApo 1.2 water immersion objective (*Olympus*) was used for most acquisitions.

In order to maximize the signal output from the side port, the prism which reflects the beam into the side port was exchanged. While the old prism reflected at least 20% of the signal into the ocular, the new prism reflects 100% signal into the side port.

3.1.2 Image splitter

For the simultaneous acquisitions of two emission wavelengths an image splitter (optosplit, *cairn*) was attached between camera and microscope via c-mount. For dual wavelength acquisition only the emission filter remains in the microscope while a dichromatic mirror in the image splitter divides the emission beam into two beams, which are then reduced by emission filters to the wavelengths of interest, see Fig. 3.1. A rectangular aperture before the first lens allows to choose the area of the chip to be illuminated. Horizontal and vertical image separation has to be adjusted and the camera has to be focused on the Optosplit aperture, as explained in the manual. Any adjustment of the optics were done in the live video mode of the camera. Image analysis of dual wavelength acquisitions can be done manually as for non split acquisitions or the software tool *field split* in Andor IQ can be used.

Single wavelength acquisitions can be done if the filter cube is removed which corresponds to a non split mode. Compared to acquisitions without image splitter the signal is only slightly reduced by two high grade AR coated lenses and two dielectrical coated mirrors, see chapter 3.2.8.

Apart from dual wavelength acquisitions, the image splitter is further useful if only parts of the whole chip are used for an acquisition e.g. in subimage readout mode or fast kinetics mode, as it prevents illumination of the chip during the shift process.

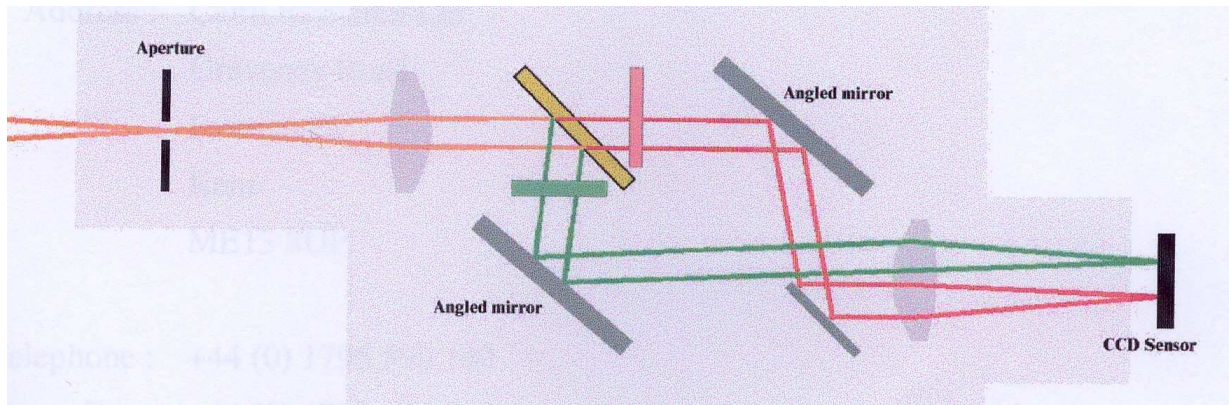


Figure 3.1: Light path in optosplit

3.1.3 Camera control and cooling

An EMCCD Camera from *Andor Technology*, type DV860 DCS-BV was used as detector. The camera was connected to the PC via a PCI (Peripheral Component Interconnect) bus interface by using a plug-in controller card in PCI format from *Andor Technology* with a 15 pin auxiliary connector. The controller card buffers data from the detector before transfer into the computer memory via the PCI bus pins as shown in Fig. 3.2. Power supply for the camera was provided by a separate 5V power connection of the controller card to the PC.

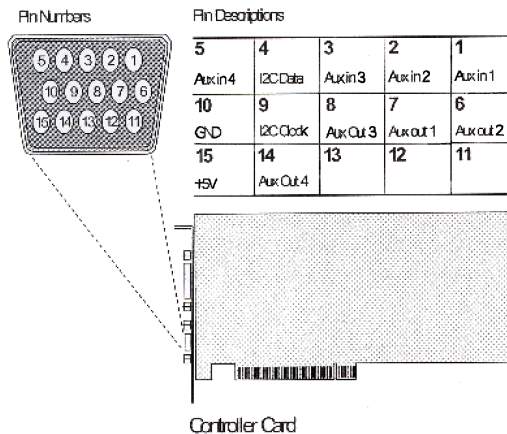


Figure 3.2: Andor PCI Controller Card provides a 15 pin auxiliary connector to control additional devices such as a trigger. Pin 11-13 are reserved for camera default control.

The EMCCD was cooled down to -90°C by a built-in Peltier cooling. As recommended by the manufacturer the power supply block for the Peltier cooling was plugged into the same power strip as the computer for best performance. A water circulator (*Haake*) which was cooled down to 13°C served as heatsink for the thermoelectric cooling. This temperature

prevented condensation in the camera head at normal humidity conditions. Unfortunately, a sudden rise in humidity up to 90% caused condensation on the cooling tube and probably in the camera head, leading to serious camera damage. Two connectors on the back allow water to be passed through the detector head but outside the hermetic vacuum sealed housing. Without water cooling, the camera could be cooled with a built-in fan which leads to a minimum temperature of -75°C .

3.1.4 Computer components

A PC with Intel Pentium 4 DualCore CPU (2,66GHz, S-775 PDP-805, 2MB cache), 512MB RAM (Dimm DDR2 PC-667) was equipped with two separate harddrives. The fast one, a HD Sata WD740AD, 74GB with 10000U/min and 4,5ms response time was used for data acquisitions. Camera operation was controlled by the software *Andor Ixon*.

3.1.5 Cell incubation during measurements

In order to keep the stage at the physiological temperature of 37°C , a stage heater was used. The immersion objective was heated to avoid heat transfer to ensure a stable temperature for the cell under observation. An objective heater further prevents variations in the refractive index of the immersion medium and convection currents in the sample due to a temperature gradient. A commercial incubation chamber constructed by *Takai Hit* was found to be the most complete and userfriendly system. It further allows to control the CO_2 concentration by a built-in flow meter. However, a 5% CO_2 /air mixture must be available which was not possible for safety reasons at the current setup location. Alternatively, a gas mixer (*Takai Hit*) could be purchased. Humidity can be controlled by a temperature controlled water bath which helps to prevent evaporation of the sample.

3.1.6 Data acquisition and analysis

Objects were placed in Lab-tek 2-well systems (*nunc*) for observation, which is a polystyrene chamber mounted on borosilicate coverglass ($0.15 \pm 0.02\text{mm}$).

Since only the most recent frames from a time series are held in the RAM, the rest of the data is read and written at high speed from the virtual memory buffer. A threshold for the data size, above which the virtual memory will be used, can be set manually. Faster and more reliable than the use of virtual memory buffer is an option called *spooling* which allows acquired data to be written directly to a storage space on the hard drive. For most acquisitions, the option *autosave* was used, which also writes data directly onto the hard drive.

Data Analysis was done with the commercial *Andor IQ* software. During analysis, data were held in the virtual memory buffer (kinetic image disk).

3.2 Camera characterization

3.2.1 Spatial resolution

The lateral resolution limit according to the Rayleigh criteria for $\lambda = 450\text{nm}$ and $\text{NA} = 1.2$ is $\approx 230\text{nm}$. The experimental calibration was done with fluorescently stained, polystyrene microspheres (*molecular probes*) which have a diameter of $2.7 \pm 0.004\mu\text{m}$. The average diameter of optimally focused beads corresponds to 8 ± 1 pixels, see Fig. 3.3. Thus, one pixel of the size $(24\mu\text{m})^2$ detects signal from $0.34 \pm 0.04\mu\text{m}^2$ of the object. According to the Nyquist Theorem that requires at least 2 pixels per length which is to be resolved, only objects larger than $\approx 0.7\mu\text{m}$ can be resolved with sufficient contrast. The calibration bar was automatically produced by the calibration assistant tool of Andor IQ.

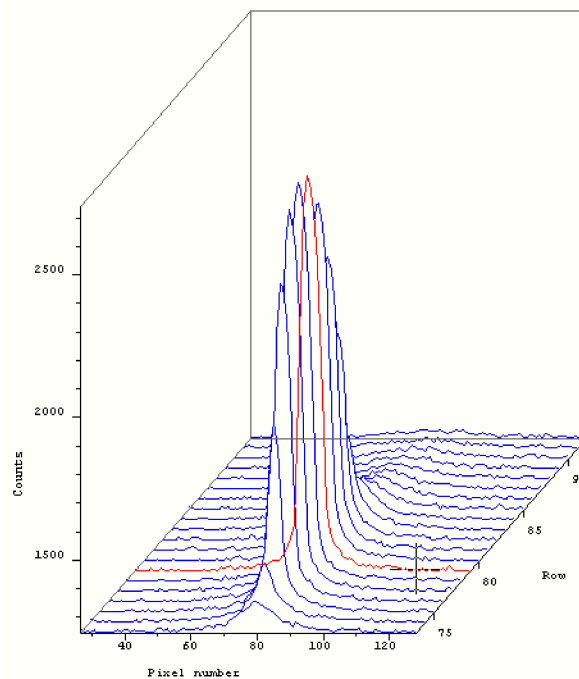


Figure 3.3: 3D-plot of the fluorescence emission of the bead which was used for calibration.

3.2.2 Temporal resolution

Temporal resolution can either be interpreted as maximum frame rate or minimum exposure time, two quantities which can be coupled or are independent from each other, depending on the camera mode. In non frame transfer mode, the minimum exposure time is $20\mu\text{s}$. In the frame transfer mode, the exposure time is inversely proportional to the frame rate. The maximum frame rates in the kinetics acquisition mode for various combinations of subimage size and binning were estimated for both camera modes, as presented in Fig. 3.4. This was done at maximum readout rate (10MHz) and the most frequently used vertical shift parameters of $0.3\mu\text{s}$ and $2V$.

| subimage size | 1 x 1 | 4 x 4 | 8 x 8 | 16 x 16 | 32 x 64 |
|---------------|-------|-------|-------|---------|---------|
| 128^2 | 480 | 1350 | 1923 | 2381 | 2630 |
| 64^2 | 847 | 2000 | 2500 | 2777 | 2940 |
| 16^2 | 2000 | 2940 | 3125 | 3333 | - |

(a) Maximum frame rate for different binning parameters (horizontal) and subimage sizes (vertical) in kinetics and *non frame transfer mode*, $T_{exp} = 20\mu\text{s}$.

| subimage size | 1 x 1 | 4 x 4 | 8 x 8 | 16 x 16 | 32 x 64 |
|---------------|-------|-------|-------|---------|---------|
| 128^2 | 500 | 1470 | 2174 | 2777 | 2940 |
| 64^2 | 909 | 2270 | 2940 | 3333 | 3333 |
| 16^2 | 2272 | 4571 | 4166 | 4166 | - |

..

(b) Maximum frame rate for different binning parameters (horizontal) and subimage sizes (vertical) in kinetics and *frame transfer mode*, $T_{exp} \sim 1/(\text{frame rate})$.

Figure 3.4

The fast kinetics mode allows the shortest exposure times, but only for single frame acquisitions. The exposure time was estimated by software to be $1\mu\text{s}$ for all possible shift speeds and $2\mu\text{s}$ in case of the slowest read out speed, even if a subimage height of 128 pixel was chosen. In order to check this experimentally, the signal of a $10\mu\text{M}$ NADH dilution acquired in fast kinetics mode with the largest possible subimage and $0.3\mu\text{s}$ as shift speed was compared to an acquisition in kinetics mode, with an exposure time of $20\mu\text{s}$. After subtraction of the dark current, the signal was 3-4 times stronger than the signal acquired with $2\mu\text{s}$ in fast kinetics mode. Thus, the exposure time in the fast kinetics mode is indeed shorter as in kinetics mode, but not as short as estimated by software.

A significant problem occurs for exposure times comparable to the shift time since charge is produced during the shift process (see Tab. 2.1 in section 2.2.4.6 for shift times). The

further the row gets shifted into the storage area, the more photo electrons can be produced and therefore destroy the image specific charge pattern. The fastest vertical shift speed is $0.1\mu s/\text{row}$ and leads to an exposure for the last row of $12.8\mu s$ which is quite large compared to an exposure time of $20\mu s$.

3.2.3 Real gain factor

The gain of the camera can be set by software in a range between 0 and 255. This value does not correspond to the real gain that can be achieved with this setting at a certain temperature but sets the voltage of the gain register. The efficiency of an electron multiplication process increases with decreasing temperature because impact ionization gets more efficient for reduced phonon scattering. Therefore the lower the temperature is the higher is the achievable effective gain. Measurements by the manufacturer were done at $T = -50^\circ C$ for different readout rates, but the temperature dependence was not displayed in the tech notes and was thus investigated in the framework of this characterization.

For measuring the real gain factor a fluorescent bead was bleached to serve as a weak constant signal. The exposure time was chosen such that it was possible to detect the signal without gain. Only a certain percentage of brightest pixels was evaluated to exclude errors due to motions of the bead relative to the evaluated chip area (ROI, region of interest). The background was taken for each gain setting, immediately before signal acquisition, and subtracted. The real gain factor at software gain x for each temperature was then calculated by

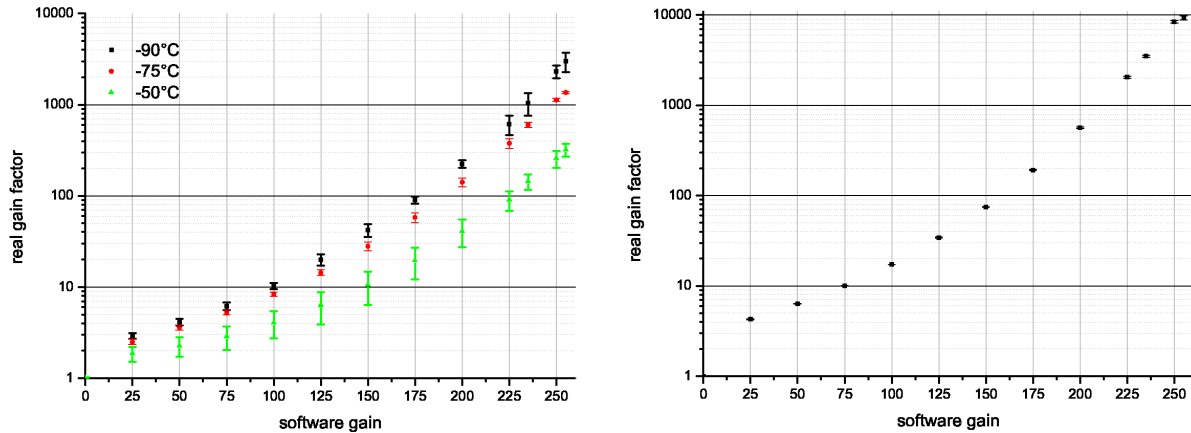
$$\text{real gain factor}(\text{gain}=x) = \frac{\text{signal}(\text{gain}=x)}{\text{signal}(\text{gain}=0)}. \quad (3.1)$$

If the image was saturated, the exposure time was reduced and the signal was extrapolated to the exposure time of the measurement at zero gain. The results were not corrected for photobleaching and are thus an underestimation.

In Fig. 3.5, the real gain factor is plotted against the software gain for 10MHz and 1MHz readout rate. The mean of 3 measurements under identical conditions (pre-gain = 4.9x, vertical shift speed= $0.3\mu s$ plus 2V) is shown. The error bars represent the standard deviation plus an error of 2% for the error of a single measurement.

At 10MHz readout rate the influence of the chip temperature was investigated, see Fig. 3.5(a). The graphs show how the impact ionization rate rises with increasing software gain (EM voltage) and decreasing temperature. Measurements at $T = -90^\circ C$ temporarily showed extreme deviations probably due to experimental errors. 5 out of 7 measurements were in the same range and the mean value is plotted in Fig. 3.5

The effect of the readout rate can be seen by comparison with Fig. 3.5(b), where the real gain factor is measured at 1MHz and $T = -90^\circ C$, the chip temperature which was used



(a) Real gain factor at 10MHz at different temperatures

(b) Real gain factor at 1MHz, $T = -90^\circ\text{C}$

Figure 3.5

for most measurements. In agreement with the tech notes, the real gain factor at 1MHz is about two times larger than at 10MHz.

Temporal stability of the gain could not be checked since it was indistinguishable from lamp fluctuations.

3.2.4 Blemishes

Different circular blemishes occurred for the fastest vertical shift speeds dependent on the shift voltage. The use of a gain did not effect the shape of the blemishes. The following images (see Fig. 3.6) are taken without gain, with open shutter, 10MHz readout rate. They show a dilution of unfocused beads in brightfield mode.

3.2.5 Readout noise

3.2.5.1 Temporal variation

Signal values acquired in the single shot mode were found to be always significantly lower than those acquired in the video mode. In order to analyze the time or frame number dependence of this effect, timeseries with different inter frame times and exposure times were measured. The acquisitions are done with closed shutter, pre-gain = 4.9, readout rates of 1MHz and 10MHz. Short exposure times and minimum temperature were used to exclude dark current contributions.

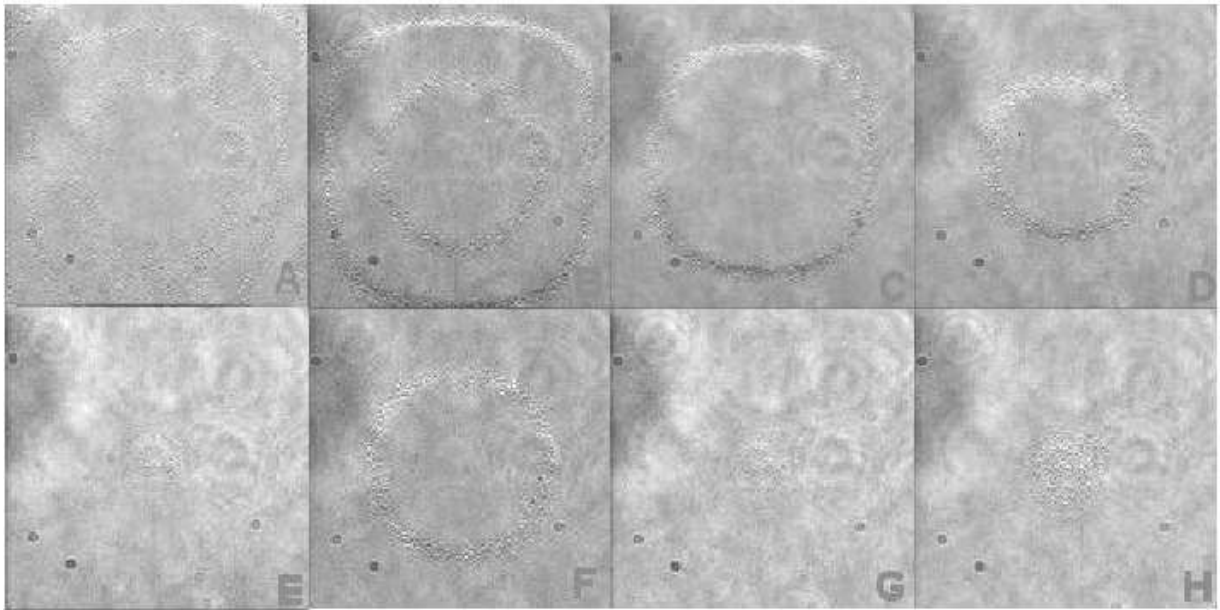


Figure 3.6: Blemishes at fast readout speeds, depending on the shift voltage: A) $0.1\mu\text{s}$ 0V; B) $0.1\mu\text{s}$ 1V; C) $0.1\mu\text{s}$, 2V; D) $0.1\mu\text{s}$, 3V; E) $0.1\mu\text{s}$, 4V; F) $0.2\mu\text{s}$, 0V; G) $0.2\mu\text{s}$, 1V; H) $0.3\mu\text{s}$, 0V

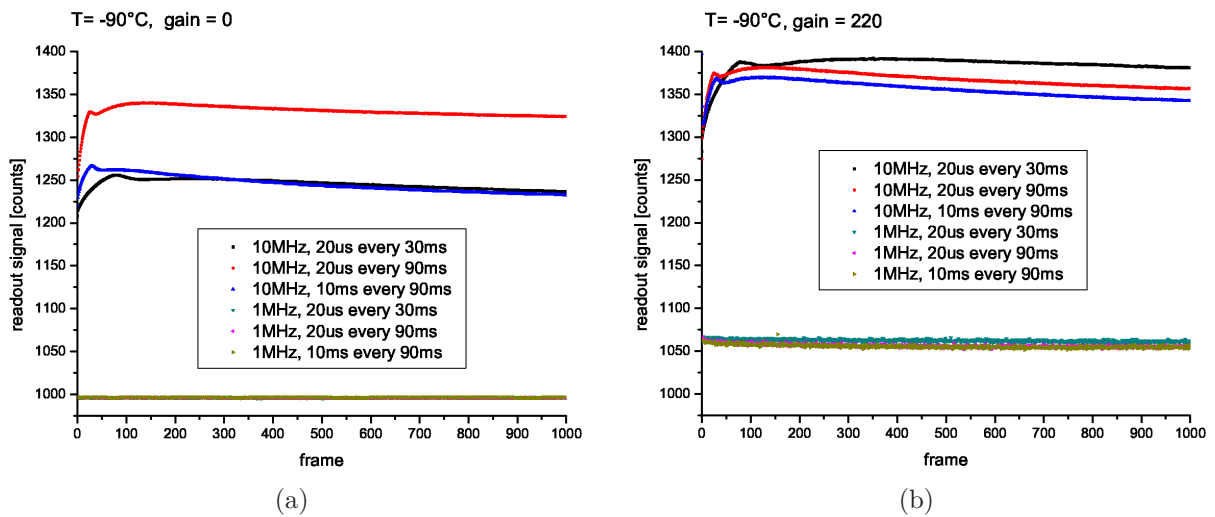


Figure 3.7: Temporal variation of readout noise: a) without gain, b) with a gain of 220.

As clearly shown in Fig. 3.7, the time dependence only occurs for 10MHz readout speed. The steep rise during the first frames seems to depend on the frame rate. A high EM gain does not change the qualitative behavior but slightly increases the absolute values. Since

the EM gain is supposed to decrease the contribution of readout noise, the effect likely results from a time dependent clock induced charge production in the readout register.

According to the manufacturer, the option *baseline clamp* in the acquisition settings was introduced to get rid of this problem. The readout noise values are taken from masked pixels and the signal is then corrected by software.

3.2.5.2 Spatial variation

To further analyze nonuniformity of the readout noise, it was separately analyzed for different vertical and horizontal rows of the chip, see Fig. 3.8(b). This was done by choosing appropriate regions of interest in the data analysis mode of *IQ*. As presented in Fig. 3.8(a), the readout noise varies over time and position on the CCD chip. The effect depends on the acquisition parameters and decreases with vertical shift speed and readout speed, thus indicating that clock induced charge production plays a role.

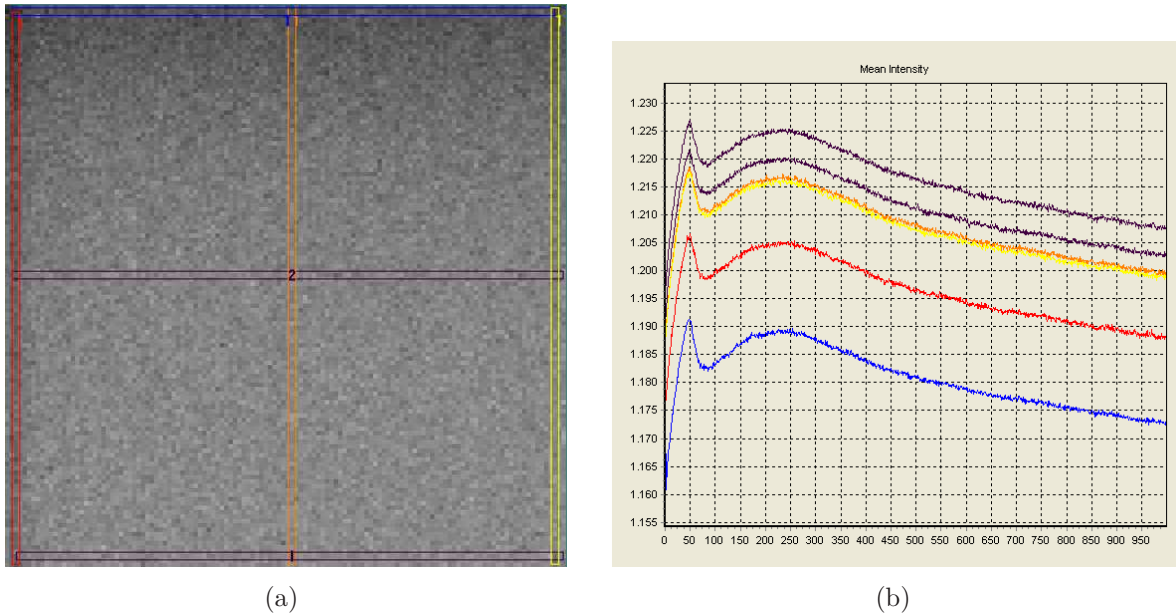


Figure 3.8: Inhomogeneous readout noise at readout speed of 10MHz, a shift speed of $0.1\mu\text{s}$ plus 0V, $T_{exp} = 20\mu\text{s}$: a) ROIs on CCD chip over which the signal is averaged; b) Timeseries of readout noise for different ROIs which are shown in the left image. The raw data, averaged over the ROI is plotted against the frame number.

3.2.6 Spurious charge

As described in section 2.2.4.2, the generation of spurious charge or clock induced charge is expected to increase with decreasing temperatures, for the same reason as the real gain increases. For a fixed temperature, it is expected to increase with increasing shift or clocking voltage and to increase with decreasing shift speed, see section basics for explanations.

The vertical CIC signal for different vertical shift speeds and voltages was measured at $T = -90^\circ\text{C}$, as mean over all pixels with closed shutter, pre-gain = 4.9, no EM gain, 10MHz and 1MHz readout rate with an T_{exp} of 1ms. The contribution of the readout noise can only be excluded at the slow readout rate. The result is presented in Fig. 3.9 (error bars are not shown for clarity).

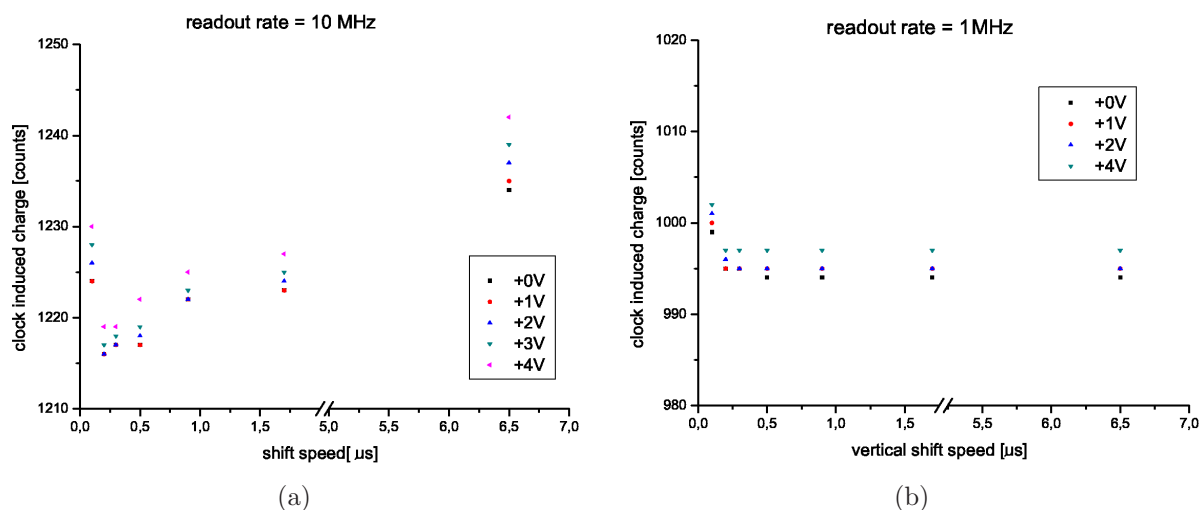


Figure 3.9: Clock induced charge: a) at 10MHz and b) at 1MHz.

The graphs nicely show a signal increase with increasing shift voltage, for both readout speeds. The difference in absolute values of Fig. 3.9(a) and Fig. 3.9(b) can be due to higher readout speed and therefore 10 fold faster horizontal clocking. At 10MHz readout rate, see Fig. 3.9(a), there is an increase with increasing shift time or decreasing shift speed, as supposed by Andor. For both readout speeds there is an increase of CIC for the minimum shift times of $0.1\mu\text{s}$. A spatiotemporal aspect of clock induced charge production has not been investigated.

3.2.7 Dark current

In order to prove if contributions of the traditional dark current are negligible at $T = -90^\circ\text{C}$, the dark signal, with closed shutter and single shot acquisition, was compared for

different but relatively short exposure times for 10MHz and 1MHz readout rate, with and without EM gain, see Fig. 3.10.

At 10MHz, an increasing exposure time had an effect on the dark current for exposure times above 30ms, while it had no effect on the signal at 1MHz. However, the increasing contribution of dark current was expected for slower readout rather than for the fast readout, since the contribution of readout time associated dark current is larger for slower readout. The dark signal increase above 30ms exposure time at 10MHz readout rate can not be explained by readout noise, since this is not supposed to contribute in single shot acquisition. This suggests a contribution of CIC, produced in the readout register. Readout noise can be noticed by higher absolute values of Fig. 3.10(a) compared to Fig. 3.10(b). Signal amplification does not change the qualitative behavior for each readout speed while the absolute value is higher if the EM gain is used. Due to the readout rate dependent gain (see section 3.2.3), the standard deviation, which depends on the stochastical multiplication process is much higher ($\approx 30\%$) for slow readout compared to fast readout.

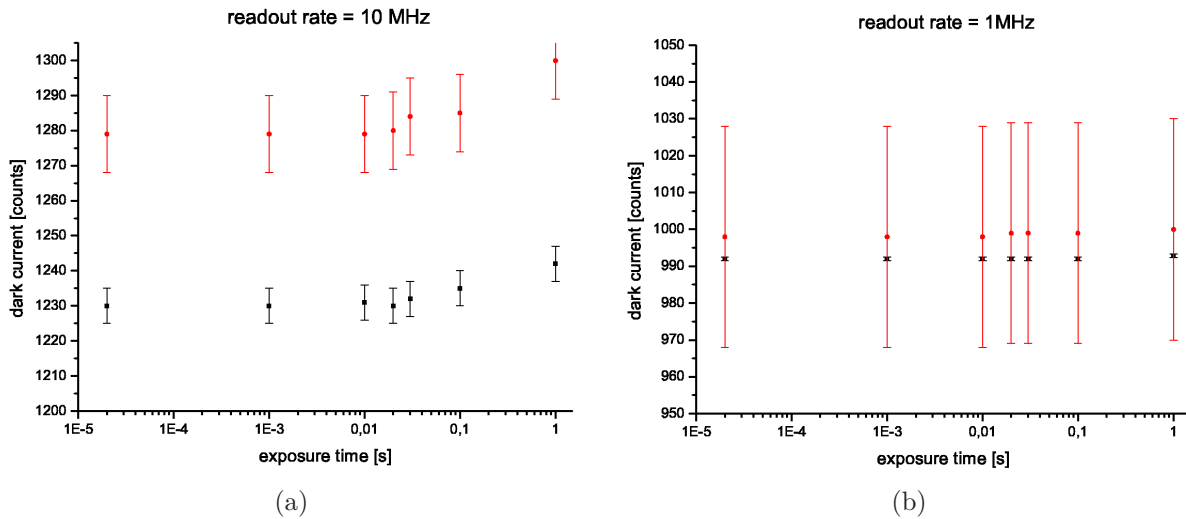


Figure 3.10: Dependence of dark current on the exposure time, using no EM gain (black) and a gain of 200 (red) at a) 10MHz and b) 1MHz. As error bars serves the standard deviation of single pixel values.

The temperature dependence of the dark current is represented in Fig. 3.11. Although the traditional dark current is supposed to decrease for decreasing temperature, it was found to increase significantly. This unexpected behavior was studied by measuring the dark current with single shot acquisitions at different gain settings at shift parameters of $0.3\mu\text{s}$ and 2V, and an exposure time of 30ms to minimize the contribution of readout noise.

The results obviously differ for slow and fast readout, see Fig. 3.11. At 10MHz, the dark signal is increasing with decreasing temperature with a slope that is maximal for the

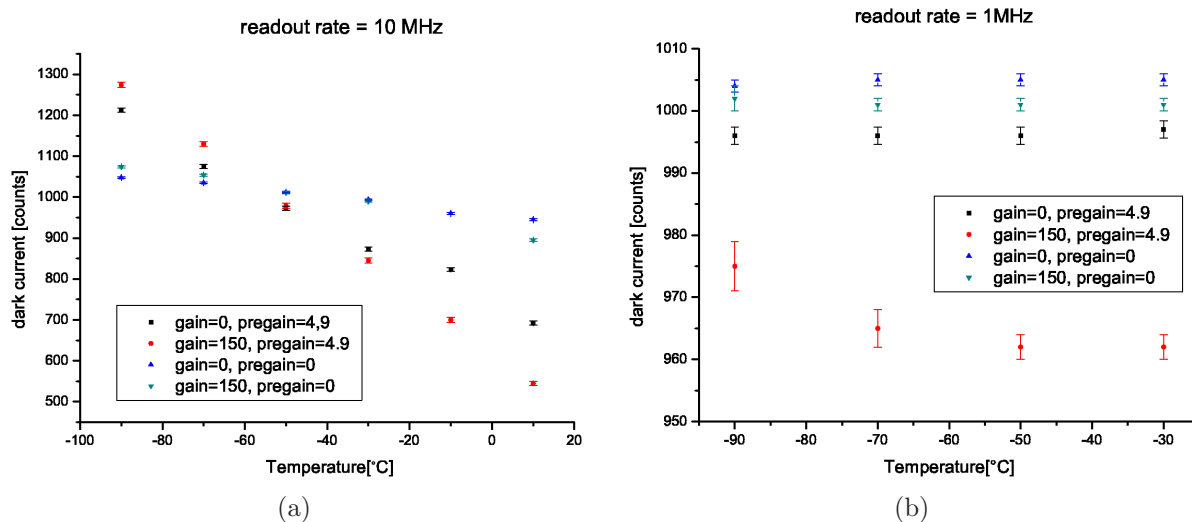


Figure 3.11: Dark current at different readout rates and gain settings

combination of high pre-gain and high EM gain and minimal for zero gain. This can only be explained by increased efficiency of charge production by horizontal, readout speed determined clocking. It might take much more than 30ms to produce as many electrons thermally, as are produced by charge shift processes at low temperatures. This indicates that horizontal CIC is the major noise contribution at fast readout speeds.

3.2.8 Detection efficiency of the Setup

3.2.8.1 Transmission properties of the setup

Petty et al. used the bottom port of the microscope in order to maximize the light collection efficiency. In order to quantify this property of our setup, all optical components those reported to be part of the Petty setup are listed in Fig. 3.12 with their transmission values. The detectors are compared according to their QE. Data of the Petty setup was estimated based on data available for similar components. A quartz objective usually has a much higher transmission below $<400\text{nm}$, which only influences the excitation efficiency of our setup. Transmission data for the quartz objective are representative for similar models (e.g. *partec*, *Zeiss*). Although using the bottom port and the fiber-coupling enables to collect the maximum possible signal, the transmissivity will be $<100\%$. Transmission data for the prism guiding the light into the side port of our setup was kindly provided by Olympus. Each glass surface was assumed to reduce the signal by 4%. The total light collection efficiency is determined by adding the respective values corresponding to the components listed above. Based on this estimation, the sensitivity of our setup should be comparable

| | | |
|---------------------------------|--------------------------|--------------------------|
| component (Petty setup) | transmission [%] | |
| objective (quartz) | 65 | |
| fiber coupling (bottom port) | <100 | |
| unknown component | <100 | |
| spectrophotometer (1 mirror, ?) | <96 | |
| QE (Gen2 tube of ICCD) | <40 | |
| total efficiency | <15 | |
| component (our setup) | transmission (405nm) [%] | transmission (450nm) [%] |
| objective (60x UplanApo 1.2 w) | 70 | 85 |
| prism (side port) | 85 | 90 |
| glass surface (side port) | 96 | 96 |
| Optosplit (2 lenses, 2 mirrors) | 85 | 85 |
| QE (EMCCD) | 40 | 75 |
| total efficiency | 20 | 47 |

Figure 3.12

to the setup used by Petty. However, if the maximum gain factor of the detectors are compared, the EMCCD used in our setup can hardly reach a real gain of 10000 (at 1MHz readout rate, maximum software gain and minimum temperature), see section 3.2.3, while this amplification factor is readily achievable by an ICCD. Furthermore, the difference is much larger for purely temporal measurements where the signal was detected with a PMT by Petty et al., since the amplification factor of a PMT can be up to 10^7 . Additionally, autofluorescence of glass components or internal reflection inside the optical components probably reduce the SNR in our setup. Differences regarding background contributions by using quartz cover slides instead of lab-tek slides could not be found in our setup.

3.2.8.2 Sensitivity required for Ca^{2+} -wave detection

In the following, the minimum local power density which is needed to obtain a Ca^{2+} -wave image is estimated, and compared to the average power density of the signal on the side port of our setup. We start with the assumption that, at exposure times of 50ns, at least 1 photons must correspond to the intensity associated with cell body. Furthermore, 2 photons must hit the phosphor screen of the intensifier tube in an area, which represents one pixel in the fluorescence image of the wave. The spatial resolution is assumed to be conserved during the intensifying process. With an emission wavelength (λ) of 405nm, the exposure time (t) of 50ns, h the Planck constant, c the speed of light and a pixel area (A)

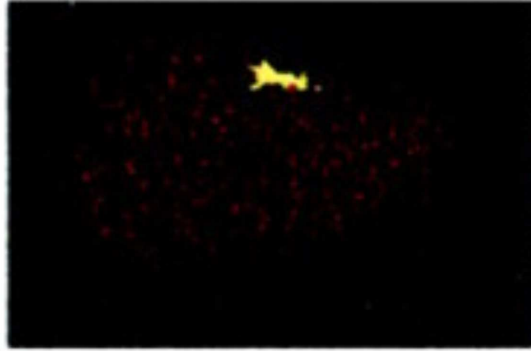


Figure 3.13: Fluorescence image of submembrane calcium wave in migrating neutrophils. The image has been taken at an exposure time of 50ns. In order to estimate the minimum power density, the red pixels of the background are assumed to represent at least 1 photon, while the yellow pixels are assumed to represent at least 2 photons. [2]

of $500\mu m^2$ as for our detector, the minimum power per pixel (P_{min}/A) is:

$$\frac{P_{min}}{A} = \frac{hc}{\lambda t A} = \frac{6,6 * 10^{-34} kg m^2/s}{4 * 10^{-7} m} \frac{3 * 10^8 m/s}{5 * 10^{-8} s} \frac{10^{-11} W}{5 * 10^{-6} cm^2} \approx 4 \frac{\mu W}{cm^2} \quad (3.2)$$

This is a fairly high value for fluorescence emission since the excitation power density in our setup was $10 \frac{\mu W}{cm^2}$ for an undisturbing lamp intensity (1%, OD2) and $100 \frac{\mu W}{cm^2}$, for the highest lamp power successfully used for cell measurements (10%, OD1), see section 4.2.1. In order to compare this value to the power density in our setup, the signal output was measured at the sideport. The averaged emission of a dense layer of fluorescent beads (*molecular probes*) was assumed to be an upper limit for the local emission intensity of a Ca^{2+} -hot spot in a cell. The beads were excited with different lamp intensities, and the emitted power density was measured with a *Nova* powermeter, using an ophir head (PD300) with an accuracy of 10%, set to wavelength 405nm.

Using a damped lamp intensity (OD2) which was found to be most undisturbing, see section 4.2.1, the measured output signal was $2nW/cm^2$, while medium lamp power corresponds to an output of $20nW/cm^2$.

If the above-estimated minimum power density is correct, an exposure time of $5\mu s$ is required to detect a single photon with our setup. The maximum possible exposure time of $200\mu s$ would only detect approximately 40 photons. However, if the emission of the fluorescent beads is much higher than the local emission of a calcium wave, the number will decrease towards the single photon level.

An error in this estimation might result from the unknown pixel size of the camera that was used for the published images. The pixel area could be 5 times smaller as the corresponding size of our camera.

3.2.8.3 NADH sensitivity of the setup

Detection limit of NADH dilutions The magnitude of NAD(P)H oscillations has been reported to be in the range of $180 - 350\mu\text{M}$ [1]. Thus, if a setup is capable to detect changes of $10\mu\text{M}$, one can safely assume that oscillations can be detected. The ability to detect NAD(P)H-oscillations at exposure times smaller 10ms can be regarded as lower limit for the ability to detect waves, since the local concentration of a wave would be higher as the averaged intensity of an oscillation.

The NADH sensitivity of the setup was investigated with a dilution series of NADH in HBSS (the NADH was kindly provided by Prof. Olsen, University of South Denmark, Odense) and compared to the NADH sensitivity of a similar Leika setup with an EBCCD camera (*Hamamatsu*, C7190), which has been used to measure NAD(P)H oscillations in single yeast cells, and a PMT which has been mounted at the camera port of the Leika microscope. In order to make measurements with different systems comparable, a SNR was defined by

$$SNR = \frac{S - Bg}{Bg}, \quad (3.3)$$

where S is the signal in counts and Bg is the signal of the buffer HBSS.

| | 10uM | 1uM | 100nM | HBSS |
|---------------------------------|--------------|-------------|-------------|----------|
| EMCCD (Signal in counts) | 123750 | 6600 | 3300 | 3070 |
| SNR | 39,31 | 1,15 | 0,07 | 0 |
| EBCCD (Signal in counts) | 190,1 | 21,1 | 17,5 | 16,5 |
| SNR | 10,52 | 0,28 | 0,06 | 0 |
| PMT (Signal in counts) | 5,70E-09 | 1,40E-09 | 8,00E-10 | 7,00E-10 |
| SNR | 7,14 | 1 | 0,14 | 0 |

Figure 3.14: The signal of NADH dilutions was measured with different setups and compared by the SNR as defined in Eq. 3.3. All systems were able to distinguish 100nM NADH from the background.

The results are shown in Fig. 3.14 and correspond to the mean of 10 acquisitions in a row. All measurements have been done with full lamp power and the most sensitive settings in lab-tek. All systems are able to detect concentrations of 100nM, while the signal of 10nM did not significantly differ from the buffer value in all systems. Absolute values of SNR can not be compared quantitatively since different exposure times were used for the EMCCD measurement and the age of the sample differed slightly. Even though an exposure time of 0.1ms is used for acquisitions with the EMCCD compared to 500ms for EBCCD and PMT, the EMCCD outperforms the other detectors. The detection limit of the EMCCD at higher exposure times was not investigated.

Ability to detect NAD(P)H concentrations in a cell In order to compare this to the ability to detect NADH concentrations in a living cell which only emits in a small volume of the buffer, nontrivial calculations must be performed.

If the signal from the whole buffer volume is assumed to contribute, regardless of the depth of focus ($0.2\mu\text{m}$), a correction factor that describes the ratio of the height of the buffer (2mm) and the height of a cell ($10\mu\text{m}$) is required. Taking an additional factor of 200 into account, this corresponds to an intracellular concentration of $20\mu\text{M}$, which would still be detectable. If this estimation is correct this implicates that oscillations with an amplitude of $\approx 85\mu\text{M}$ can be detected under ideally stable and noiseless conditions. Measurements with a fresh NADH sample at exposure times of 500ms shall be repeated in order to explore the detection limit below 100nM.

The fact that NAD(P)H oscillation in single yeast cells have been measured with the EBCCD [36] further suggests that the sensitivity is in the right order of magnitude.

3.3 Conclusion

Based on the aspects discussed, a few recommendations regarding camera handling can be made.

If a fast readout is not indicated by a high frame rate, choosing the slowest readout rate seems to reduce most exotic effects that were described for a readout rate of 10MHz. The time dependence of the readout noise was absent and the dark current was found to be independent of the exposure time as expected at $T = -90^\circ\text{C}$ for exposure times $< 1\text{s}$. Even at inter frame times of 30ms with exposure times of about 1ms, it is sufficient to choose 1MHz as readout rate since there will still be enough time left for keep clean cycle, exposure time and shift process.

For acquisitions with an exposure time $< 10\text{ms}$, for which contributions of dark current are negligible, the temperature should only be chosen as low as indicated by the required real factor to reduce the effectiveness of clock induced charge production. However, for longer exposure times implicating a slower readout, cooling down to $T = -90^\circ\text{C}$ helps to reduce dark current contributions. If the water cooling is used, the humidity must be checked continuously since the aircondition of the lab does not protect against sudden rises in humidity which indeed happened and caused camera damage.

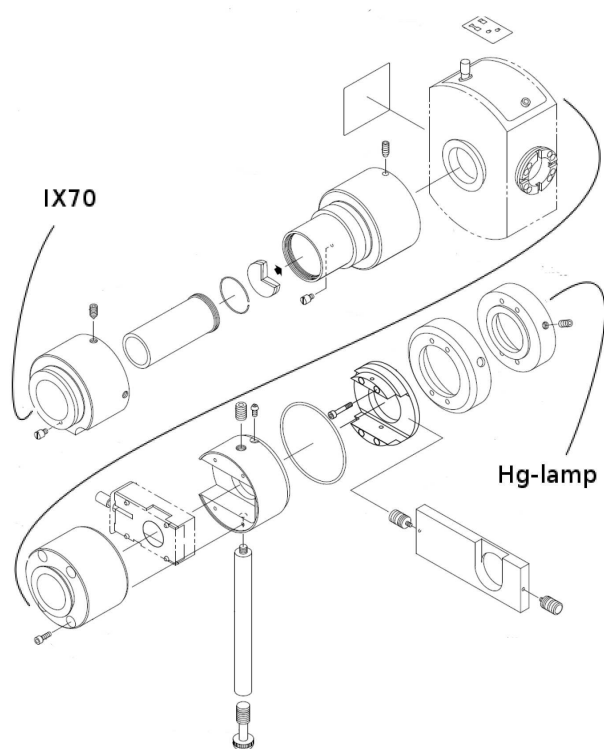


Figure 3.15: Components of TIRF illuminator

Chapter 4

Live cell measurements

Experiments were carried out with the already described setup at the *DKFZ* and with a similar setup at the Nikon Imaging Center (Bioquant, Heidelberg). Experiments done with the Celcom group (University of Southern Denmark, Odense) could not be used for analysis due to technical and biological errors.

4.1 Materials and methods

4.1.1 Cell preparation and handling

4.1.1.1 Neutrophil Isolation

Neutrophils are very sensitive cells and the technique by which they are isolated from blood samples possibly influences experimental results. The two basic procedures which are commonly used for neutrophil isolation are density gradient centrifugation and lysis. These techniques can be applied exclusively or in combination.

Hypotonic lysis Neutrophils isolated by hypotonic lysis were provided by Prof. Hänsch (Institute for Applied Immunology in Heidelberg) for first experiments. The addition of 0.2% NaCl for 20s ruptures erythrocytes via osmosis followed by the addition of 1.6% NaCl, which neutralizes the buffer to a physiological salt concentration of 0.9% NaCl. This is supposed to be harmless to leukocytes as it is a routine step for removing contaminating erythrocytes from leukocytes, which are isolated following a ficoll protocol, see below. The ruptured erythrocytes are then separated from remaining cells by centrifugation (5min at 2000rpm). Lysis has to be repeated six to seven times until most erythrocytes are removed. The sample still contains mononuclear cells, which is not a problem for microscope based single cell measurements since cells can be identified by size and morphology.

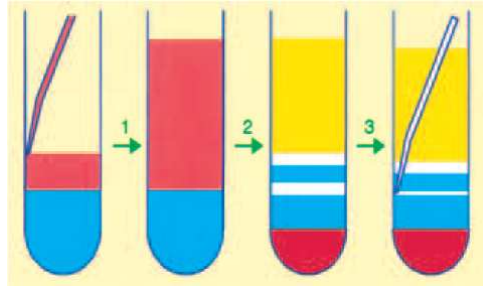


Figure 4.1: Illustration of PMN isolation following the (*Polymorphprep*) protocol.

Density gradient centrifugation In density gradient centrifugation techniques, the blood cells are separated according to their buoyant density, which is much greater for PNSs than for mononuclear cells, but similar to the buoyant density of erythrocytes. Therefore a one-step isolation of neutrophils using a dextran gradient alone is not possible.

For most experiments, isolation of neutrophils was done by using a dextran (polysaccharide) density gradient product called *Polymorphprep* (*Axis-Shield*, Norway) which allows a one-step centrifugation protocol for the separation of mononuclear and polymorphonuclear leukocytes into two distinct bands, free from red blood cells, see Fig. 4.1. The high osmolarity of *Polymorphprep* (460osm) which results from the addition of sodium diatrizoate, causes the erythrocytes to loose water and shrink, what increases their buoyant densities and thus increases their sedimentation rate. For most experiments, about 10ml of peripheral human blood was sampled by the medical assistant of the *DKFZ*, and mixed with 50 μ l of sodium heparin (*Braun*) to prevent coagulation.

Following the protocol of the manufacturer, 5ml of anticoagulated whole blood was carefully layered over 5ml of *Polymorphprep* in a 10ml tube (*falcon*), followed by centrifugation at room temperature (35min at 460 x G or 1500rpm plus 20 minutes needed for the swing out without brakes). The polymorphonuclear cells were then harvested using a Pasteur pipette and resuspended in HBSS (Hanks Balanced Salt Solution, without phenol red, with Ca^{2+} and Mg^{2+} , 1g/l glucose (5.5mM), buffered to a pH of 7.4 with Tris (24mM)). A higher glucose concentration, as used by Prof. Hänsch (11mM) was described to reduce the percentage of polarized cells [16]. The cells were washed twice by further centrifugation and resuspension (460 x G, 5 minutes). During the washing process the cell pellet was solved and resuspended in fresh buffer without using a vortex.

This isolation method was chosen since Hänsch et al. reported (personal communication) that cells isolated with *Polymorphprep* migrated well, while isolation with Ficoll, a different type of polysaccharide, lead to refractive, non migrating cells. In order to compare the migration behavior of cells isolated with *Polymorphprep* to cells isolated with Ficoll, polarized neutrophils were observed in a chemotaxis chamber (*ibidi*). However, the cells did not migrate and were refractive to stimulation for both isolation methods. This exper-

iment was not representative for several reasons, including a technical problem with the chemotaxis chamber reported by the manufacturer.

For the experiment with the ficoll gradient, 5ml whole blood was layered over 5ml Ficoll (Fico Lite-H, 1.077g/ml, *Linaris*) followed by centrifugation at room temperature (25 minutes at 2500 rpm plus 20 minutes swing out time). This separates mononuclear cells from polymorphonuclear cells, but leukocytes were still not separated from erythrocytes, which was done by lysis, repeated four times. The difference to the procedure used by Petty et al. is that separation from erythrocytes is done by subsequent dextran sedimentation, followed by lysis once only. For the separation of neutrophils from erythrocytes, Petty combines two gradients with different densities (Histopaque 1077 and 1119).

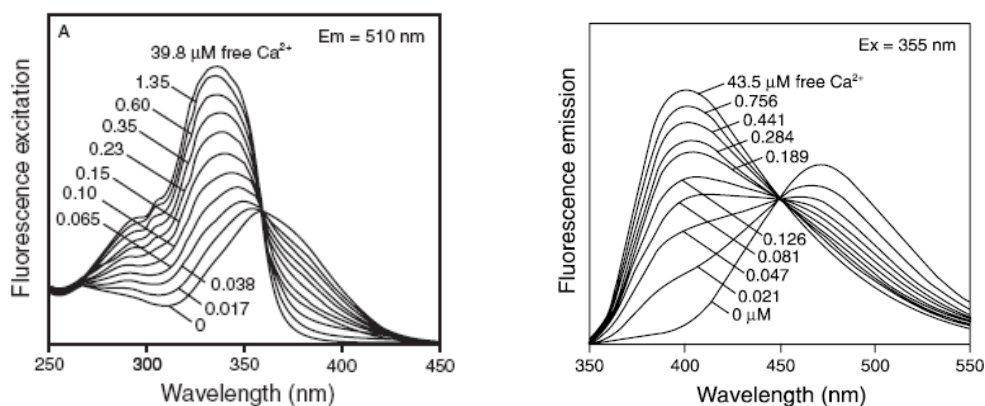
For the experiments presented here, contaminating erythrocytes were not removed by lysis and centrifugation. Alternatively, the sample was washed by changing the buffer on the microscopy slide after a suitable number of neutrophils has become adherent. Since other blood cell types remain in suspension, this technique allowed to control both, the cell density and purity on the slide.

4.1.1.2 Cultivation of HT1080 cells

HT1080 fibrosarcoma cells were grown in culture flasks at 37°C and 5% CO₂ in DMEM (*Gibco* with 10% FCS and 1% Glutamin). They have been passaged twice a week following a standard protocol including: washing off dead cells, detaching confluent cells from flasks with Trypsin for 2 minutes) and seeding in different dilutions in DMEM (e.g. 1:20, 1:50 and 1:100). For measurements, they were grown on lab-tek 2-well chamber slides used for most cell experiments. Optimal cell density for experiments on the day of the passage was achieved, if cells were seeded at a dilution of 1:20. Approximately 3 hours after seeding a significant fraction of the cells showed the typical polarized shape.

4.1.2 NAD(P)H measurement

The intracellular concentration of NAD(P)H was measured by microfluorometry, using the setup described above. In contrast to Petty et al. who used a PMT as detector, we analyzed the mean signal of all pixels of interest using the EMCCD camera. The autofluorescence of NAD(P)H was excited at 365nm (filter:365WB50, *omega optical*) and emission was detected at 450nm (filter:450AF58, *omega optical*), separated with a bandpass (400DCLP, *omega optical*). Comparable measurements were done in the Nikon Imaging Center with a similar setup, see section 4.1.5.2 for details.



(a) Excitation spectrum of fura-2 [38]

(b) Emission spectra of indo-1 [38]

Figure 4.2

4.1.3 Calcium measurements

4.1.3.1 The calcium sensitive dyes fura-2 and indo-1

Indo-1 is the calcium indicator that Petty et al. used for the detection of Ca^{2+} -spikes and waves. As shown in Fig. 4.2(b), the emission intensity of the calcium bound dye changes in a wavelength dependent manner. At 405nm, the intensity increases dramatically for calcium concentrations that are commonly associated with cell activation, while the emission at 470nm drops slightly. The calcium sensitivity of fura-2 arises from wavelength dependent excitation of the calcium bound dye. Both spectra have an isobestic point, which is insensitive to changes in calcium concentration. This can be used for calibration. The binding kinetics of the dyes differ slightly, determining the ability to measure fast concentration changes. Indo-1 has an association constant of $0.5 - 1.0 \cdot \text{nM}^{-1}\text{s}^{-1}$ which is about twice as high as the corresponding value of fura-2 [37], making it more suitable for the detection of fast concentration changes. Dissociation constants (K_d) are 140nM and 230nM for fura-2 and indo-1 respectively [38], indicating a lower affinity and thus faster off-rates of indo-1. For measurements with our setup, a 355HT15 filter was used for excitation while the emission was detected with a 405DF43 filter and separated with a 390DRLP bandpass.

4.1.3.2 Labeling protocol

Indo-1 AM and fura-2 AM were purchased from *Sigma Aldrich*, solved in DMSO and the stock solutions (1mM) were stored at -20°C . The AM (acetoxymethylester) form of the

dyes can passively diffuse across the cell membrane. For cell labeling, $5\mu\text{l}$ of the stock solution was diluted in 1ml HBSS, leading to a final concentration of $5\mu\text{M}$. Incubation was done at 37°C in the dark, 20 min for indo-1 and 30 min for fura-2, followed by 2 times washing with HBSS. The centrifugation for the washing process was done at 2000rpm for 5 min and the pellet was solved in fresh buffer without using a vortex. Measurements were done after ≈ 20 minutes of equilibration, which is also needed for cytoplasmic de-esterification into the membrane impermeable forms of the dyes. The AM ester forms are also fluorescent, but calcium insensitive.

4.1.3.3 Ratio imaging

Ratio imaging with fura-2 was performed at the Nikon Imaging Center. Two different excitation wavelengths (340nm and 387nm) were used. Filter sets were changed automatically. An intracellular rise in calcium concentration causes the excitation efficiency at 340nm to increase, while it decreases at 387nm, see Fig. 4.2(a). Thus, by taking the ratio of the emission intensities, the calcium sensitivity of the signal is increased. Furthermore, artifacts produced by lamp fluctuations or shape changes, which would modulate excitation or emission equally for both excitation wavelengths, are eliminated by taking the ratio.

4.1.4 Shape measurements

Dynamic measurements of shape changes have been done in previous studies by using 90° -light scattering or turbidity measurements. Periodic signal changes have been found, see [12] for references. In order to relate the signal obtained from a bulk measurement to collective shape changes, theoretical descriptions of how volume changes, lamellipod and pseudopod extension influence the signal are needed. This has not been done yet. However, it has been suggested that low light extinction coincides with a polarized morphology. If shape changes are measured based on a cytoplasmic fluorescence signal, two different cases have to be considered. A symmetric increase in cell volume and the formation of asymmetric extensions at a constant cell volume.

The fluorescence signal (F), averaged over the projected cell area (A), is proportional to the concentration of the fluorophores (c) and the average cell diameter along the light path (d):

$$F \sim c * d. \quad (4.1)$$

- For the case of symmetric cell swelling, the signal will decrease with increasing area (A) since the cell diameter increases with the radius (r) but the fluorophore concentration decreases $\sim r^3$.

- Asymmetric extensions at a constant cell volume reduce the average cell diameter and thus the signal.

Thus, one expects the average fluorescence to be inversely proportional to the projected cell area in both cases. An important question is how the depth of focus influences the signal distribution over the whole chip.

The depth of focus can be described by

$$\Delta X \approx \frac{2n\epsilon}{M}, \quad (4.2)$$

where ΔX is the distance from the focal plane, n the relative aperture, ϵ the radius of lateral uncertainty allowed for a certain pixel size and M is the magnification of the objective, see [39], p. 210. For a typical microscope, the depth of focus is $\approx 200\text{nm}$ which is much smaller than the diameter of a spherical neutrophil of $\approx 10\mu\text{m}$. Assuming the thin lamellipod extensions of a cell are roughly within the depth of focus, the major fraction of the cell body will definitely be out of the depth of focus. If the cell contracts, the distance of the cell body to the focal plane increases further.

Since the total photon flux of excitation and emission in other planes are expected to be the same in widefield microscopy, the signal should be roughly constant when averaged over the whole CCD chip. However the contrast, which is crucial for image analysis will decrease.

A conclusion whether cell body contraction leads to a signal decrease or not depends very much on the area over which the intensity is averaged as well as on the cell volume change. Thus, no clear interpretation of the data is possible without further investigations.

4.1.4.1 Detection method

The cells were isolated following the Polymorphprep protocol and observed in HBSS buffered to a pH of 7.4 with Tris (24mM). The lamp power was reduced with gray filters (OD2), as described in section 4.2.1. No stimulation was applied but activation due to nonsterile preparation can not be excluded. The cells were labeled with indo-1 as for calcium measurements, but the emission was detected at 450nm with the NADH filter set, which is an isobestic point of the indo-1 emission spectrum (calcium insensitive emission), see Fig. 4.2(b). Due to the bandwidth of the NADH emission filter, detection of calcium sensitive parts of the spectrum could not be excluded. If the intracellular calcium concentration was depleted by the addition of ionomycin (*Sigma-Aldrich*) to a final concentration of $20\mu\text{M}$, no significant change in intensity was observed. However, no increase in intensity at 405nm was observed either, indicating a problem with the dye. An additional proof for

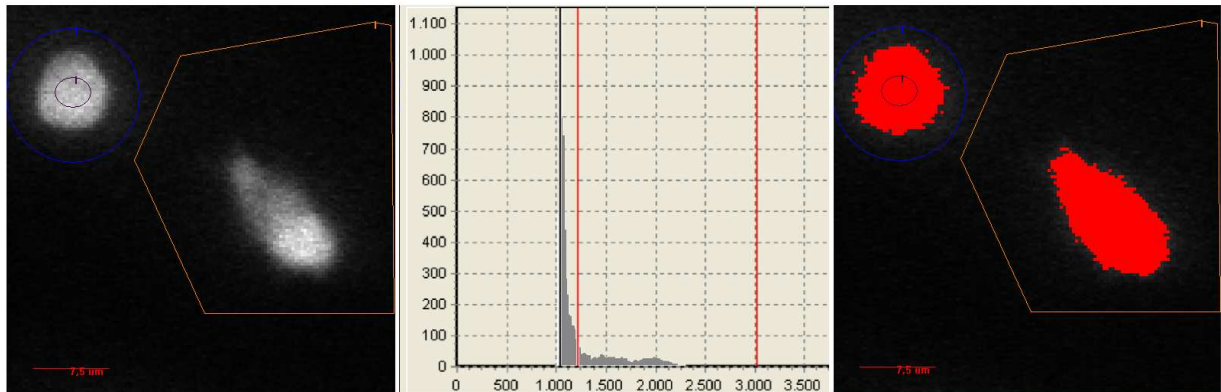


Figure 4.3: The fluorescence signal of a spherical non migrating and a polarized migrating cell was analyzed simultaneously (left). By setting a threshold such that only the pixels corresponding to the cell area were analyzed, the projection of the cell body can be observed (right). The left red bar in the histogram (middle) shows the position of the threshold in the histogram, which is critical for the reliability of this method.

the Ca^{2+} -insensitivity of the fluorescence signal is the signal shape. The signal measured at 405nm has the same peak-like minima as the signal measured at 450nm, see section 4.2.5.3.

The intensity of indo-1 labeled cells was ≈ 25 times higher than the NADH autofluorescence when the applied exposure time and the SNR (signal to noise ratio) were compared. The signal obtained at $T_{\text{exp}}=0,5\text{s}$ for NAD(P)H lead to a SNR of $\approx 0,1$ while the SNR of the labeled cells obtained at $T_{\text{exp}}=0,01\text{s}$ was $\approx 0,05$. It can therefore be excluded that the signal oscillations observed in labeled cells result from NAD(P)H-oscillations.

4.1.4.2 Data analysis

As always done when analyzing a weak signal of a fast migrating cell, setting a threshold at a high contrast timeseries allowed to determine the projected area of the cell by counting the pixels above the intensity threshold. The threshold was set such that the perimeter of the resulting cell area corresponded to the cell perimeter determined by eye inspection. The histogram of a typical high contrast acquisition with a bar representing the threshold is shown in Fig. 4.3.

4.1.5 Data acquisition

In order to obtain physiological conditions during the measurements, the *Tokai Hit* incubation chamber described in chapter 1 was used. Cells were mostly placed on Lab-tek

2-well systems (*nunc*) for observation. If quartz slides were used, no obvious difference in cell behavior could be observed. After adjusting the cell density such that observation of single cells was possible, cells were chosen individually for measurements after observation under brightfield illumination if they showed the required morphology and behavior. For fluorescence measurements, the field aperture was adjusted such that only the field of view on the detector was illuminated to minimize irradiation of neighboring cells. Furthermore, the aperture of the *optosplit* was closed to an extent that only emissions from the area of interest, namely the field of view of the camera could enter the image splitter.

4.1.5.1 EMCCD settings

The EMCCD acquisition settings that were used unless otherwise noted correspond to a vertical shift speed and voltage of $0.3\mu\text{s}$ and 2V , 1MHz readout rate and a chip temperature of -90°C . Timeseries were taken in the kinetics mode, without baseline clamp and in non frame transfer mode. Since weak signals were measured, the pre-gain was set to 4.9x .

Exposure time and cycle time (inter frame time) were chosen by software. The subimage mode was never chosen since the image of a neutrophil already covered about half of the chip. Binning ($2\text{x}2$) was only used if emphasized.

4.1.5.2 Setup and settings in the Nikon Imaging Center

Additional measurements were done at the Nikon Imaging Center, with a similar setup (TE 2000-4 inverted microscope, *EXFO X-Cite 120* lamp), using a UV corrected 40x PlanApo ($\text{NA} = 1.4$), and an EMCCD camera (*Hamamatsu*, C9100-12). A lamp shutter reduced the illumination time. Binning ($2\text{x}2$) was used in most acquisitions.

4.1.6 Data analysis

Data analysis was done with *Andor IQ*. For cells that were not moving significantly, the fluorescence intensity was averaged over the ROI (region of interest). If the frame rate used was higher than necessary for the detection of oscillations, the data were smoothed using the *image math* option of *Andor IQ* to eliminate noise by adding frames, until a total time of 2s was covered by the resulting image. If cells were migrating fast, the ROI had to be chosen as large as the area transited by the cell. For low contrast images, this averaged the small signals such that oscillations could not be detected. Therefore, an intensity threshold was set manually that excluded background pixels from evaluation. This method also allowed to determine the cell area, as will be explained later. The resulting data files were exported and presented using *Origin*, otherwise data was plotted with *Andor IQ* for convenience.

Data analysis at the Nikon Imaging Center was done similarly using the software *NIS-Elements*. The image contrast was modified using the *mapping* function and a false color representation. If the intensity varied strongly over time and cell location, further image processing was done with *Andor IQ*, as described in 4.2.6.1.

4.2 Results

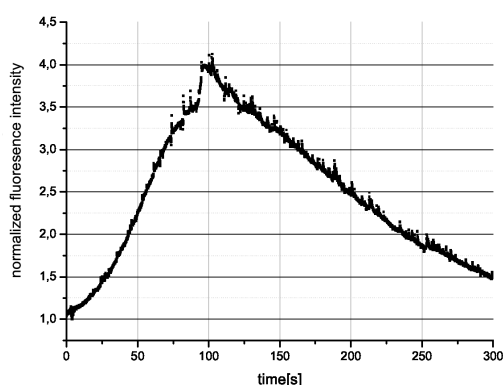
4.2.1 Effect of illumination power on cell behavior

In general, illumination power should be minimized for live cell experiments in order to prevent phototoxicity. This is especially important if UV excitation is applied. The main damage caused by UVA radiation (320 – 400nm) results from the production of reactive oxygen species such as excited singlet oxygen, superoxide anions, hydroxyl radicals and nitric oxide which can have various effects on cells. It is assumed that these effects depend on the irradiation dose which is proportional to the product of illumination power and illumination time. Thus, phototoxicity can either be minimized by using neutral density filters to attenuate the lamp power as much as the sensitivity of the setup allows, or by using a lamp shutter to prevent illumination during the inter frame time.

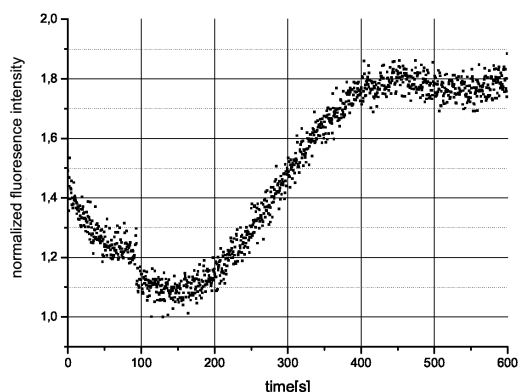
The illumination power was measured behind the objective with a powermeter (*Nova*) set to 405nm. The position of the detector head was varied and the maximum value was noted. The power density of the focussed beam was estimated by assuming that the measured value represented the power of the beam with a diameter of 1mm².

- If cells were illuminated with maximum beam intensity of $\approx 14\text{mW}/\text{cm}^2$, the NAD(P)H signal immediately increased monotonically up to 300% above the initial value, see Fig. 4.4(a). When reaching a maximum level, the signal decreased again, likely due to photobleaching. The signal increase of the cytoplasm, see Fig. 4.4(d), allowed to recognize cell organelles such as the polymorph nucleus. Another effect of this illumination power was that migrating cells stopped moving. No oscillatory signal was observed for this illumination power. When a comparable illumination power was used at the Nikon setup, where a larger field of view allowed to observe several cell simultaneously, the fraction of adherent cells increased significantly after 5min of illumination.
- Using a gray filter (OD1) which reduced the illumination power to $\approx 1\text{mW}/\text{cm}^2$, lead to photobleaching of $\approx 20\%$ per minute followed by and signal increase after about 3 minutes, see Fig. 4.4(b). Although cells were not stopped in their movement immediately, no oscillatory signal was detected at this illumination power.

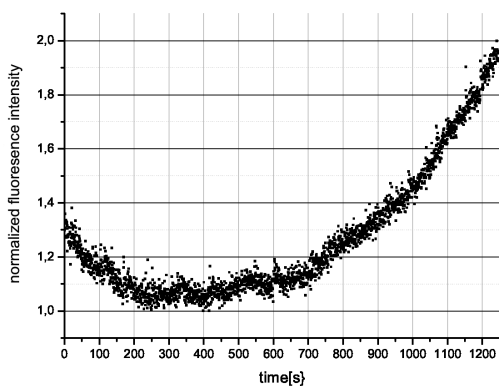
- With two gray filters (OD1), mounted between to cover slides (corresponding to OD2, $\approx 200\mu\text{W}/\text{cm}^2$) no significant signal increase occurred within 10 minutes and photobleaching was $<5\%$, see Fig. 4.4(c).



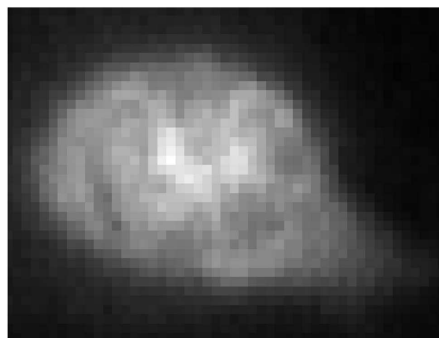
(a) Effect of UVA illumination on NAD(P)H fluorescence signal: immediate signal increase at maximum lamp power



(b) Effect of UVA illumination on NAD(P)H fluorescence signal: delayed signal increase at medium lamp power



(c) Effect of UVA illumination on NAD(P)H fluorescence signal: late signal increase at low lamp power



(d) The cytoplasmic signal increase allowed to recognize cell organelles such as the polymorph nucleus

Figure 4.4

Since the results of Petty et al. did not show any activation or bleaching effect without a shutter being used (personal communication), it can be assumed that the illumination intensity was $<1\text{mW}/\text{cm}^2$. This is important when the sensitivity of the setups is compared.

Since the excitation wavelength of the indo-1 and NAD(P)H is similar, the UVA induced effect will also be present for measurements with the indo-1 filter set, although a change

in NAD(P)H emission will not be noticeable, due to a different emission filter. If the excitation effectiveness of filters is compared by approximating the integral of the spectral transmission profiles, excitation power of the indo-1 filter set is 4 times lower than for the 365WB50 in the NAD(P)H filter set. Thus, when estimating a noninvasive lamp power, the intensity can be 4 times higher, as the values for the NAD(P)H filter set.

4.2.1.1 NAD(P)H detection limit in living neutrophils

The detection limit of NAD(P)H in neutrophils was estimated depending on lamp power and exposure time. The signal was considered to be detectable if the location of the cell body was recognizable on the fluorescence image, after optimizing the contrast in IQ . If the cell was only localizable by using a high gain (e.g. 200), the noise in the background corrected signal was often larger than the expected Amplitude of the oscillations. Since NAD(P)H levels varied slightly among cells, the detection limit does not implicate that oscillations are detectable in all cells.

- With the full lamp power $(300 \pm 100)\mu\text{W}$, which has been found to be highly disturbing, see previous section, the minimum exposure time achievable with sufficient contrast was 1ms at a gain of 100.
- Using an illumination power of $(30 \pm 10)\mu\text{W}$ that prevented a UVA triggered signal increase for 2-3 minutes, the minimum exposure time achievable, was 10ms with a gain of 200.
- With an illumination power that avoided a UVA triggered signal increase for 10 minutes $(5 \pm 1)\mu\text{W}$, it required exposure times of 500ms if a moderate gain software gain of 100 was used, and 100ms for a software gain of 200.

Since the detection of NAD(P)H-waves requires exposure times of 10ms or shorter, see section basics, this setup does not allow NAD(P)H-wave imaging with an undisturbing lamp power!

4.2.1.2 Indo-1 detection limit in living neutrophils

According to Petty et al., a minimum exposure time of $200\mu\text{s}$ is required to recognize a calcium wave. Therefore, the minimum exposure time achievable was determined for neutrophils labelled according to the protocol of Petty et al.

At steady state calcium concentrations, the fluorescence signal at medium excitation power did only allow to decrease the exposure time down to 2ms. However, the detection limit of

indo-1 depends on the calcium concentration. Due to the binary emission intensity of indo-1, see Fig.4.2(b), the local intensity of the wave is comparable to the averaged intensity of a calcium depleted cell. Since calcium depletion did not lead to the expected signal increase, the minimum exposure time achievable at elevated calcium concentrations was estimated based on the calcium dependent emission spectrum of indo-1. Since the emission intensity at 405nm increases ten times at high calcium concentrations, the estimated minimum exposure time is 200 μ s. Thus, it is theoretically possible to reach the minimum exposure time that is required for the detection of Ca²⁺-waves, under optimized labelling conditions.

4.2.2 Cell morphology and migration behavior

Since there is few literature about the variety of shapes and movements that living neutrophils can adopt, a phenomenological description of the observations which were made during experiments will be given in the following.

After transferring the cell suspension onto the slide, some neutrophils started to adhere immediately. The fraction of adherent cells increased with time, until, after 2-3 hours on the slide, they either became apoptotic in the polarized morphology or they fell back into a spherical non adherent state.

Depending on the cell isolation method, handling and age of the sample, the cells appeared to be in different viability and/or activation states. These states were not further characterized by appropriate cell biological methods. Since conditions during experiments changed, only qualitative observations are summarized.

Morphology Polarized adherent cells were found for all methods except for those cells isolated with FACS lysis buffer containing formaldehyde. Different levels of polarizations were observed, similar to those described by Hallett et al. [40].

Many adherent cells were not polarized along one distinct direction. Some cells showed small extensions in more than one direction, see Fig. 4.13. With increasing age of the sample (stored in HBSS in the dark at room temperature), the fraction of cells with this morphology increased and extensions increased in number and length, appearing like filopodia. Other cells allowed identification of a particular direction of orientation. Less cells showed a longitudinal shape with clearly defined uropod and lamellipod. These differences were observed even without any migration. Polarized cells in suspension, as described in section 2.5 were also observed.

Migration Different modes of migration were observed: In most preparations with hypotonic lysis and *Polymorphprep* the cells showed lamellipodia extensions in arbitrary directions, although the cells did only move slowly (<1 μ m/min) and often seemed to stick

to the slide. If the cells were illuminated with full lamp power, this movement was stopped and the cells shranked slightly.

If illuminated with a low lamp intensity, see section 4.2.1, cells isolated with *Polymorphprep* temporarily migrated as fast as $3\mu\text{m}/10\text{s}$. This is very fast compared to average chemotaxis speed observed by Prof. Hänsch, $100\mu\text{m}/90\text{min}$, or $3\mu\text{m}/\text{min}$ as reported by [41]. The discrepancy to our results can be explained by the nonuniformity of migration observed in our setup. The neutrophils seemed to switch between periods of fast migration and periods in which the cell appeared to adjust to a new direction. This is consistent with observations described in the review of Ehrenguber et al. [14], see section 2.5.

If stored at room temperature in the dark in HBSS, properly polarized and migrating cells were found 36 hours after cell isolation.

Chemotaxis experiments using commercial chemotaxis chambers (*ibidi*) with an FMLP gradient did not allow to observe migrating cells, although a slight excess in orientation towards the FMLP reservoir was observed. According to the manufacturer, such problems were reported by others too, and do not necessarily implicate an application error.

4.2.3 Shape oscillations

By measuring the cytoplasmic fluorescence signal of indo-1 at the isobestic point of the spectrum (450nm), oscillations with periods of 10s, 20s and 50s were observed with our setup. These signal modulations likely result from shape change induced intensity modulations. We tried to correlate the intensity oscillation to changes of the projected cell area based on an intensity threshold method as described earlier. Unfortunately, this method seems to be fairly susceptible for artifacts, and it was not possible to determine whether cell area and intensity are generally in phase or not, or if there is a fixed phase relation at all. Although oscillatory events were found in most cells observed ($n=30$), only few cells showed such a nice periodicity as the data presented here. It was assumed that these data correspond to a more physiological undisturbed behavior than the data with a tendency to chaotic appearance. Therefore, only data of individual cells are presented which allowed a correlation to the morphological state.

Oscillations of average intensity and projected cell area with a period of $\approx 10\text{s}$ were found in migrating possibly activated cells, see Fig. 4.5(a) and a period of $\approx 50\text{s}$ was found in spherical non migrating cells, see Fig. 4.5(b). For the cell presented in Fig. 4.5(a), the 10s area oscillation of the migrating cell seems to have a lower frequency oscillation superimposed.

The intensity in the center of the spherical cell was analyzed separately and presented in the same graph. The intensity oscillation in the cell center was in phase with the signal of the whole cell and showed a higher absolute value for reasons of different cell thickness (see Fig. 4.5(c)) and a slightly larger relative amplitude, see Fig. 4.5(b).

The amplitude of the intensity oscillations in the migrating cell is $\approx 7\%$ from the baseline, larger than the amplitude of the area oscillations of $< 2.5\%$. In order to investigate the relationship of the intensity and the cell area oscillation, the difference of normalized intensity and area is displayed in Fig. 4.5(d). Since the result is not constant, the relationship of the intensity and the cell area oscillation is not trivial. Unfortunately, at this point of the investigation, it is not possible to give a distinct interpretation of this graph.

In spherical adherent cells that did not show any variation of cell shape, no oscillatory signal was found (data not shown). A more precise correlation to different types of movements was not possible for several reasons. Firstly, only the signal of few cells showed a nice periodicity and the observation of most cells did not allow to recognize a pattern in migration by eye inspection. Secondly, due to the extremely low contrast of the thin lamellipod extensions, the cell perimeter was mostly unrecognizable on fluorescence images.

When the fluorescence emission was measured at 405nm, similar results were found, suggesting calcium insensitivity of the dye, see Fig. 4.10.

As mentioned above, contradictory relationships of intensity and cell area oscillations were found. As in most acquisitions with our setup, the area obtained by setting a low threshold, resulting in a continuous cell area, followed the change in intensity. Acquisitions with the Nikon setup mostly showed a resulting area that was mirror-inverted to the lapse of the intensity.

In order to investigate the influence of the threshold position, the signal of two medium contrast cells (comparable SNR, measured with our setup) was analyzed, and the intensity and area obtained by setting different intensity thresholds were plotted, see Fig. 4.6(b). If the threshold is set such that only a small fraction of bright pixels in the center of the cell are evaluated, the resulting area is temporarily mirror-inverted to the lapse of intensity. Together with results that will be presented as NAD(P)H oscillations in the next section, this suggests a nontrivial relationship between intensity and area oscillation, which seems to depend on several independent effects.

4.2.4 NAD(P)H-oscillations

In measurements with our setup we found an oscillatory NAD(P)H fluorescence signal in some unstimulated migrating cells. Periods of 10s, 20-30s and 50-70s were observed, see Fig. 4.7.

In our setup, an acceptable SNR at sufficient resolution was obtained when 2x2 binning and an exposure time of 1s was used. When measurements were done in the Nikon Imaging Center with a similar setup, a lamp shutter was used which reduced the illumination time to 20%, and the lamp power was reduced to 5%. This corresponds to an effective illumination power of 1%, as used in our setup, if the power (*EXFO* X-Lite 120) is comparable to a 100W mercury lamp (what has been confirmed empirically by other users).

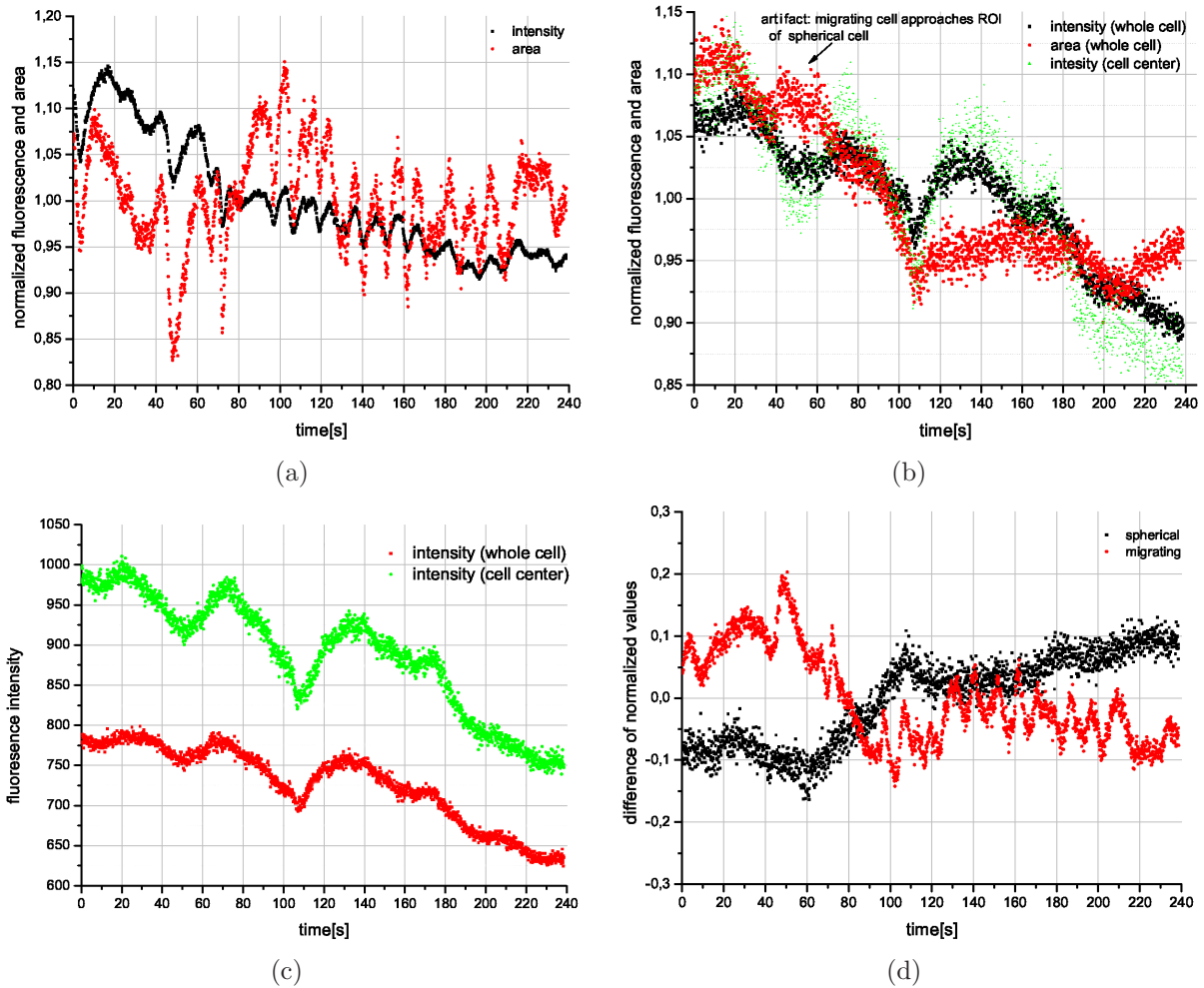


Figure 4.5: Shape oscillations measured by the cytoplasmic fluorescence of indo-1 labelled cells at the isobestic point of the spectrum. A polarized migrating cell (a) and a spherical non migrating (b) were analyzed. Normalized amplitudes are plotted against time. The normalized amplitude of the intensity oscillation in the center of the spherical cell (see purple circle in Fig. 4.3) is compared to the normalized amplitude of the whole cell (c). In order to investigate the relation between intensity and area oscillations, the difference of normalized amplitudes was plotted for both cells (d).

When the cell area was analyzed for measurements with our setup, a higher intensity seemed to coincide with a more compact cell body. This possibly results from data analysis artifacts, see discussion. By eye inspection, during repetitive sequences of 50s oscillations the cell did not move significantly in one direction but appeared to move back and forth, as it was adjusting to a new direction. The similarity to shape oscillations of the same period indicates at least a strong correlation of shape and NAD(P)H signal.

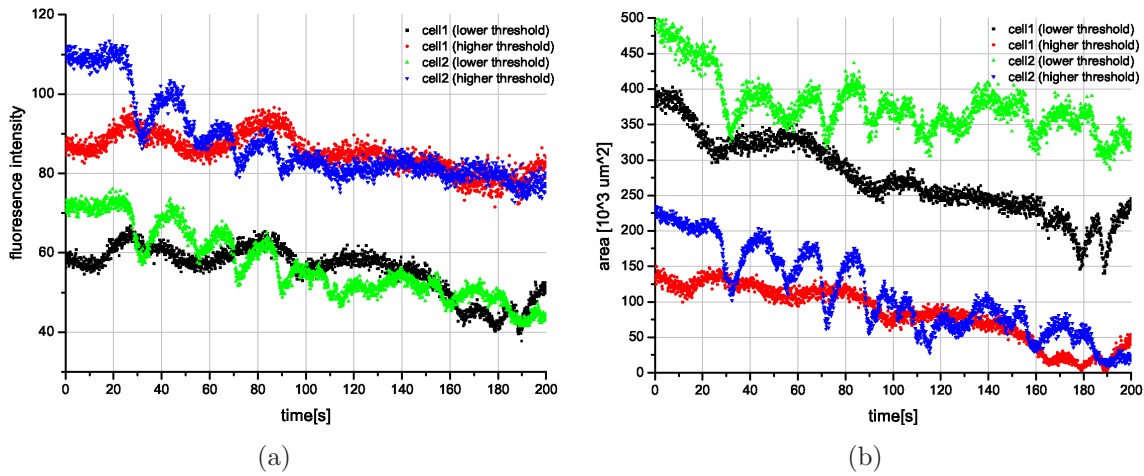


Figure 4.6: Shape oscillations measured with the fluorescence signal of indo-1 labelled cells at the isobestic point of the spectrum. Two cells of comparable SNR were analyzed, and the intensity (a) and area (b) obtained by setting different intensity thresholds were plotted. As in most acquisitions with our setup, the area obtained by setting a low threshold, resulting in a continuous cell area, follows the change in intensity. If the threshold is set such that only a small fraction of bright pixels in the center of the cell are evaluated, the resulting area partially mirrors the lapse of intensity of the cell with the lower frequency oscillation while it is still in phase with the intensity when it switches to a higher frequency mode.

If the area was analyzed with *NIS-elements*, the oscillations of intensity and area was mostly mirror-inverted even for cells with different SNRs that have been measured simultaneously. However, in some acquisitions area and intensity oscillations showed temporarily different periods, see Fig. 4.7(b).

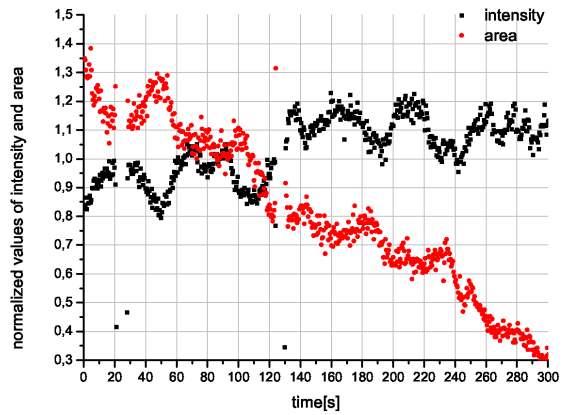
The results reflect those that have been identified as shape oscillations. Furthermore, the relative amplitude of the oscillations was similar. The possible influence of shape oscillations might be reduced, when averaging the signal over the whole CCD chip, see section 4.1.4. However, doing so was not possible in our setup. Without setting a threshold, it was impossible to determine the cell signal against the noise.

4.2.5 Ca^{2+} -oscillations

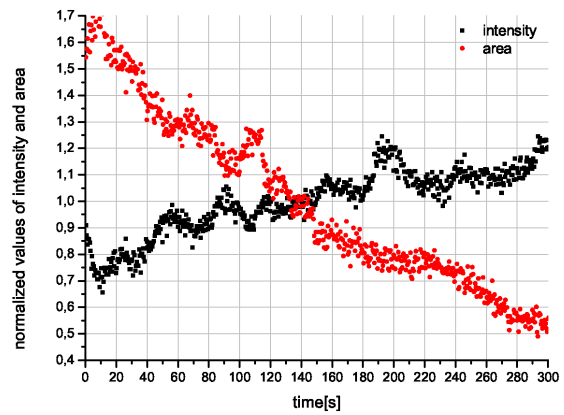
4.2.5.1 Ratio imaging with fura-2

The signal obtained by ratio imaging showed oscillation with periods of 10s and 30s in a few migrating cells that have been preactivated by antibody coated beads, see Fig. 4.8.

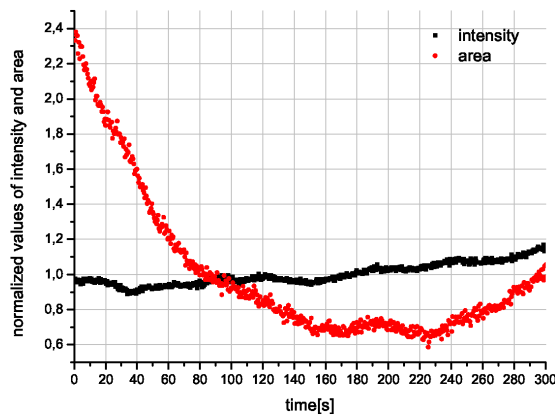
If measured with migrating cells that have been stored in the dark at room temperature for 24 hours, only the signal of a few polarized cells showed oscillatory events with a period



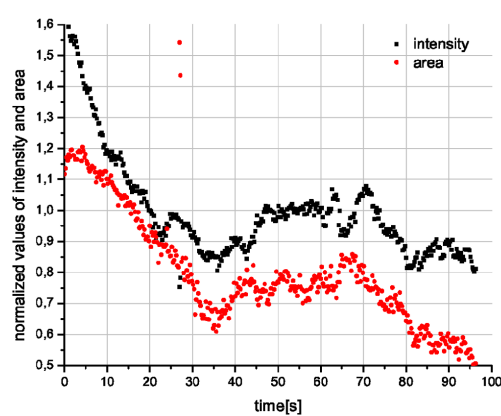
(a) Oscillations of the NAD(P)H autofluorescence signal with a period of 50s and 25s. Area and intensity mirror each other with slight phase shifts (measured with Nikon setup).



(b) Oscillations of the NAD(P)H autofluorescence signal with a period of 30s superimposed to 60s shape oscillations? (measured with Nikon setup).



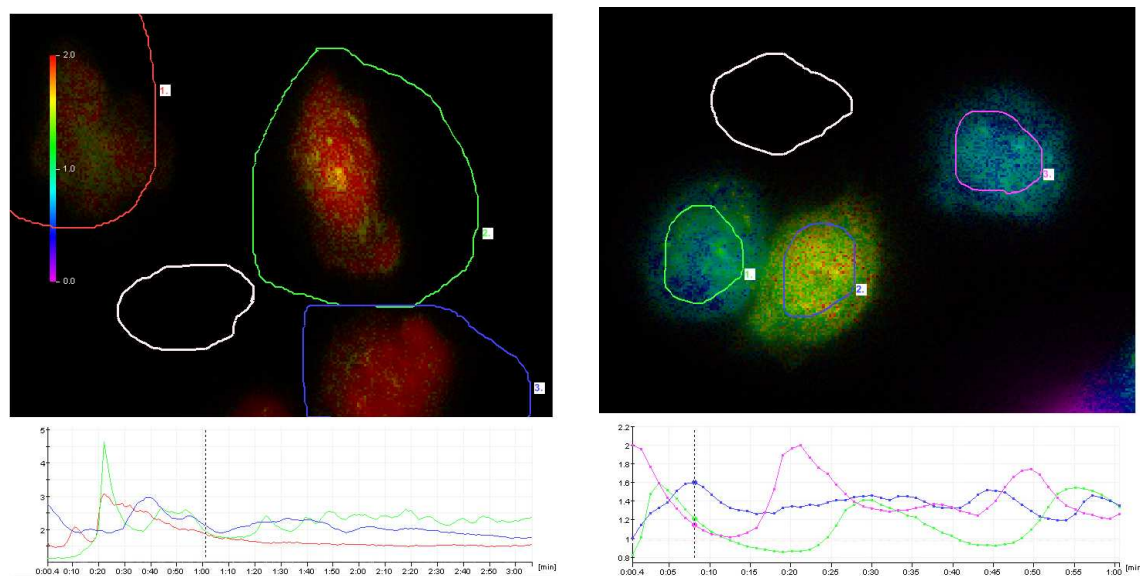
(c) Oscillations of the NAD(P)H autofluorescence signal with a period of 50s at 10% lamp power and 1/5 illumination time, corresponding to an effective lamp power of 2%. The number of analyzed pixels decreases due to the illumination (measured with Nikon setup).



(d) Oscillations of the NAD(P)H autofluorescence signal and/or the cell shape with a period of 10s.

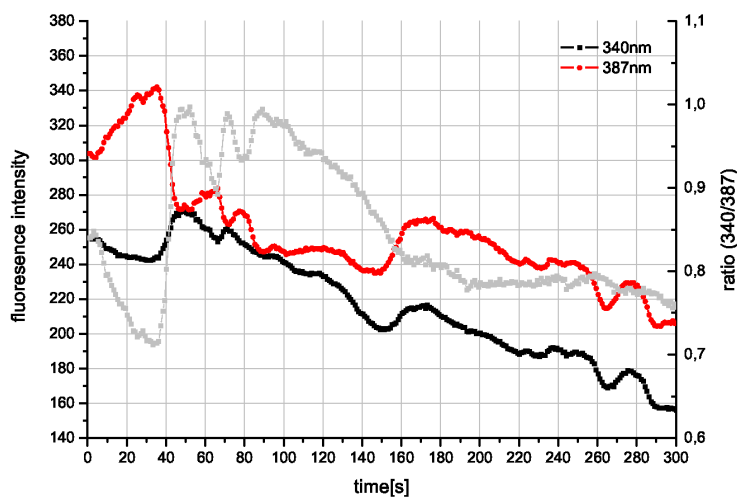
Figure 4.7

of ≈ 30 s. However, comparison of the two signals used for ratio imaging indicated that not all oscillatory events result from calcium oscillations. The ratio imaging is demonstrated in Fig. 4.8(c). If the oscillatory event was parallel in the two channels, it could be identified as artifact since a rise in Ca^{2+} concentration must have opposite effects on the intensity in both channels. Lamp oscillations could be excluded by comparing the signal of cells that have been measured simultaneously. The origin of the oscillation which was parallel in both channels could be a shape oscillation.



(a) Cytosolic Ca^{2+} -oscillations have a period of $\approx 10\text{s}$ in preactivated neutrophils (ratio imaging with Nikon setup).

(b) Cytosolic Ca^{2+} -oscillations have a period of $\approx 30\text{s}$ in preactivated neutrophils (ratio imaging with Nikon setup).



(c) Ratio imaging allows to identify oscillations caused by artifacts. The emission at 340nm and 387nm is plotted together with the ratio against time.

Figure 4.8

4.2.5.2 Single wavelength acquisition with fura-2

Acquisitions with a time resolution of 100ms were done with fura-2 labelled cells using a single excitation wavelength (340nm) in order to detect calcium spikes of a duration

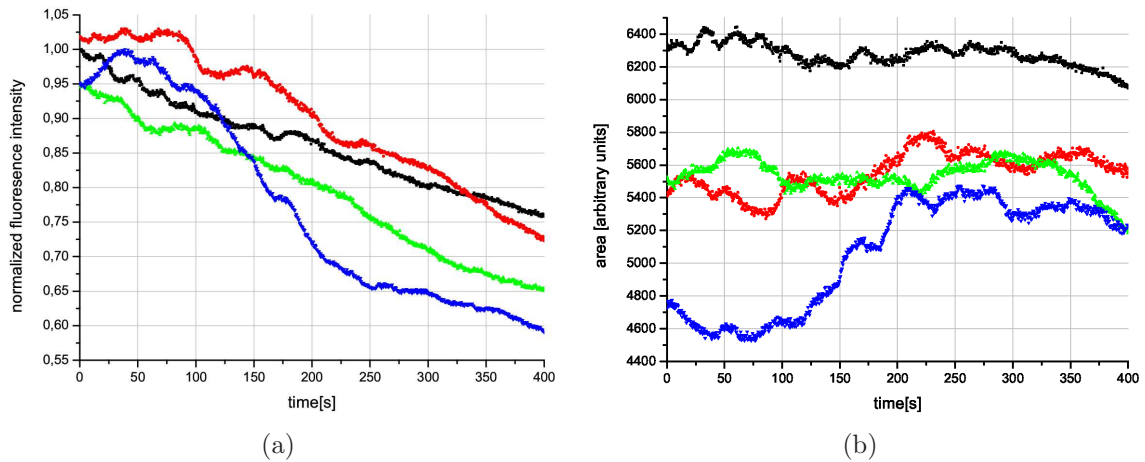


Figure 4.9: Timeseries of single wavelength acquisition with fura-2. The intensity and area of different cells are shown (simultaneously measured with the Nikon setup).

of 200ms. As displayed in Fig. 4.9, sinusoidal oscillations in intensity and area of periods varying from 20s to 50s have been observed. Lamp oscillations can be excluded by comparing the signal of several cells which was measured simultaneously, while artifacts resulting from shaped changes or cell movements can not be excluded without ratio imaging. Since the binding kinetics of fura-1 is slow compared to indo-1, a calcium spike could appear broadened.

4.2.5.3 Single wavelength acquisition with indo-1

Following the protocol of Petty et al., single wavelength measurements with indo-1 labelled cells were done at the calcium sensitive emission wavelength of 405nm and at the isobestic point of the spectrum (450nm) by using the NAD(P)H filter set. The acquisitions at the isobestic point were used to identify shape oscillations, as described earlier. Although a time resolution of 70ms was used, the acquisitions at 405nm did not show the expected spikes, but showed oscillations with temporarily occurring sharp minima, see Fig. 4.10. As mentioned before the calcium sensitivity could not be proven by the addition of ionomycin. The similarity of the results measured at both wavelengths suggests an calcium insensitive emission. Therefore the results could be interpreted as shape oscillations as well.

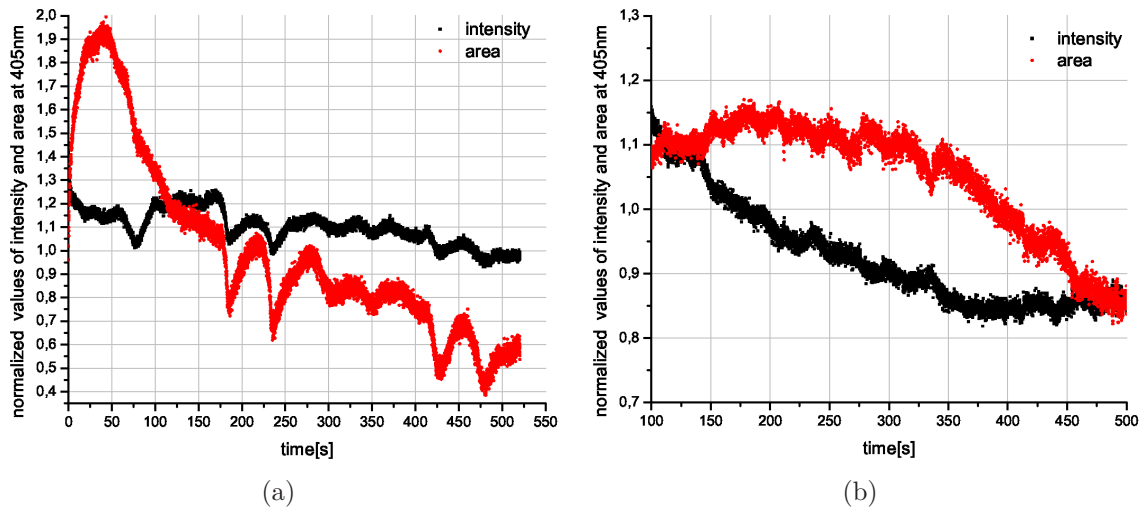


Figure 4.10: Single wavelength acquisitions of indo-1 labelled cells at 405nm. Each frame was taken with an exposure time of 70ms in order to provide a suitable time resolution for the detection of a 200ms spikes as reported by Petty et. al. In contrast, oscillations with periods of 50s and 25-30s are observed.

4.2.6 Problems with spatiotemporal acquisitions

4.2.6.1 NAD(P)H -waves

As mentioned in section 4.2.1.1, our setup is not sensitive enough for spatiotemporal acquisitions at exposure times that are short enough for wave acquisitions at a noninvasive lamp power. However, we tried to capture waves with 100% and 10% illumination power. At full illumination power, no waves were found at exposure times of 1, 5 and 10ms. This might result from the fact that the phenomenon of a selforganized wave is most likely disturbed by lamp intensities that influence the NAD(P)H concentration in such a highly invasive manner as in our setup at 100% lamp power. The resulting images required further image analysis in order to visualize the possibly existing cytoplasmic wave. Due to the UVA illumination, the polymorph nucleus becomes darker (relative to the increasing intensity of the cytoplasm, and smaller objects, possibly mitochondria or granules, became much brighter than the cytoplasm, see Fig. 4.13. By using the *image math* option of *IQ*, the first image (frame) was subtracted from the following frames in order to correct the image for the localized high intensity spots. Since the smaller objects were mobile within the cytoplasm, this methods only worked (theoretically) for a few frames in a row. In order to correct for the high increase in average intensity over time, each image was normalized by its mean intensity. Cell movements were no problem since migration was stopped at this lamp intensities. The resulting images were analyzed by eye inspection in different contrast enhancing options.

The use of medium illumination power (10%) required a gain of 200 in order to reach an exposure time of 10ms. No organelles were recognizable but the images were too noisy to identify any pattern. In addition to image analysis by eye inspection, we tried to confirm the existence of a wave by analyzing the temporal signal of cell parts, which are supposed to oscillate with a period corresponding to ≈ 3 wave transits per second, as displayed in [10]. In order to triple the amplitude of the oscillations and thus the wave intensity, the cells were incubated with PMA (10 μ M for 15 min). However, no difference in the signal intensity was observed and no wave pattern was recognizable in 5 cells that were measured with an exposure time of 10 ms.

4.2.6.2 Ca²⁺-waves

The prerequisite for the detection of the submembrane Ca²⁺-waves reported by Petty et al. is that the sensitivity of the setup allows to decrease the exposure time down to $\approx 200\mu$ s. Since the calcium sensitivity of the emission could not be confirmed by application of the calcium ionophore ionomycin, no experimentally determined minimum exposure time is known for high calcium levels. If a high cytosolic calcium concentration increases the emission intensity 10 times, this limit can theoretically be reached with our setup, see section 4.2.1.2. Thus, it is theoretically possible to detect submembrane Ca²⁺-waves. Unfortunately, the Ca²⁺-spikes which are necessary to time the high-speed acquisition could not be reproduced.

4.2.7 Effect of cell stimulation

Experiments with polarized, non migrating cells In polarized cells that did not migrate or migrating cells which were stopped in their movement due to high lamp power, no oscillation could be induced by stimulation with the combination of FMLP (0.5 μ M) and melatonin (150mg/ml). For such cells, stimulation with INF- γ (25ng/ml, 125ng/ml, 1,25 μ g/ml), glucose (10mM) and PMA (10 μ M) was applied. Even stimulation with *E. coli* had no effect. It is likely that the polarized morphology alone does not require the same degree of viability as it is required for a physiologically working metabolism.

Experiments with highly motile cells The oscillatory signals found in unstimulated highly motile cells showed a larger spectrum of periods as reported by Petty et al. In the few experiments presented above, the effect of stimulation was not studied. However, the cells might potentially be activated by the non-sterile isolation conditions.

4.2.8 Experiments with HT1080 cells

Experiments with the cell line HT1080 were done, since the same phenomena were reported as in neutrophils. The cells did not show any of the expected NAD(P)H signals when a full lamp power was applied. Migration was not recognizable by eye inspection, indicating improper cell handling.

4.3 Discussion

The major task of this project was to optimize biological and technical conditions simultaneously, each field being challenging itself, and difficult to optimize independently from each other. The biological part, namely cell handling and lamp intensity was considered as optimized when the cells were migrating and oscillatory signals were measured. However, the nature of the oscillations needs to be discussed. Especially, the influence on the data analysis method on the results has to be discussed. Furthermore, there are technical limitations and artifacts which have caused the failure to reproduce the results of Petty et al.

4.3.1 Shape oscillations and/or concentration oscillations?

Setting an intensity threshold in order to determine cell shapes from fluorescence images is a commonly accepted method. Recently, a new software application called *CellSegmenter* was developed to quantify cell shapes [42]. The program is based on simple intensity thresholding [43] but allows individual thresholds for each cell.

As displayed in Fig. 4.12(a), shape oscillations are expected to have a fixed phase relation relative to other cellular oscillators such as NAD(P)H and Ca^{2+} . Since shape oscillations are likely to be superimposed to NAD(P)H and calcium oscillation, we tried to distinguish the origin of the oscillating fluorescence in our data by analyzing the phase relation of area and intensity oscillation.

However, when intensity thresholding was applied to the data presented above, no clear relationship of cell area and averaged fluorescence intensity was found. For this specific application, several independent problems reduce the reliability of the intensity threshold method.

The most basic problem is that, apart from shape oscillations, there might be other effects which cause the fluorescence emission to oscillate. Although measuring at an isobestic point generally implicates calcium insensitivity of the fluorescence emission, the emission spectra found in the literature could be slightly different, e.g. due to variations of the pH. However, it can be excluded that the sharp minima in the oscillating fluorescence of our data correspond to Ca^{2+} -spikes, since the signal at the calcium sensitive wavelength

(405nm) did not show peak like maxima. However, there might be other shape independent effects that periodically modulate the emission of indo-1 at 450nm (e.g. the pH). The similarity to the results of Ehrenguber et al. (see section 2.5) which reported shape oscillations of identical periods, is most convincing. It seems likely that the sharp peak like minima correspond to a contracted cell shape where the cells adjust to a new direction while the smooth maxima corresponds to the straight-line movement.

If, for an unknown reason, the emission spectrum of indo-1 in the cells measured with our setup is significantly different from the spectrum published by the manufacturer, the results have to be re-interpreted. The potential shape oscillations could simply be pure calcium oscillations, or periodic calcium spikes which appear as sharp emission minima.

In addition to uncertainties regarding the signal origin, the contrast of the image, as well as the position of the threshold relative to the data histogram determine the reliability of the intensity threshold method. It was shown that the threshold position can significantly influence the results, see Fig. 4.6. Intensity and area oscillated in phase in high contrast acquisitions. However, when the contrast was decreased by shortening the exposure time, the results were still in phase when a too high threshold was applied (no continuous cell area). When a low threshold, leading to a continuous cell area was applied, intensity and area were mirror-inverted. This can not be explained based on the data available. When cells of different image contrast were simultaneously measured in the Nikon Imaging Center (due to inhomogeneous illumination), image analysis with the same threshold for all cells resulted in a cell area that was the mirror-inverted intensity. Due to this inconsistency, the relationship of cell area and intensity oscillation can not be interpreted without further investigations. Especially, it can not be used to identify the origin of particular oscillating fluorescence signal.

There might be a physical explanation for the above-described inconsistency regarding influence of image contrast and threshold position on the results. The position of the cell body relative to the focal plane determines the distribution of the fluorescence signal over the CCD chip. This signal distribution is nontrivial for two reasons; Firstly, the influence of the depth of focus on the signal distribution is not trivial. Secondly, a variety of movements of particular cell parts, such as the thin lamellipod extension or thick pseudopod extension, relative to the focal plane are possible.

Even an adherent cell will have a much larger axial extension than the typical depth of focus of 200nm. Thus, only the thin lamellipod extensions might roughly fit into the depth of focus. Assuming the focal plane to be in the center of the lamellipodia, cell contraction will decrease the cell area and thus increase the intensity averaged over the cell area, as predicted from the theory, see section 4.1.4.

While this might crucially determine a pixel based data analysis, it is certainly less important if the signal is averaged over the whole chip, as it happens when purely temporal acquisitions are done with a PMT. Hence, the results of Petty et al. could be indeed pure concentration oscillations, while our data likely shows superimposed shape oscillations. Unfortunately, the weak signal of unlabeled migrating cells could not be analyzed without

an intensity threshold.

4.3.2 Technical problems and limitations

4.3.2.1 Is the sensitivity of our setup sufficient to detect spatiotemporal waves?

A general problem of this project was that only little was known about the strength of the purely temporal signal reported by Petty et al. On the one hand, the amplitude of the NAD(P)H oscillations was reported to be 3 – 10% of the absolute NAD(P)H level, and should therefore be detectable if the noise is $< 3\%$. On the other hand, the setup established by Petty et al. suggested the need for high sensitivity. When the NAD(P)H sensitivity of our setup was investigated experimentally with NADH dilutions, it was found to be at the limit to detect the oscillations. Since exposure times short enough for wave acquisitions were used for this experiment, the setup should theoretically be able to detect a NAD(P)H-wave. However, the experiment which is basis for these estimations could not be reproduced, probably due to the age of the purified NADH. If the sensitivity is characterized by the minimum achievable exposure time, we also find the sensitivity to be on the limit. An exposure time of 10ms could only be achieved at a lamp power of 10% which was found to be invasive.

The sensitivity required for spatiotemporal calcium measurements was estimated based on experimental and theoretical data of our setup and the published data of Petty et al. We found that exposure times larger than $5\mu\text{s}$ are needed to detect one fluorescence photon with our setup. This implicates that acquisitions with exposure times in the nanosecond range, as reported by Petty et al. are not possible with our setup. The minimum exposure time that allowed to recognize the cell body at steady state calcium concentrations was 2ms, which is ten times longer than required for the calcium wave detection. However, as explained before, the emission appeared to be calcium insensitive. Since the emission intensity is expected to increase (up to ten times) at high calcium concentrations, it is theoretically possible to reach an exposure time of $200\mu\text{s}$. Thus, the sensitivity could be sufficient for calcium wave detection, if the labelling is optimized.

4.3.2.2 Lamp spikes and oscillations

Several types of lamp spikes and oscillations have been observed, unfortunately with the same periods as reported for the neutrophil oscillations. Lamp oscillations were usually measured by analyzing the constant signal of fluorescent beads. As displayed in Fig. 4.11(a), characteristic lamp spikes are also present in the background.

After the bulb (USH-1030L, *ushio*) was used for about 50 hours, spiky fluctuations of up to 30% normalized amplitude (Fig. 4.11(a)) occurred, which temporarily had a transient

shape, see Fig. 4.11(b). A fresh bulb (hbo, *osram*) showed fluctuations of $< 2\%$ amplitude, see Fig. 4.11(c). When used in a different lamp house with a different controller (*Kübler*, ebq100 isolated), the same bulb type showed spontaneous oscillations with periods of 20s, 40s, 50s, 100s, depending on the working hours, see Fig. 4.11(d,e). Since lamp fluctuations can occur spontaneously during acquisitions, it is necessary to distinguish whether the signal modulation was caused by the illumination or actually by varying emission. Therefore two cells were measured simultaneously and lamp fluctuation could be excluded if their signal was modulated differently. When single cells were measured, the relative intensity of the fluctuation was compared to the relative fluctuation of the dark current corrected background. Similar relative amplitudes identified lamp oscillations, lower relative amplitude in the background suggested stray light to be the origin the background oscillation.

4.3.3 Biological problems

4.3.3.1 Influence of cell preparation on cell behavior

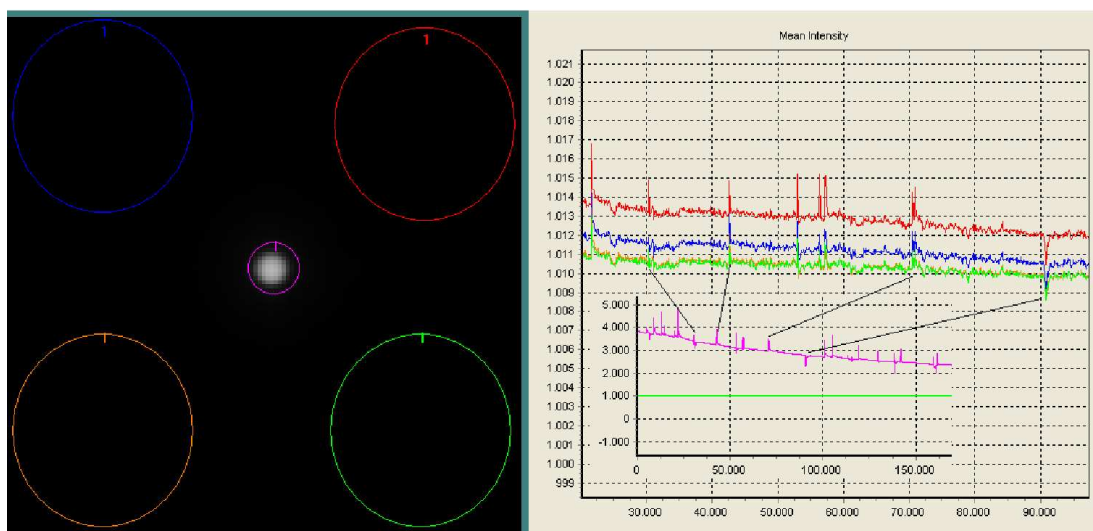
Neutrophils are fragile cells that can be easily damaged by improper handling. Thus, slight differences in handling might disturb the cells although they are viable and migrate.

A possible reason for the irregularity of the observed oscillations could be the compound sodium diatrizoate, which is included in *Polymorphprep*. Although it can effect the cell viability [44] it is commonly used for immunologic research. Cells isolated by repetitive lysis alone were never found to oscillate, when examined with fura-2 ratio imaging or with our setup, at high lamp power. However the NAD(P)H in such cells was never measured using low lamp intensities. Although cells isolated with ficoll, followed by 4 times lysis as described above, did not appear to be more viable, the failure of this method possibly had other reasons. For future investigations, isolation following the Petty protocol should be applied. Alternatively, lysis can be avoided by washing off the erythrocytes manually from the cover slide, after the neutrophils have adhered.

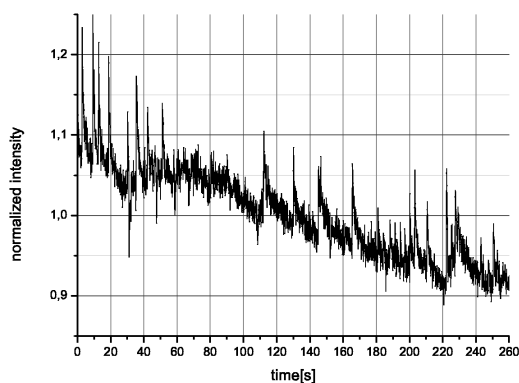
Since most cells showed irregular oscillatory signal, it is a major question if and how this irregularity influences spatiotemporal patterns. It seems likely that these patterns are disturbed as well. Thus, they might be undetectable by eye inspection, or by a data analysis which is based on the assumption that a wave periodically modulates the intensity of cell parts.

4.3.3.2 NAD(P)H increase due to UVA irradiation

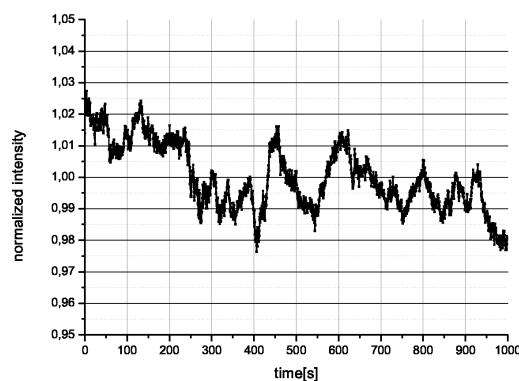
Since the UVA irradiation was found to be highly invasive for cells, we had to reduce the lamp intensity at least by a factor of ten.



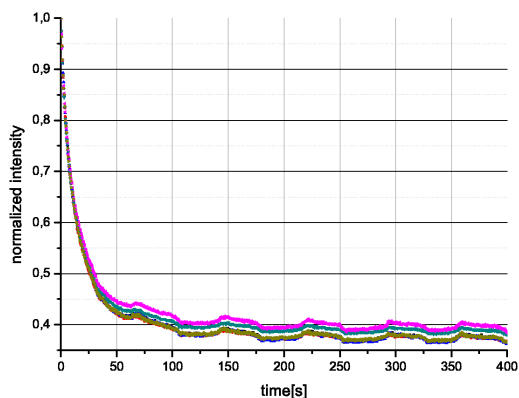
(a) Lamp spikes of the ushio bulb in our setup measured with a fluorescent bead (left image in the middle) and compared to the background fluctuations. A timeseries of the fluorescence intensity is shown in the right image. In order to distinguish lamp spikes from stray light the relative amplitude of the spikes was compared.



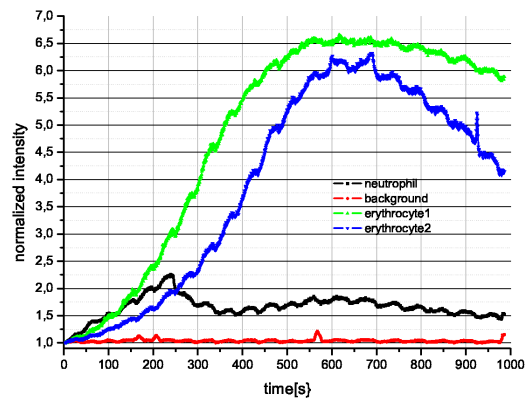
(b) Transient spikes with a period of 20s, measured with ushio hbo bulb in our setup.



(c) Chaotic lamp noise ($< 2\%$) of osram hbo bulb in our setup.

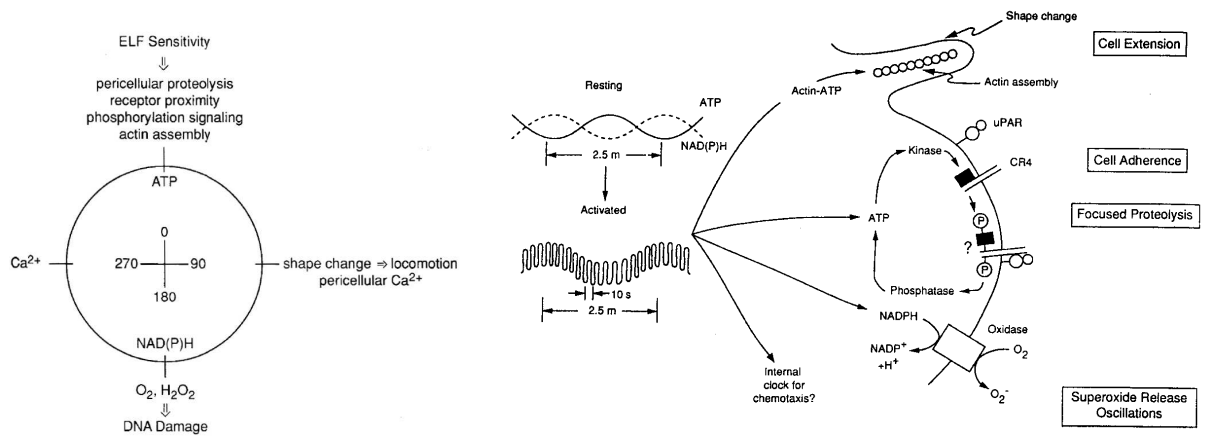


(d) Lamp oscillations of osram hbo bulb in Leika setup, measured with a slide with fluorescent coating.



(e) The NAD(P)H fluorescence signal of several blood cells is measured simultaneously. A lamp oscillation of osram hbo bulb in Leika setup make the signal look like a synchronized oscillation in neutrophils and erythrocytes.

Figure 4.11



(a) Experimentally found phase relations (b) Hypothetical model for the coupling of different oscillators in cellular biochemistry and function [1] [1]

Figure 4.12

The described influence of UVA on the NAD(P)H concentrations might disturb or even destroy a selforganized phenomenon such as a travelling wave.

The increase NAD(P)H concentration due to UVA illumination was also observed in HT1080, breastcancer cells, erythrocytes and yeast cells indicating a nonspecific mechanism. Among blood cells, the effect was most distinct in erythrocytes. Since the fluorescence signal increased, an increased reduction from the non fluorescent NAD(P)⁺ to the fluorescent NAD(P)H can be presumed and a direct oxidative effect can be excluded. It can only be speculated if this is an indirect effect of the reactive oxygen species, or if there is a UVA sensitive mechanism in the PO (peroxidase-oxidase) reaction, which is the enzymatic reduction of oxygen by NADH.

4.3.3.3 Biological complexity

The data currently available suggest that several types of cellular oscillators are superimposed and might be coupled.

Shape oscillations are likely to modulate various cell properties. Changes of the membrane surface implicate changes of distances of membrane proteins. This is crucial for interactions such as those of CD4 and uPAR receptors, which was shown to oscillate by FRET measurements (Förster resonance energy transfer), see [1]. Apart from purely mechanical effects, the electrical properties of the plasma membrane depend on membrane thickness and surface. Both, mechanical and electrical effects might have an impact on ion channel activities.

Since periodic oscillations in the F-actin content accompany shape oscillations in suspension, it was suggested that cyclic actin polymerization could be the driving force for shape oscillations. A coupling of cyclic actin polymerization to oscillating Ca^{2+} and ATP levels would be plausible, but has not been shown yet.

In a rather speculative model, see Fig. 4.12(a), Petty summarizes how oscillations of NAD(P)H and ATP concentration might be translated into a repetitive sequence of biochemical reactions in the extracellular matrix, in order to promote locomotion. An oscillating signaling machinery simultaneously phosphorylates CR4 and/or associated proteins, leading to CR4-uPAR coupling. This coupling is supposed to focus pericellular proteolysis next to integrin adherence sites, where then, actin assembly and cell extension proceed, when ATP is at its peak [1].

4.4 Conclusion

4.4.1 An ideal setup for detection of biochemical oscillations

4.4.1.1 A stable light source

Lamp spikes and oscillations of similar periods as the expected fluorescence signal have been observed. Thus a stable light source is a necessity for future investigations. Lamp sources with increasing importance in microscopy are LEDs (light emitting diodes), which have been reported to have fluctuations of less than $< 0.03\%$ [45]. Recently, UVA emitting LEDs (with a maximum at 365nm) with sufficient power have become commercially available, e.g from *Rapp Optoelectronic* or *Pizmatix*. Continuous and pulsed excitation is possible with one system, replacing a lamp shutter in its function of reducing phototoxicity. Illumination power up to 100mW is possible, depending on the NA (numerical aperture) and the diameter of the light guide. Recall, that the illumination power that has been found to be most undisturbing for cells was $\approx 2\mu W$.

The disadvantage of using LEDs is that they are single wavelength sources only. However, a multi-color LED illumination system is offered by *Rapp Optoelectronic*. Alternatively, super-quiet mercury or xenon lamps are offered by *Hamamatsu*. Noise reduction is done by both barium impregnated cathodes and rapid current adjustments in the power supply, which usually adds 2% of noise [45]. While the costs of a LED with power supply are $\approx 1500\text{€}$, noise controlled lamps are available from $\approx 4000\text{€}$ on.

4.4.1.2 Multiparameter measurements

As discussed above, applying a simple intensity threshold was not sufficient to obtain reliable results for changes in cell area or shape. For a more reliable segmentation that is

necessary to study shape changes with widefield microscopy, one could label any protein located on the membrane to get a strong signal from the cell perimeter.

If the main intention is to exclude artifacts resulting from shape changes, a membrane permeable fluorophore that uniformly labels the cytoplasm, such as ethidiumbromide (if measured fast enough to prevent binding to DNA) could be used for calibration, if detected simultaneously. By labeling neutrophils with CFDA-AM (5-carboxyfluorescein diacetate-acetoxymethylester, 0.5mg/ml, 30min at 37°C) it could be excluded that oscillations in cell thickness accounted for the traveling NAD(P)H waves [4]. This membrane permeant dye can be imaged using filter sets for fluorescein ($\lambda_{ex} \approx 488\text{nm}$, $\lambda_{em} \approx 530\text{nm}$). If spectral crosstalk is minimized and taken into account, this dye could be used for a dual wavelength acquisition. Similarly to Ca^{2+} -ratio imaging, parallel signal modulations in both detection channels would indicate shape change induced signal modulation.

4.4.2 An ideal setup for detection of waves

Although an ICCD is necessary to reach exposure times below $100\mu\text{s}$ which was shown to significantly improve the contrast, the signal in our experiments was not even strong enough to reach the limits of our camera. Using a lamp shutter would allow higher illumination intensities and thus a higher photon yield. A shutter with a minimum opening time of 2ms (*Uniblitz*) would allow to reduce illumination time fifty times at interframe times of 100ms, thus facilitating acquisitions at exposure times that could otherwise only be reached with the full lamp power.

In case of the submembrane Ca^{2+} -waves that only appear for 200ms every 20s, one could open the shutter once every 30ms. For a shutter with an opening time of 2ms, this would reduce the UVA dose 15 times. Since the waves occur only each 20s, one could additionally limit the acquisition time to $\approx 5\text{s}$, which reduces the illumination time by a factor of 4, but still ensures not to miss the wave.

4.4.2.1 A different approach - High-speed TIRF acquisitions with Calcium Green Flash

Alternatively to improvements on the technical side, another method could be used to detect submembrane calcium waves. Recently, a new calcium indicator called Calcium Green Flash (CaGF) was developed which allows to image calcium microdomains on sub-millisecond timescales around the mouth of open Ca^{2+} -channels, see [46]. CaGF combines the advantage of small-molecule indicators whose fluorescent response is very rapid, with the benefit of genetically encoded indicators in that it can be targeted to a protein of interest, [47]. With an K_d of $100\mu\text{M}$, CaGF has an off-rate which is ≈ 500 times faster as the respective value of indo-1. The fact that it is localized at the channel of interest should

dramatically increase the SNR compared to experiments using indo-1. In addition, using a TIRF microscope for fluorescence acquisitions further improves the SNR compared to the setup of Petty et al.

If tagged to genetically targeted L-type calcium channels in HEK293 cells, hot spots of fluorescence were observed upon depolarization, indicating dense microdomains of active channels, while most calcium channels were closed. This was concluded to be the result of a nonuniform distribution of responsive channels, what could not have been measured with other calcium indicators before.

If this method would be used to detect submembrane calcium waves, the first step would be to transfect a T-type channel with a tetracysteine motif (the target to which CaGF attaches) which must then be stably expressed by the cell. The CaGF is then added to the cell medium in AM ester form, like other calcium indicators. Since transfections take about one day, one should try this only if other phenomena that have been found to accompany the waves, can be detected in a reliable periodicity and regularity in one-day old neutrophils, before taking the effort of establishing the transfection.

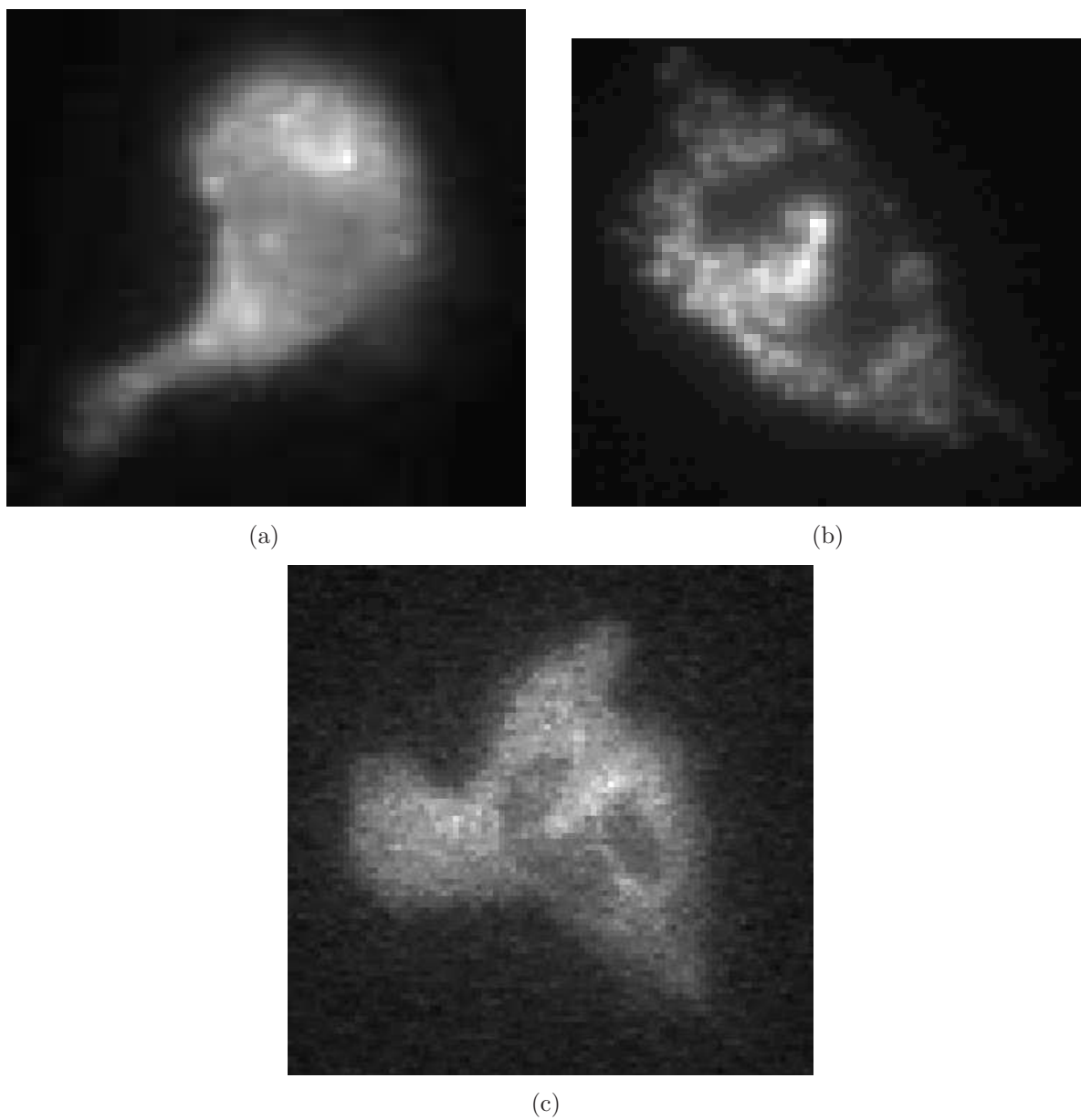


Figure 4.13: Autofluorescence images of neutrophils exposed to high doses of UVA. Granules and the polymorph nucleus are recognizable.

Chapter 5

Modeling of a submembrane Ca^{2+} -wave

In the following, a model for the submembrane Ca^{2+} -wave in migrating neutrophils is presented as the current version of an article.

Chapter 6

Summary

The microscope setup used for collecting fluorescence image series of spatiotemporal events in living cells was constructed. This was realized by combining commercial modular components. It consists of an inverted widefield microscope IX70, an EMCCD camera as detector, an incubation chamber to maintain physiological conditions and other optical or electrical accessories that are needed to control system performance.

The EMCCD camera was characterized by its spatial and temporal resolution and the real gain factor achievable, dependent on temperature and readout rate. Furthermore, the behavior of readout noise, clock induced charge production and dark current was studied at different acquisition settings. The dominating noise source was found to be charge produced by horizontal clocking in the readout register at readout rates of 10MHz.

The light collection efficiency of our setup was compared to the setup established by Petty et al. By taking the transmission properties of optical components and the quantum efficiency of the detectors into account, our setup outperforms the setup of Petty et al. However, the higher amplification factors achievable by an ICCD and a PMT might increase the sensitivity of the Petty setup compared to our setup. Furthermore, Petty et al. minimized potential sources of autofluorescence by using a quartz objective.

The ability of our setup to detect a submembrane Ca^{2+} -wave was quantified. This was done by comparing the power density of the fluorescence emission at the sideport of our microscope, to the minimum local power density that must be present in the setup of Petty et al. Based on the published fluorescence images of the wave which must represent at least two photons per pixel at an exposure time of 50ns, we get $4\mu\text{W}/\text{cm}^2$ as the minimum local power density. This was found to be only 25 times weaker than the highest excitation power density that was applied for cell measurements in our setup. Thus, an extremely high photon yield of fluorescence emission must be present in the setup of Petty et al. In order to obtain an upper limit for fluorescence power densities on the side port of our setup, a dense layer of fluorescent beads was used as sample. The averaged emission power density was found to be 100 times lower as the minimum local power density in the setup

of Petty et al. Thus, $5\mu\text{s}$ is the minimum exposure time which is required to detect a single photon with our setup. Following this estimation, 40 photons are the expected signal for an exposure time of $200\mu\text{s}$, which was reported to be the maximum exposure time at which wave detection is possible.

The minimum exposure time achievable with our setup was further investigated experimentally with indo-1 labeled neutrophils. The fluorescence emission at steady state calcium concentrations allowed to decrease the exposure time down to 2ms, which was reported to be insufficient for wave detection by Petty et al. Due to problems with the dye, the minimum exposure time at high calcium levels, and thus increased fluorescence emission could not be measured. Therefore, the minimum exposure time theoretically achievable was estimated based on the known spectral properties of indo-1 to be $200\mu\text{s}$. Thus, an exposure time at which Ca^{2+} -wave acquisitions are possible can be theoretically achieved with our setup, under optimized labelling conditions.

The NAD(P)H-sensitivity of our setup was measured with NAD(P)H dilutions and compared to a Leika setup based on an EBCCD camera (University of South Denmark, Odense). Our setup was found to be more sensitive as the Leika setup, which is capable to detect NAD(P)H-oscillations in single yeast cells. This suggests that the NAD(P)H sensitivity of our setup is in the right order of magnitude to detect NAD(P)H-oscillations in single neutrophils.

The detection limit of 100nM NADH, measured with a dilution, can not be compared to the measurements of NAD(P)H concentrations in cells because they do emit in a smaller volume. Using a correction factor which accounts for the different sample heights of cell and dilution, it could be concluded that the NAD(P)H-sensitivity of our setup is sufficient to detect changes $20\mu\text{M}$ NAD(P)H within a cell. This might allow to detect the oscillation that range from $180\text{-}350\mu\text{M}$ with our setup.

In the second part of this thesis, measurements with freshly isolated human neutrophils were carried out using the described setup and a similar microscope in the Nikon Imaging Center (Bioquant, University of Heidelberg). The results are outlined in the following.

The UVA excitation was found to be highly invasive at full lamp power. The NAD(P)H emission intensity increased up to 300% and the cells stopped their movements. This effect was reduced at 10% lamp power and was absent for 10min at 1% lamp power.

The NAD(P)H detection limit in neutrophils was characterized by the exposure time that could be achieved at a certain lamp intensity. It was found that a noninvasive lamp power required exposure times of $>100\text{ms}$ to detect a signal. The exposure time required for wave detection (10ms) could only be achieved with a medium lamp power (10%).

The possible effect of shape oscillations on the appearance of a constant cytoplasmic signal in our setup was investigated by measuring the signal of indo-1 labelled cells at 450nm, an isobestic point of the spectrum. Oscillations with periods of 10s, 20s and 50s were found. By setting an intensity threshold, the cell area was measured which indicated an oscillating

cell shape. However, the method was found to be fairly susceptible to artifacts and did not allow to determine a clear relationship of intensity and cell area oscillation.

When the NAD(P)H autofluorescence was analyzed with the intensity threshold analysis, oscillations of similar periods were found, which suggest at least a strong correlation to shape oscillations. However it could not be excluded, that shape oscillations are superimposed to the pure NAD(P)H-oscillations.

Furthermore, the cytoplasmic calcium concentration was investigated by ratio-imaging and single wavelength acquisitions of fura-2 labeled cells. As expected, some oscillatory events could be identified as Ca^{2+} -oscillations with periods of 10s and 30s, while others were identified as artifacts, likely caused by shape oscillations. In order to detect Ca^{2+} -spikes which are crucial to determine the rhythm of Ca^{2+} -wave transits, single wavelength measurements were done with indo-1, a dye which is more suitable to detect fast concentration changes. However, when using a suitable time resolution, no sharp, spike-like maxima were found as reported by Petty et al. In contrast, oscillations with sharp peak-like minima, with a period of 50s were observed. This might be explained by a problem with the dye leading to calcium insensitivity of the emission. This is supported by the fact that calcium depletion did not lead to the expected signal increase, as well as that the signal shape was similar to the signal measured at the isobestic point of the spectrum.

Imaging of NAD(P)H waves at medium and high lamp power failed, possibly due to the invasiveness of the UVA illumination. Unfortunately, at a noninvasive lamp power, exposure times of $>100\text{ms}$ were required to detect a NAD(P)H signal. Stimulation with PMA, which was reported to increase the contrast three times, did not allow to identify a wave pattern at medium lamp power either.

Imaging of Ca^{2+} -waves failed since no temporal spikes were found in indo-1 labelled cells.

In the third part of this thesis, a mathematical model for the propagation of the submembrane Ca^{2+} -wave was constructed. This was done in collaboration with Mario Mommer (IWR/BIOMS).

The key participants in wave propagation were identified based on the experiments by Petty et al. The data suggest that the low voltage gated T-type calcium channel plays a key role, implicating the importance of membrane potential. Since the periodic depolarization, which correlates with the wave transit, is reduced by blocking the T-type channels, a transmembrane Ca^{2+} -influx through these channels was assumed to have an effect on the membrane potential. Influences of other calcium sources or ion channels are assumed to have no direct effect on the propagation mechanism.

A simple voltage dependent gating model was used to describe the T-type channel behavior. A formulation for the spatial variation of membrane potential produced by a transmembrane current was found in the literature. The spatial coupling of membrane potential and T-type channel gating was implemented by Mario Mommer. The parameters of the model were related to physiological values based on the experimental data available for similar

cell types.

Depending on the total transmembrane current which was estimated by the model, the number of participating channels was derived. Furthermore, the rise in intracellular Ca^{2+} -concentration and the associated change in potential were estimated. The results suggest that other mechanisms must compensate for the large change of membrane potential that would be produced by the calcium influx during one wave transit. The model reproduced robustly the experimentally observed wave behavior, namely, wave speed, reflection and a tendency to asymmetry. Details and results of this work are presented as an article.

Bibliography

- [1] H.R. Petty. *Self-Organized Biological Dynamics and Nonlinear Control by External Stimuli*, chapter Oscillatory signal in migrating neutrophils: effects of time-varying chemical and electric fields, pages 173–192. Cambridge University Press, 2000.
- [2] A.L. Kindzelskii and H.R. Petty. Intracellular calcium waves accompany neutrophil polarization, formylmethionylleucylphenylalanine stimulation, and phagocytosis: A high speed microscopy study. *J. Immunol.*, 170:64–72, 2003.
- [3] H.R. Petty. Spatiotemporal chemical dynamics in living cells: From information trafficking to cell physiology. *Biosystems*, 83:217–224, 2006.
- [4] H.R. Petty and A.L. Kindzelskii. Dissipative metabolic patterns respond during neutrophil transmembrane signaling. *PNAS*, 98:3134–3149, 2001.
- [5] A.L. Kindzelskii and H.R. Petty. Apparent role of traveling metabolic waves in oxidant release by living neutrophils. *PNAS*, 99:9207–9212, 2002.
- [6] S. Inoue. *Video Microscopy*. Springer, 1986.
- [7] Electronic imaging detectors. www.olympusmicro.com.
- [8] Digital cameras. www.andor.com.
- [9] Tutorial: Optimizing your signal to noise ratio. www.roperscientific.com.
- [10] H.R. Petty, R.G. Worth, and A.L. Kindzelskii. Imaging sustained dissipative patterns in the metabolism of individual living cells. *Phys. Rev. Lett.*, 84:2754–2757, 2000.
- [11] M. Naraghi and T.H. Müller. Two-dimensional determination of the cellular Ca^{2+} binding in bovine chromaffin cells. *Biophys. J.*, 75:1635–1647, 1998.
- [12] M.U. Ehrengruber, D.A. Deranleau, and T.D. Coates. Shape oscillations of human neutrophil leukocytes: characterization and relationship to cell motility. *J. Exp. Biol.*, 199:741–747, 1995.
- [13] H.P. Ting-Beall, D. Needham, and R.M. Hochmuth. volume and osmotic properties of human neutrophils. *Blood*, 84:2774–2780, 1993.

- [14] M.U. Ehrengruber, T.D. Coates, and D.A. Deranleau. Shape oscillations: a fundamental response of human neutrophils stimulated by chemotactic peptides? *FEBS*, 359:229–232, 1995.
- [15] J.B. Huang, A.L. Kindzelskii, A.J. Clark, and H.R. Petty. Identification of channels promoting calcium spikes and waves in ht1080 tumor cells: Their apparent roles in cell motility and invasion. *Cancer Res.*, 64:2482–2489, April 2004.
- [16] U. Kummer, J. Zobeley, J. Brasen, R. Fahmy, A. Kindzelskii, A. Petty, A.J. Clark, and H.R. Petty. Elevated glucose concentrations promote receptor-independent activation of adherent human neutrophils: An experimental and computational approach. *Biophys. J.*, 92:2597–2607, 2007.
- [17] P.N. Prasad. *Introduction to Biophotonics*. Wiley-Interscience, 2003.
- [18] J.R. Lakowicz. *Principles of Fluorescence Spectroscopy*. Springer, 2006.
- [19] G. Löffler. *Basiswissen Biochemie*. Springer, 2000.
- [20] A.J. Rosenspire, A.L. Kindzelskii, and H.R. Petty. Interferon- γ and sinusoidal electric fields signal by modulating nad(p)h oscillations in polarized neutrophils. *Biophys. J.*, 79:3001–3008, 2000.
- [21] A.L. Kindzelskii, M.M. Eszes, R.F. Todd, and H.R. Petty. Proximity oscillations of complement receptor type 4 and urokinase receptors on migrating neutrophils are linked with signal transduction/metabolic oscillations. *Biophys. J.*, 73:1777–1784, 1997.
- [22] Y. Adachi, Kindzelskii A.L., N. Ohno, T. Yadomae, and H.R. Petty. Amplitude and frequency modulation of metabolic signals in leukocytes: Synergistic role of ifn- γ in il-6-and il-2-mediated cell activation. *J. Immunol.*, 163:4367–4374, 1999.
- [23] A.J. Rosenspire, A.L. Kindzelskii, and H.R. Petty. Pulsed dc electric fields couple to natural nad(p)h oscillations in ht-1080 fibrosarcoma cells. *J. Cell Sci.*, 114:1515–1520, 2001.
- [24] G. Dupont and A. Goldbeter. Oscillations and waves of cytosolic calcium: insights from theoretical models. *BioEssays*, 14:485–493, 1992.
- [25] A.P. Thomas, G.J. Bird, G. Hajnoczky, L.D. Robb-Gaspers, and J.W. Putney. Spatial and temporal aspects of cellular calcium signaling. *FASEB*, 10:1505–1517, 1996.
- [26] G.W. Sullivan, G.R. Donowitz, J.A. Sullivan, and G.L. Mandell. Interrelationships of polymorphonuclear neutrophil membrane-bound calcium, membrane potential, and chemiluminescence: Studies in single living cells. *Blood*, 1984.
- [27] D.E. Burgess, O. Crawford, B.P. Delisle, and J. Satin. Mechanism of inactivation gating of human t-type (low-voltage activated) calcium channels. *Biophys. J.*, 82:1894–1906, 2002.

- [28] Edward Perez-Reyes. Molecular physiology of low-voltage-activated t-type calcium channels. *Physiol. Rev.*, 83:117–161, 2003.
- [29] M.E. Jaconi, R.W. Rivest, W. Schlegel, D.R. Wollheim, and P.D. Lew. Spontaneous and chemoattractant-induced oscillations of cytosolic free calcium in single adherent human neutrophils. *J. Biol. Chem.*, 263:10557–10560, 1988.
- [30] L.F. Jaffe. Classes and mechanisms of calcium waves. *Cell Calcium*, 14:736–745, 1993.
- [31] Andrei L. Kindzelskii and Howard R. Petty. Ion channel clustering enhances weak electric field detection by neutrophils: apparent roles of skf96365-sensitive cation channels and myeloperoxidase trafficking in cellular responses. *Eur. Biophys. J.*, 35:1–26, 2005.
- [32] Proceedings of SPIE. *High-Speed fluorescence microscopy of cell signaling*, volume 5580, 2005.
- [33] A.J. Tanskanen, E.I. Tanskanen, J.L. Greenstein, and R.L. Winslow. How to formulate membrane potential in a spatially homogenous myocyte model. *eprint arXiv:q-bio/0508041*, 2005.
- [34] R.S. Eisenberg and E. Engel. The spatial variation of membrane potential near a small source of current in a spherical cell. *J. Gen. Physiol.*, 55:736–757, 1970.
- [35] D. Hellerstein. Passive membrane potentials. *Biophys. J.*, 8:358–379, 1968.
- [36] A.K. Poulsen, M.O. Petersen, and L.F. Olsen. Single cell studies and simulation of cell-cell interactions using oscillating glycolysis in yeast cells. *Biophys. Chem.*, 125:275–280, 2007.
- [37] A.T. Jackson, M.P. Timmerman, C.R. Bagshaw, and Ashley C.C. The kinetics of calcium binding to fura-2 and indo-1. *FEBS-Lett.*, 216:35–39, 1987.
- [38] Fura and indo ratiometric calcium indicators. www.probes.com.
- [39] Bernd Jähne. *Digitale Bildverarbeitung*. Springer, 2005.
- [40] E.J. Hillson and M.B. Hallett. Localised and rapid Ca^{2+} micro-events in human neutrophils: Conventional Ca^{2+} puffs and global waves without peripheral-restriction or wave cycling. *Cell Calcium*, 41:525–536, 2007.
- [41] S.S. Parikh, S.A. Litherland, M.J. Clare-Salzler, W. Li, P.A. Gulig, and F.S. Southwick. *Capg*^{-/-} mice have specific host defense defects that render them more susceptible than *capg*^{+/+} mice. *J. Infect Immun.*, 71:6582–6590, 2003.
- [42] C. Bakal, J. Aach, G. Church, and N. Perrimon. Quantitative morphological signatures define local signaling networks regulating cell morphology. *Science*, 316:1753–1756, 2007.
- [43] I. Kaganman. Training a computers eye on cell shape. In *Nat. Methods*, volume 4. 2007.

- [44] Product information. www.sigma-aldrich.com.
- [45] H. Petty. Established and emerging methods, experimental strategies, and applications in immunology. *Microsc. Res. Tech.*, 70:687–709, 2007.
- [46] O. Tour, S.R. Adams, R.A. Kerr, R.M. Meijer, T.J. Sejnowski, R.W. Tsien, and R.Y. Tsien. Calcium green flash as a genetically targeted small-molecule calcium indicator. *Nat. Chem. Biol.*, 3:423–431, 2007.
- [47] A. Doerr. Calcium imaging in a flash. In *Nat. Methods*, volume 4. 2007.

Acknowledgements

Ich möchte mich bei Prof. Jörg Langowski für die Unterstützung dieses Projekts und meine Betreuung bedanken.

Gleichermaßen danke ich Priv.-Doz. Dirk Lebiedz für Organisation dieses Projekts und meine Betreuung.

Bei Dr. Mario Mommer möchte ich mich für die nette Zusammenarbeit bedanken.

Prof. Christoph Cremer danke ich für die Bereitschaft die Zweitkorrektur der Arbeit zu übernehmen.

Außerdem danke ich Prof. Jürgen Warnatz und der *Reaflow*-Gruppe für die Bereitstellung des Arbeitsplatzes am IWR.

Bei Dr. Ulrike Engel möchte ich mich für die Einführung in die Mikroskopie mit lebenden Zellen bedanken.

Prof. Ursula Kummer danke ich für das Interesse am Projekt und der Vermittlung des Kontakts zu den Gruppen Hänsch und Olsen.

Prof. Gertrude Hänsch danke ich für die Hilfe bei der Zellpreparation.

Special thanks to Prof. Lars Olsen (University of South Denmark, Odense) for the opportunity of a very nice and interesting stay in the *Celcom* group.

Den Kollegen aus der Gruppe Langowski danke ich für den angenehmen Laboralltag.

Abschließend danke ich meiner Familie, meinen Freunden und im Besonderen Sebi für die private Unterstützung.

Ich erkläre hiermit, dass ich die vorgelegte Arbeit selbst verfasst und mich keiner anderen als der von mir ausdrücklich bezeichneten Quellen und Hilfen bedient habe.

Heidelberg, den 09. November, 2007

.....
Carina Reble

